Surface Roughness Effect on Inverse Partial Fluorescence Yield

by

Xiaopan Mao

A thesis
presented to the University of Waterloo
in fulfillment of the
thesis requirement for the degree of
Master of Science
in
Physics

Waterloo, Ontario, Canada, 2013

© Xiaopan Mao 2013

I hereby declare that I am the sole author of this thesis. This is a true copy of the thesis, including any required final revisions, as accepted by my examiners.

I understand that my thesis may be made electronically available to the public.

Abstract

X-ray absorption spectroscopy (XAS) has been benefiting many desciplines of the natural sciences. XAS is a powerful tool used to probe the electronic structure and local bonding environment of materials. Inverse partial fluorescence yield (IPFY), a new XAS technique developed in 2011, allowed greater emplyment of XAS by breaking down the limitations of existing techniques in many significant scenarios but also extended the applicability of fluorescence yield to a quantitative analysis level. [1] However, IPFY was originally developed for smooth bulk materials and the applicability of IPFY to rough surfaces or powder specimens is unknown. XAS is often performed on rough samples and there are many scenarios where bulk single crystals are not available so that the use of powder specimen is inevitable.

In this thesis, we propose a numerical model to investigate surface roughness effects on IPFY and an analytical model to account for porosity in porous specimens. To compare to this calculation, IPFY measurements on rough surface and porous $NdGaO_3$ specimens will also be presented. We found that for surface roughness size of 0.109 times the emission x-ray penetration length $1/\mu(E_f)$, the error introduced by roughness is less than 5% for any detection geometry. Our calculations also showed that the distortions of IPFY can be minimized at certain detection geometries, especially near normal incidence and emission geometry where surface roughness effects vanish. Our theoretical modeling revealed that porosity effect will only scale IPFY spectra by a constant factor so that the lineshape of IPFY is preserved.

Acknowledgements

First of all, I would like to express my gratitude to my supervisor David Hawthorn who has always been kind and supportive. The invaluable lessons he has taught me in both research and life will continue to guide me for the rest of my life. I have also benefited immensely from my fellow researchers Andrew and Chris, the appreciation towards their patience and gentle help is beyond expression. I must also acknowledge Tom, Ronny, Feizhou and many other scientists working in CLS for their advice and support. Without all those people, this work would not have been possible.

I would like to express my great appreciation to my parents for the chance they have created for me. Without their hardworking and unwavering understanding, I would never have the opportunity to experience such a wonderful foreign life. Their love is the everlasting power that drives me to chase after the life I have always been thinking of. The same appreciation expresses to my big brother Dapan, who is always ready to listen and help.

At last, I would also like to thank my friends Jiaqi, Hao, Zheng, Bingyao and Heqing for their care in my daily life and happiness they make me feel everyday.

Dedication

I dedicate this thesis to my parents Qingguo and Lifang.
Your understanding and love makes me be who I want to be.

Table of Contents

List of Tables ix

List of Figures x

List of Abbreviations xii

1 Introduction 1

1.1 X-ray absorption spectroscopy . . . 1

1.1.1 X-ray interacts with matter . . . 1

1.1.2 Fluorescence and Auger electrons . . . 2

1.1.3 X-ray absorption spectra . . . 3

1.1.4 XAS techniques . . . 6

1.1.5 Inverse partial fluorescence yield . . . 7

1.2 Overview . . . 9

2 Modeling of surface roughness effect on IPFY 11

2.1 Fluorescence yield . . . 11

2.2 Formulation of IPFY on rough surfaces . . . 13

2.3 Formulation of surface roughness effect on IPFY . . . 15

2.4 $G(z, A, x)$ dependence on IPFY . . . 15

2.5 Numerical modeling of surface roughness effect on IPFY . . . 16

2.5.1 Sine wave rough surface . . . 17
2.5.2 $G(z, A, x)$ from a sine wave rough surface . . . 19
2.5.3 Roughness size dependence of surface roughness effect on IPFY from numerical modeling . . . 22
2.5.4 Energy dependence of surface roughness effect on IPFY . . . 23
2.5.5 Geometry dependence of surface roughness effect on IPFY . . . 24

3 Experimental Demonstration of Surface Roughness Effect on IPFY 28
3.1 Details of measurement . . . 28
3.2 IPFY spectroscopy . . . 28
3.2.1 $NdGaO_3$ . . . 28
3.2.2 Penetration length of $NdGaO_3$ . . . 29
3.2.3 X-ray fluorescence and PFY . . . 30
3.2.4 IPFY spectroscopy on rough surface $NdGaO_3$ samples . . . 31

4 Granularity effect on IPFY 36
4.1 Granularity effect . . . 36
4.2 Randomly distributed rough surface . . . 37
4.3 Porosity effect . . . 37
4.4 General granularity effect . . . 39
4.5 IPFY spectroscopy on $NdGaO_3$ powder specimen . . . 40

5 Conclusions 42
5.1 Summary of results . . . 42
5.1.1 Theoretical work . . . 42
5.1.2 Experimental demonstrations . . . 44
5.1.3 Future work . . . 45

References 46

APPENDICES **50**

A Limit of numerical integration depth **51**

B Optimal sampling points **53**

C Proof of the periodicity of $G(z, A, x)$ from bulk **55**

D $NdGaO_3$ rough sample preparations and characterizations **58**

D.1 $NdGaO_3$ sample preparations 58

D.2 Characterizations of surface roughness by AFM 59

E Refinement to $S_{j,k}$ analysis of IPFY **62**

E.1 $S_{j,k}$ analysis 62

E.2 The effect of Unequal $A_{j,k}(E_i)$ on $S_{j,k}(E_i)$ analysis 63

E.2.1 The collapse of IPFY spectra 64

E.2.2 Deviation of $S_{j,k}(E_i)$ analysis under $A_j(E_i) \neq A_k(E_i)$ 65

E.2.3 Ratio of $\frac{A_j(E_i)}{A_k(E_i)}$ 66

E.2.4 Reformulism of $S_{j,k}(E_i)$ analysis in the case $\frac{A_j(E_i)}{A_k(E_i)} = M_{jk}$ 69

E.2.5 Error propagation 70

E.3 Experimental demonstration of $A_{j,k}(E_i)$ effect on $S_{j,k}(E_i)$ analysis 79

E.3.1 NdGaO3 79

E.3.2 $S_{j,k}(E_i)$ analysis of IPFY spectra 79

List of Tables

2.1 The maximum surface roughness size for different geometries from simulation. 26

3.1 Characteristic x-ray emission lines of $NdGaO_3$. 31

List of Figures

1.1 X-rays interact with matter . . . 2
1.2 Fluorescence and Auger electrons . . . 3
1.3 XAS of different elements . . . 4
1.4 XAS of Cu in different valencies . . . 4
1.5 XAS as a probe of bonding environment . . . 5
1.6 IPFY on NiO . . . 7
1.7 $\mu(E_i)$ of NiO . . . 8

2.1 Schematic of fluorescence yield. . . . 12
2.2 Schematic of x-ray interact with a smooth surface and rough surface . . . 14
2.3 Average $G(z, A, x)$ smooth and rough surfaces. . . . 16
2.4 Schematic of x-ray interacts with a sine wave rough surface . . . 17
2.5 Schematic of $G(z, A, x)$ from a sine wave surface and a smooth surface. . . . 18
2.6 $G(z, A, x)$ from a sine wave rough surface at different geometries. . . . 20
2.7 The roughness size dependence of surface roughness effect on IPFY from sine wave rough surface simulation. . . . 22
2.8 Energy dependence of surface roughness effect on IPFY based on sine wave rough surface simulation. . . . 24
2.9 Geometry dependence of surface roughness effect on IPFY from sine wave rough surface simulation. . . . 25
2.10 Contour plot of IPFY^r/IPFY^s from a sine wave rough surface as a function of $\mu(E_i)/\mu(E_f)$ and $A * \mu(E_f)$ for normal geometry and regular geometry. 27

3.1 X-ray penetration depth of $NdGaO_3$. 29
3.2 X-ray fluorescence and characteristic emission lines of $NdGaO_3$. 30
3.3 IPFY spectra of 500 grit polished $NdGaO_3$ and from calculations. 32
3.4 IPFY spectra from smooth surface, 120 grit polished $NdGaO_3$ samples at normal incidence geometriy. 34
3.5 IPFY spectra from smooth surface, 120 grit polished $NdGaO_3$ samples at regular incidence geometriy. 35

4.1 Porosity effect on randomly packed powder specimen 38
4.2 IPFY spectra of $NdGaO_3$ powder specimen. 41

B.1 Sampling points. 53

C.1 Schematic of the periodicity proof of $G(z, A, x)$ from sine wave rough surface. 55
C.2 Periodicity of $G(z, A, x)$ from bulk part. 57

D.1 Polished $NdGaO_3$ samples. 59
D.2 AFM characterizations of polished $NdGaO_3$ samples. 60
D.3 Fitting of distribution functions of polished $NdGaO_3$ rough surfaces. 61

E.1 Simulation of the $A_{j,k}(E_i)$ effect on IPFY. 67
E.2 The contour plots of $\delta S_{j,k}(E_i)/S_{j,k}(E_i)$. 72
E.3 The contour plot of $\delta\mu(E_i)/\mu(E_i)$. 74
E.4 δ_{jk} dependence of $\delta\mu(E_i)/\mu(E_i)$. 76
E.5 g_j/g_k dependence of $\delta\mu(E_i)/\mu(E_i)$. 77
E.6 $\mu(E_i)/\mu(E_f)$ dependence of $\delta\mu(E_i)/\mu(E_i)$. 78
E.7 Standard $S_{j,k}(E_i)$ analysis to obtain $\mu(E_i)$ from $NdGaO_3$ long energy range measurement. 80
E.8 Correction of $A_{j,k}(E_i)$ effect on IPFY from $NdGaO_3$ long energy range measurement. 81

List of Abbreviations

XAS	X-ray Absorption Spectroscopy
ES	Edge Steps
XANES	X-ray Absorption Near Edge Structure
EXAFS	Extended X-ray Absorption Fine Structure
XAFS	X-ray Absorption Fine Structure
EY	Electron Yield
FY	Fluorescence Yield
TEY	Total Electron Yield
TFY	Total Fluorescence Yield
IPFY	Inverse Partial Fluorescence Yield
SDD	Silicon Drift Detector
PFY	Partial Fluorescence Yield
IXL	Incident X-ray Length
EXL	Emission X-ray Length
IXD	Incident X-ray Depth
EXD	Emission X-ray Depth
RMS	Root Mean Square
CLS	Canadian Light Source
SGM	Spherical Grating Monochromator
MCP	Micro-Channel Plate
AFM	Atomic Force Spectroscopy
XRF	X-Ray Fluorescence

Chapter 1

Introduction

1.1 X-ray absorption spectroscopy

In this section, we will start with the process of x-ray absorption and how the decaying products are related to the electronic properties of materials. We will then show what consists of x-ray absorption spectra and what information can be extracted from the spectra. After that, we will talk about how **x-ray absorption spectroscopy** (XAS) is measured and the inadequacies of conventional XAS techniques. Furthermore, we will introduce the newly developed XAS technique called **inverse partial fluorescence yield** (IPFY) and how it overcomes the saturation effects other techniques have and how it is used to determine absorption coefficients. Lastly, we will discuss the problems IPFY has and how those problems motivate the investigations of surface roughness effect and porosity effect on IPFY.

1.1.1 X-ray interacts with matter

For XAS, we only concentrate in the energy range below 1 MeV. In this energy regime, excluding the transmitted x-rays, as illustrated in figure 1.1 there are three primary processes: photoelectric absorption, coherent scattering and incoherent scattering. In the process of photoelectric absorption, an incident photon is absorbed and an electron is ejected which carries the energy difference between incident photon energy and binding energy exerted by the atom to the electron. In this regime, the excitations from the left behind core-holes will decay by means of characteristic fluorescent x-rays or Auger electrons, carrying the

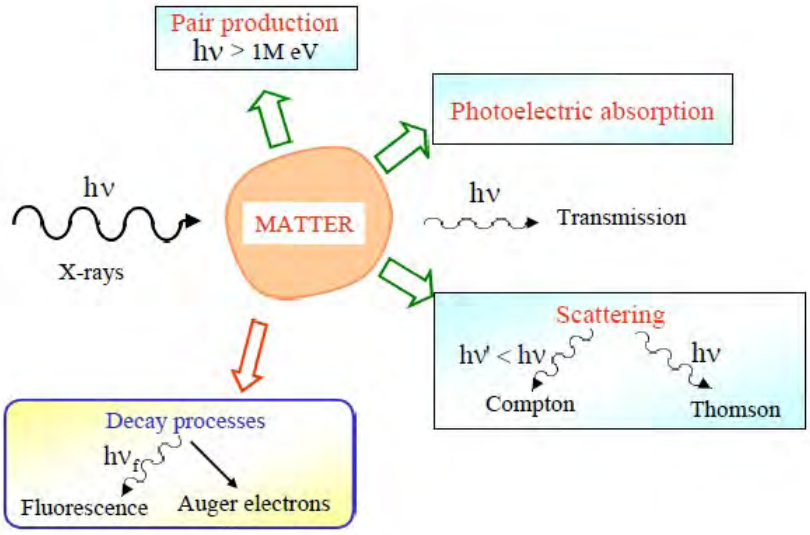


Figure 1.1: Schematic of the interaction between x-ray and matter.(Figure adapted from reference [2]).

information of the element composition and electronic structure of the material. For coherent scattering or Rayleigh scattering, the photons are scattered by bound atomic electrons with no loss of energy. For incoherent scattering or Compton scattering process, incident photons will inelastically collide with one particular kind of electron and lose its energy, the scattered x-ray wavelength is accordingly modified. [3]

1.1.2 Fluorescence and Auger electrons

When the atoms are excited by absorbing incident x-rays, the excited core-hole will eventually relax back to the ground state of the atom. As shown in figure 1.2a, in the decaying process of fluorescence regime, higher energy level core electron, for instance, level M or level L, will drop back into the core hole and emit characteristic fluorescence x-rays. The emission lines from L to K and from M to K are named as K_α and K_β emission lines, respectively. As for the Auger electron yield regime, the refillment of the core-hole will promote an Auger electron to the continuum from another core-level. Since the emission in both regimes involves in the characteristic energies of the absorbing atom, it can be used to identify the absorbing element [5, 6]. For instance, in figure 1.3, we plotted the L-edge XAS on Fe, Co, Ni, Cu in absolute cross-section scale. We can see that for same

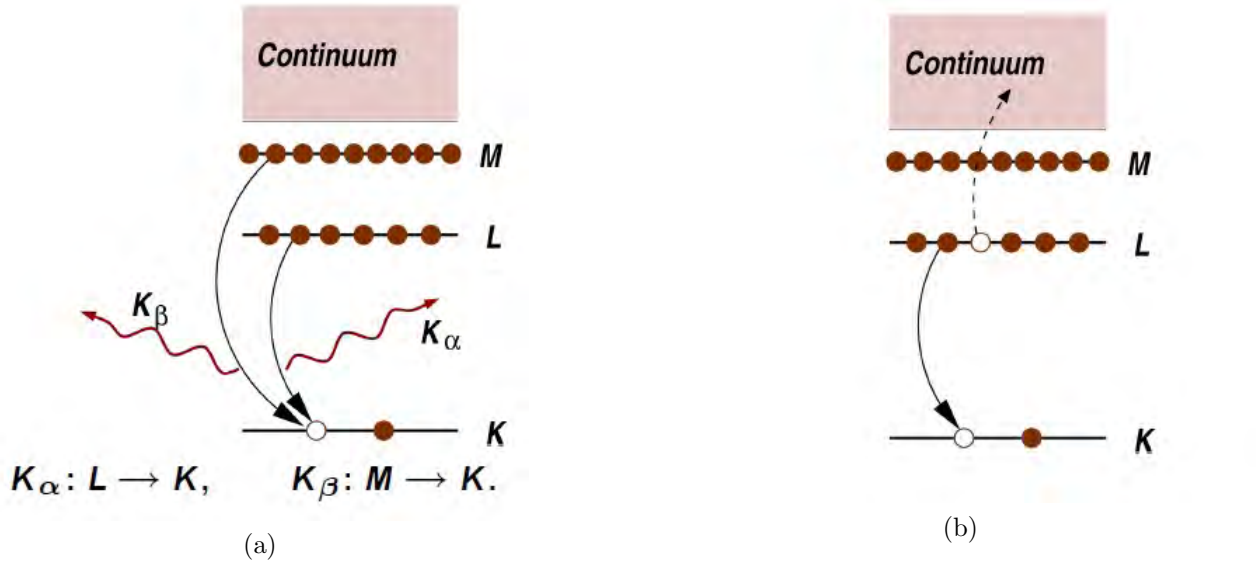


Figure 1.2: (a) X-ray Fluorescence yield process (b) Auger electron yield process.(Figure adapted from reference [4]

absorption edge, different element has different characteristic energies and this feature can be used to identify the absorbing atom.

1.1.3 X-ray absorption spectra

When x-rays interact with matter, there is a certain probability that x-rays are absorbed. Such probability is decided by the incident x-ray energy and electronic configuration of the related atoms [7–10]. In the case of free atoms model, when we increase the incident x-ray energies to be above the transition energies of inner-shell electrons, the absorption probabilities will increase largely and create sharp discontinuities often termed as **edge steps**. [8, 11, 12] In real world solids, atoms are not actually free to move but confined in lattices instead. The multi-body interactions of electrons with nearby atoms would form complicated absorption structure both near and far beyond absorption edges [10, 13]. The domination of strong scattering and local atomic resonance in the **x-ray absorption near edge structure** (XANES) provides a direct link to the oxidation state and local bonding environment of the interacted atoms. As shown in figure 1.4, the big differences in L-edge XAS of same element Cu but with different valences prove that XAS can be used to probe the oxidation state in the material.

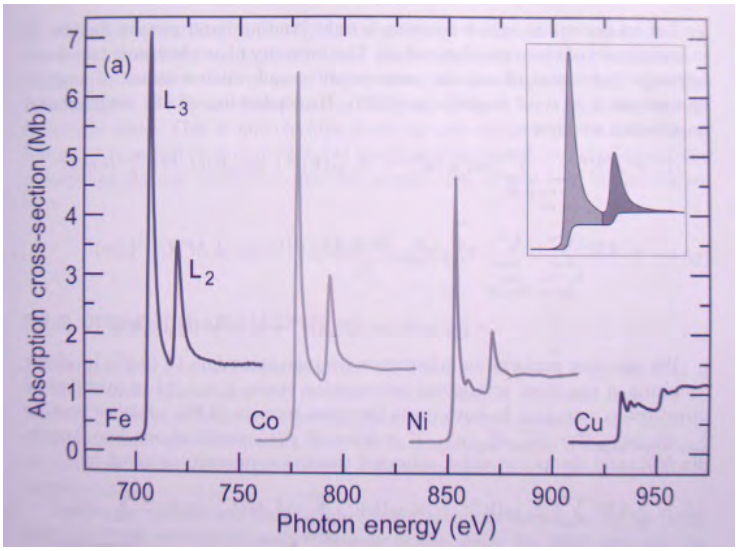


Figure 1.3: X-ray absorption spectroscopy on Fe, Co, Ni, Cu L edge in absolute cross-section scale.(Figure adapted from reference [7]).

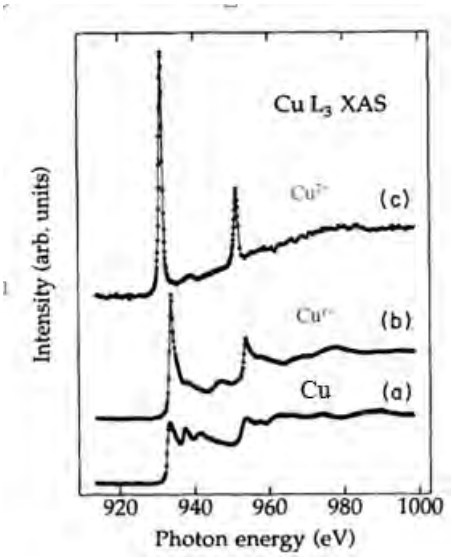


Figure 1.4: X-ray absorption spectroscopy on (a) copper metal, (b) Cu_2O, (c) CuO. (Figure adapted from reference [14]).

The polarization dependence of XAS can be used to determine the orbital information of absorbing atoms. The combination of the polarization and energy dependence makes

XAS an invaluable tool in analyzing complex systems. For example, the high temperature superconductor $YBa_2Cu_3O_{6+\delta}$ has structure as illustrated in figure 1.5a. There are three types of Cu: Cu2 (valence 2+) from CuO_2 plane is in $3d^9$ state, having a single hole in Cu $3d_{x^2-y^2}$ orbital; Cu1e (valence 1+) from CuO_2 chains is in $3d^{10}$ state with a full d shell; Cu1f (valence 2+) from CuO_2 chains is in $3d^9+3d^9\underline{L}$ state with a hole in $3d_{y^2-z^2}$ symmetry. Those three types of Cu atoms within the same system can be identified by XAS based on their preferred polarization, valences and their characteristic energies of the corresponding states as shown in figure 1.5b.

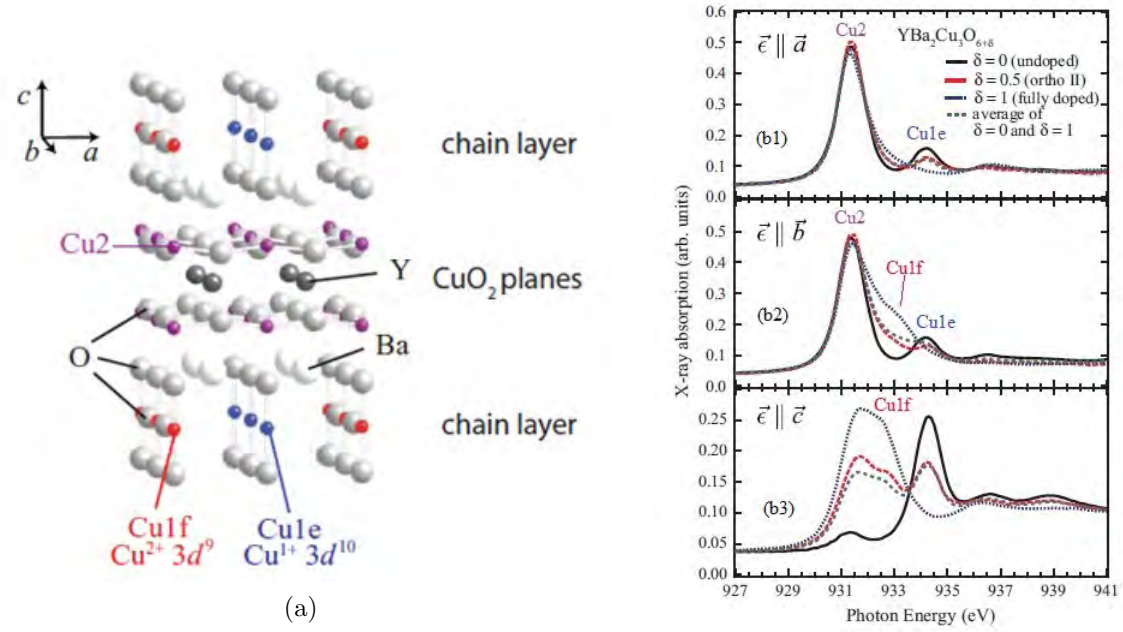


Figure 1.5: (a) The structure of high temperature superconductor $YBa_2Cu_3O_{6+\delta}$. δ refers to doping and has value from 0 to 1. (b1) Cu L-edge XAS of $YBa_2Cu_3O_{6+\delta}$ with polarization parallel to a axis. (b2) Cu L-edge XAS of $YBa_2Cu_3O_{6+\delta}$ with polarization parallel to b axis. (b3) Cu L-edge XAS of $YBa_2Cu_3O_{6+\delta}$ with polarization parallel to c axis. Figures are adapted from reference [15].

Beyond the absorption edge, the quantum interference results from emitted photoelectrons created oscillations in XAS spectra which give information on the number and chemical indentities of near neighbours and the average interatomic distances [16–18]. This spectral region is named as **extended x-ray absorption fine structure** (EXAFS). Combining spectral regions of XANES and EXAFS, we obtain the region called **x-ray absorption**

fine structure (XAFS).

XAS measurements are performed at synchrotron beamlines which provides us with much more photon flux and higher data collection efficiency than old x-ray tube based XAS measurements [19]. In XAS measurements, we can tune photon energies to correspond to transition energy between an particular inner-shell energy level and an unoccupied state, such element specific targeting measurements make XAS a powerful tool in the study of structural and electronic properties of matter in wide scenarios across all natural sciences.

1.1.4 XAS techniques

There are three common XAS techniques: transmission, **electron yield** (EY) and **fluorescence yield** (FY) [7,10,20,21]. Transmission measurement is operated by transmitting very strong x-ray flux through a thin sample and the transmitted x-ray is detected right behind the sample. The theory behind transmission mode is Beer-Lambert law which is a direct measurement of x-ray attenuation coefficient. However, the requirement of ultra-thin sample for this technique makes it very restrictive. As to EY and FY, those two are the decaying product of x-ray interactions with matter. When x-rays are interacting with a sample, the absorbing atom is excited to an upper unoccupied state and leaves behind a core hole [10]. The main channels for the excited atom to decay is either to emit a characteristic fluorescence photon or eject one or more kinetic Auger electrons. For low-energy excitation, Auger emission will dominate the relaxation process while fluorescence is the primary relaxation process for higher-energy excitation, e.g., atomic numbers greater than 40. The probability of either case depends on atomic shell and atomic number Z of the atom. [22–24] For the collection of EY, it is usually completed by measuring the drain current that created by the refillment of the vacancies left behind by the escaped electrons. This drain current is the measure of what we termed as **total electron yield** (TEY). Alternatively, if the escaping electrons carried sufficient kinetic energies, a channelplate or channeltron detector can be used to detect them. As to the detection of FY, photodiode, channelplate or channeltron detectors are the main tools to collect the **total fluorescence yield** (TFY).

TEY is a surface sensitive technique. It is very sensitive to surface contamination or surface charging in insulators. Conversely, TFY is a bulk sensitive technique [7]. However, it failed to produce reliable XAS spectra in the case of concentrated samples due to saturation effects. Futhermore, neither TEY nor TFY is directly proportional to x-ray absorption cross-section since they are not directly related to absorption process. Even though a lot of

effort has been spent to correct the XAS spectra due to discrepancies from the techniques themselves, full eliminations of the erroneous spectra from those two techniques cannot be achieved [25, 26].

1.1.5 Inverse partial fluorescence yield

In 2011, a new XAS technique called **inverse partial fluorescence yield** (IPFY) is developed and the detection of the IPFY makes use of a energy dispersive photon detector, such as **silicon drift detector** (SDD) to collect the **partial fluorescence yield** (PFY) from non-resonant atom or core state [1, 27]. For instance, in figure 1.6, PFY spectra from

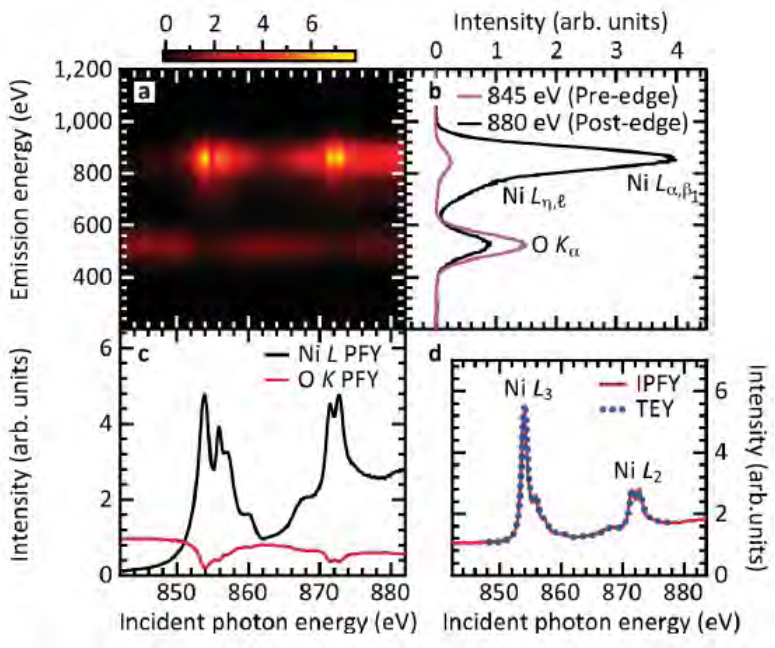


Figure 1.6: (a) X-ray fluorescence of NiO across Nd L_3 and L_2 edges. (b) Emission spectra of resonant Ni L edges and non-resonant O K edges at energy 845 eV and 880 eV, respectively. (c) PFY of Ni L edge and O K edge (d) IPFY is the inversion of O K PFY and show good agreement with TEY data. (Figure adapted from reference [1]).

resonant Nickel L edge and non-resonant Oxygen K edge are measured, and the resonant PFY from Nickel L edge is largely distorted and cannot be used to determine absorption coefficient. IPFY in this case is simply the inversion of the PFY from non-resonant Oxygen K emission, for example, IPFY=$1/\text{PFY}_{OK}$. As argued by Achkar in reference [1], IPFY

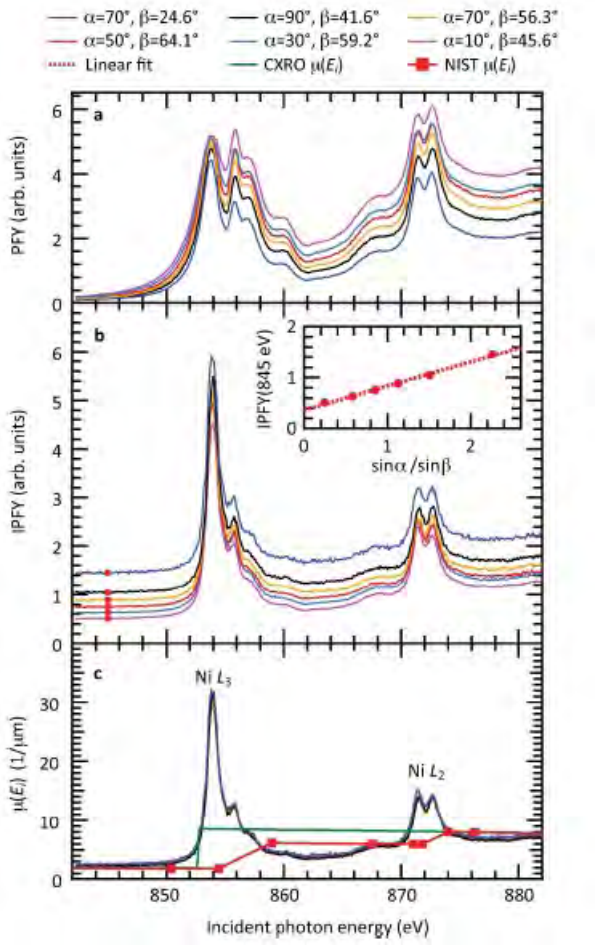


Figure 1.7: (a) PFY of NiO across Nd L_3 and L_2 edges. (b) IPFY from O K edge at different geometries. (c) By using fitting parameters from geometry, the resulted spectra showed excellent agreement with literature. 1(Figure adapted from reference [1]).

turns out to be proportional to the absorption coefficient and such result can be seen by the good agreement of IPFY with TEY in figure 1.6 part (d). For detection geometry denoted as j, IPFY can be written as:

$$\text{IPFY}_j \quad = \quad A\left(\mu\left(E_i\right)+\mu\left(E_f\right)\frac{\sin\alpha_j}{\sin\beta_j}\right) \tag{1.1}$$

where A depends weakly on energy over XANES region and can be approximately treated as a constant. Such constant can be obtained by fitting IPFY from different geometries.

As shown in figure 1.7, IPFY on NiO taken at same energy 845 eV but different geometries varies linearly with $\sin\alpha/\sin\beta$ as predicted in formula (1.1). The good agreement of absorption coefficient obtained from IPFY with literature verified the proportionality of IPFY with linear absorption coefficients.

The newly developed XAS technique IPFY is both bulk sensitive and free of saturation effects and charging effect, and most importantly, it is also a direct accurate measure of total x-ray absorption coefficient [1, 27]. Based on that, IPFY is even able to do compositional analysis of materials [28]. Those prominent features of IPFY make it a very powerful tool in rich avenues in XAS.

IPFY is originally developed for smooth single crystals, however, XAS is often performed on rough or powder samples. We want to know which features of IPFY are robust when IPFY is performed on rough surfaces or porous samples. Also, we want to know under what roughness sizes, geometries and other conditions, IPFY can be still applied to rough surfaces or porous samples. When dated back to existing treatments of surface roughness effect and porosity effect on general x-ray fluorescence yield measurement, the efforts so far to my knowledge only worked out for very limited parameter space and specific scenarios, which cannot meet the purpose of our subject [29–34]. The investigations over surface roughness effect and porosity effect on IPFY are important and demanding.

1.2 Overview

Chapter 2 will start with the formulation of IPFY on rough surface, and followed from the formulation is the discussion of the newly introduced parameter due to surface roughness. In modeling surface roughness effect, we proposed an artificial sine wave rough surface to numerically model the dependence of surface roughness on roughness size, geometry and incident photon energy. All the details in our calculations, such as critical number of sampling points, critical depth can be found in our Appendix A, B, C. In Appendix E, we also discussed about the refinement to IPFY spectroscopy when experimental conditions are not stable. That section is for the purpose of understanding the discrepancy in our quantitative analysis of absorption coefficients on smooth surfaces and the corresponding correction to it.

In chapter 3, we will further verify our numerical modeling with experimental demonstrations on rough $NdGaO_3$ samples. We will show IPFY spectra measured on smooth

surfaces, 500 grit polished sample and 120 grit polished sample in two different geometries. By inserting the real surface roughness sizes from atomic force spectroscopy (AFM) characterizations into our numerical calculations, we found that sine wave model can well capture the degrees of distortion on rough surface IPFY. However, this sine wave model cannot fully capture the trend of the change in IPFY intensity, which may due to the fact that our single roughness size parametrization is not sufficient to resolve all the features contained in a real rough surface.

In addition to our main topic, we discussed qualitatively about granularity effect from porous samples in chapter 4. In a special case where we have smoothly polished powder specimen, a theoretical model is proposed to treat porosity effect in IPFY and the results from this model will be shortly discussed. Later, we illustrated IPFY measurement performed on porous $NdGaO_3$ samples and those results will only be qualitatively commented.

Chapter 2

Modeling of surface roughness effect on IPFY

In this chapter, we will first formulate IPFY expression for rough surfaces based on the IPFY expression from smooth surfaces. To quantify the effect of surface roughness, a sine wave rough surface profile was proposed and the change in IPFY intensity from a rough surface with respect to a smooth surface is calculated in all interested physical ranges. The surface roughness size dependence, energy dependence and geometry dependence of the effect will be discussed respectively.

2.1 Fluorescence yield

To understand our later formulation of surface roughness effect on IPFY, we have to first understand a few terminologies involved in the former formulation of fluorescence yield for smooth surfaces [27]. Consider the detection of fluorescence yield with geometry as illustrated in figure 2.1, where the incident beam with energy E_i makes an angle α with the surface and the emission beam with energy E_f makes an angle β with the surface. Therefore the normalized differential intensity contribution from element X over a thin layer with thickness dz at depth z is:

$$\frac{dI_X\left(E_i,E_f\right)}{I_0\left(E_i\right)} = \eta\left(E_f\right)\frac{\Omega}{4\pi}\omega_X\left(E_i,E_f\right)\frac{\mu_X\left(E_i\right)}{\sin\alpha}e^{-\left(\frac{\mu\left(E_i\right)}{\sin\alpha}+\frac{\mu\left(E_f\right)}{\sin\beta}\right)z}dz \tag{2.1}$$

where $\eta\left(E_f\right)$ is the detector efficiency, Ω is the solid angle made by the detector, $\omega_X\left(E_i,E_f\right)$

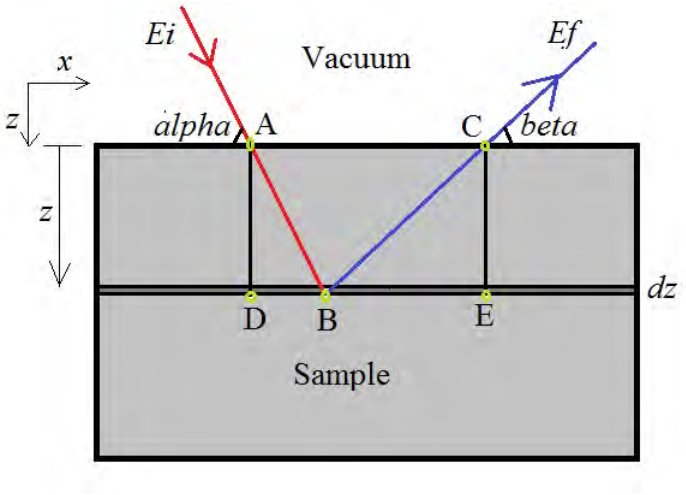


Figure 2.1: Schematic of fluorescent x-ray attenuation.

is the probability that an incident photon of energy E_i will lead to a fluorescence photon of energy E_f, rather than emission of one or more Auger electrons, with index X as atoms/core states specific. $\mu(E_i)$ and $\mu(E_f)$ are the total absorption coefficients of the material at energy E_i and E_f, respectively.

For clarity, we will introduce some important terminologies. As depicted in figure 2.1, our **incident x-ray length** (IXL) at depth z is defined to be the length incident x-ray travelled inside the sample, in this case, L_{AB}, which is related to depth z as $z/\sin\alpha$. Similarly, the **emission x-ray length** (EXL) at depth z is $L_{BC} = z/\sin\beta$. If we only consider the length x-ray travelled along the depth direction z, it is termed as **incident x-ray depth** (IXD), which is L_{AD} and it is the same as depth z. In the same way, the **emission x-ray depth** (EXD) L_{CE} is defined to be the length emission x-ray travelled along z direction and it also has same length as depth z. In this sense, the difference between IXD and EXD for a smooth surface is zero. Later on we will see in a rough surface, IXD is no longer the same as EXD.

Followed from equation (2.1), the integrated partial fluorescence yield from element X can be expressed as:

$$\mathrm{PFY}_X = \frac{I_X(E_i, E_f)}{I_0(E_i)} = \frac{\Omega}{4\pi}\eta(E_f)\,\omega_X(E_i, E_f)\int_0^\infty \frac{\mu_X(E_i)}{\sin\alpha} e^{-\left(\frac{\mu(E_i)}{\sin\alpha}+\frac{\mu(E_f)}{\sin\beta}\right)z} dz \tag{2.2}$$

Experimentally, $I_0(E_i)$ is measured from a metal grid, so the true incident photon intensity[1] is $I_{Grid}(E_i) = I_0(E_i)\,\nu_{Grid}(E_i)$ where $\nu_{Grid}(E_i)$ is grid quantum efficiency; therefore,

[1] Photons that are directly received by samples.

the experimental partial fluorescence yield is modified by replacing I_0 with I_{Grid}:

$$\mathrm{PFY}_X = \frac{I_X\left(E_i, E_f\right)}{I_{Grid}\left(E_i\right)} = \frac{I_X\left(E_i, E_f\right)}{I_0\left(E_i\right)\nu_{Grid}\left(E_i\right)} \tag{2.3}$$

Combine equation (2.2) and (2.3), we obtain that:

$$\mathrm{PFY}_X = \frac{\Omega}{4\pi}\frac{\eta\left(E_f\right)\omega_X\left(E_i, E_f\right)}{\nu_{Grid}\left(E_i\right)}\int_0^\infty \frac{\mu_X\left(E_i\right)}{\sin\alpha} e^{-\left(\frac{\mu\left(E_i\right)}{\sin\alpha}+\frac{\mu\left(E_f\right)}{\sin\beta}\right)z} dz \tag{2.4}$$

2.2 Formulation of IPFY on rough surfaces

Experimentally, IPFY expression for a smooth homogeneous material with geometry depicted in figure 2.2a is simply a inversion of its correponding PFY, where PFY is from non-resonant element or core state X [27]. Followed from equation (2.4), smooth surface IPFY can be expressed as:

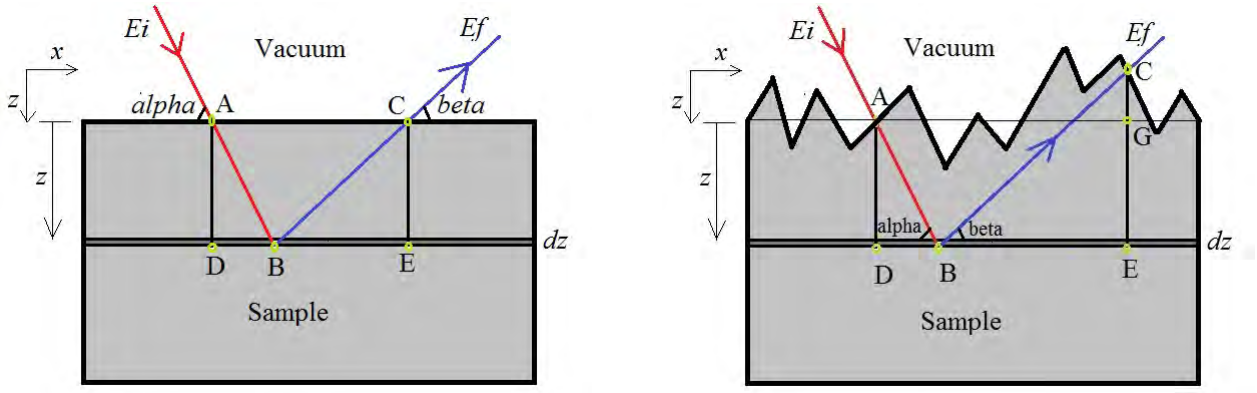
$$\mathrm{IPFY}_s = \frac{1}{\frac{\Omega}{4\pi}\frac{\eta\left(E_f\right)\omega_X\left(E_i,E_f\right)}{\nu_{Grid}\left(E_i\right)}\int_0^\infty \frac{\mu_X\left(E_i\right)}{\sin\alpha} e^{-\left(\frac{\mu\left(E_i\right)}{\sin\alpha}+\frac{\mu\left(E_f\right)}{\sin\beta}\right)z} dz} \tag{2.5}$$

In figure 2.2a, as argued before, for a smooth surface we can see the incident x-ray depth (IXD) ${L^s}_{AD}$ is always the same as the emission x-ray depth (EXD) ${L^s}_{CE}$ at any depth z. Whereas in rough surface in figure 2.2b, the EXD ${L^r}_{CE}$ is no longer the same as IXD ${L^r}_{AD}$. Clearly, the difference in IXD and EXD L_{CG} in a one dimensional rough surface as depicted, is related to depth z, lateral position x and **root mean square** (RMS) A of this rough surface profile. If we define the difference between effective IXD and EXD at depth z and lateral position x as following:

$$G\left(z, A, x\right) \quad = \quad \mathrm{EXD}\left(z, A, x\right) - \mathrm{IXD}\left(z, A, x\right) \tag{2.6}$$

Instead of using depth z for EXD in formula (2.5), we have to use $z + G\left(z, A, x\right)$ for rough surface case. In addition, the integration has to integrate over the lateral direction due the x dependence of $G\left(z, A, x\right)$. [30] Therefore, by incorporating equation (2.6) into equation (2.5), we can write our IPFY expression for rough surfaces as following:

$$\mathrm{IPFY}_r = \frac{1}{\frac{\Omega}{4\pi}\frac{\eta(E_f)\omega_X(E_i,E_f)}{\nu_{Grid}(E_i)}\int_{x1}^{x2}\int_0^\infty \frac{\mu_X(E_i)}{\sin\alpha} e^{-\left(\frac{\mu\left(E_i\right)}{\sin\alpha}z+\frac{\mu\left(E_f\right)}{\sin\beta}(G(z,A,x)+z)\right)} dzdx} \tag{2.7}$$



(a) (b)

Figure 2.2: (a) A smooth bulk material with incident x-ray making an angle α and emission x-ray making an angle β to the surface. The IXD $L^s{}_{AD}$ is equal to EXD $L^s{}_{CE}$ as defined as z. (b) X-ray interacts with a rough surface bulk sample. The incident angle α and emission angle β are defined with respect to smooth surface plane. The IXD $L^r{}_{AD}$ is different from EXD $L^r{}_{CE}$ in rough surface and our $G(z, A, x)$ is $L^r{}_{CG}$ in this depiction.

To simplify equation (2.7), we will define quantity $A(E_i)$ to be:

$$A(E_i) = \frac{\nu_{Grid}(E_i)}{\frac{\Omega}{4\pi}\eta(E_f)\,\omega_X(E_i, E_f)\,\mu_X(E_i)} \tag{2.8}$$

Hence, rough surface IPFY expression can be reduced into:

$$\text{IPFY}_r = \frac{A(E_i)}{\int_{x1}^{x2}\int_0^{\infty}\frac{1}{\sin\alpha}e^{-\left(\frac{\mu(E_i)}{\sin\alpha}z+\frac{\mu(E_f)}{\sin\beta}(G(z,A,x)+z)\right)}dzdx} \tag{2.9}$$

Similarly, we can rewrite IPFY formula (2.5) for smooth surface as:

$$\text{IPFY}_s = \frac{A(E_i)}{\int_0^{\infty}\frac{1}{\sin\alpha}e^{-\left(\frac{\mu(E_i)}{\sin\alpha}+\frac{\mu(E_f)}{\sin\beta}\right)z}dz} \tag{2.10}$$

2.3 Formulation of surface roughness effect on IPFY

The simpliest way to see how much effect surface roughness would cause on IPFY is to divide IPFY from a smooth surface by IPFY from a rough surface with same experimental conditions[1] [29]. Combine equation (2.9) and equation (2.10), the ratio $\mathrm{IPFY}_r/\mathrm{IPFY}_s$ is:

$$\frac{\mathrm{IPFY}_r}{\mathrm{IPFY}_s} = \frac{A_r\left(E_i\right)}{A_s\left(E_i\right)} \frac{\int_0^\infty e^{-\left(\frac{\mu\left(E_i\right)}{\sin\alpha}+\frac{\mu\left(E_f\right)}{\sin\beta}\right)z} dz}{\int_{x1}^{x2}\int_0^\infty e^{-\left(\frac{\mu\left(E_i\right)}{\sin\alpha}z+\frac{\mu\left(E_f\right)}{\sin\beta}\left(G(z,A,x)+z\right)\right)} dzdx} \tag{2.11}$$

where the subcript indices r and s which represent *rough* and *smooth* and $A\left(E_i\right)$ represents the experimental conditions in measurement.
In our IPFY measurements, most often the experimental conditions are very stable, therefore the fluctuations in $A\left(E_i\right)$ are negligible, equation (2.11) can be further reduced as:

$$\frac{\mathrm{IPFY}_r}{\mathrm{IPFY}_s} = \frac{\int_0^\infty e^{-\left(\frac{\mu\left(E_i\right)}{\sin\alpha}+\frac{\mu\left(E_f\right)}{\sin\beta}\right)z} dz}{\int_{x1}^{x2}\int_0^\infty e^{-\left(\frac{\mu\left(E_i\right)}{\sin\alpha}z+\frac{\mu\left(E_f\right)}{\sin\beta}\left(G(z,A,x)+z\right)\right)} dzdx} \tag{2.12}$$

However, in some rare cases, the fluctuations in $A\left(E_i\right)$ are noticable and can affect our analysis of IPFY spectra. In our later experimental demonstration on $NdGaO_3$ for rough surfaces, we will see such effect. Besides, if such instable conditions happened in two separate IPFY measurement on smooth surfaces, the absorption coefficients we obtained regularly would be quite different from literature, however such discrepancy can be corrected properly as shown in appendix E.

2.4 $G\left(z, A, x\right)$ dependence on IPFY

From our formulation of IPFY for rough surfaces, we found $G\left(z, A, x\right)$ essentially decides how the IPFY intensity will change with respect to smooth surfaces. For a real rough surface, $G\left(z, A, x\right)$ is very position dependent and the sign of average $G\left(z, A, x\right)$ can be

[1] Same experimental conditions mean in these two IPFY measurements for smooth surface and rough surface, all variables inside of $A\left(E_i\right)$ and geometries should be consistent. However, this is not always the case as would be discussed in Appendices.

positive or negative which relies on the actual structure of rough surface and detection geometry. Here we just want to briefly discuss about the possibilies that the IPFY spectra would evolve for rough surfaces at different cases of $G(z, A, x)$. As illustrated in figure 2.3, in the case of smooth surfaces, the average $G(z, A, x)$ denoted as G_{avg} is 0, the IPFY intensity would stay the same. In the case shown in (b), where the G_{avg} is less than 0, which means emitted x-rays are attenuated less than they should be, so the collected PFY intensity would be bigger than expected, therefore IPFY intensity would drop accordingly. In the case shown in (c), where we have positive average G_{avg}, similarly, the IPFY intensity from rough surfaces would be bigger than smooth surfaces.

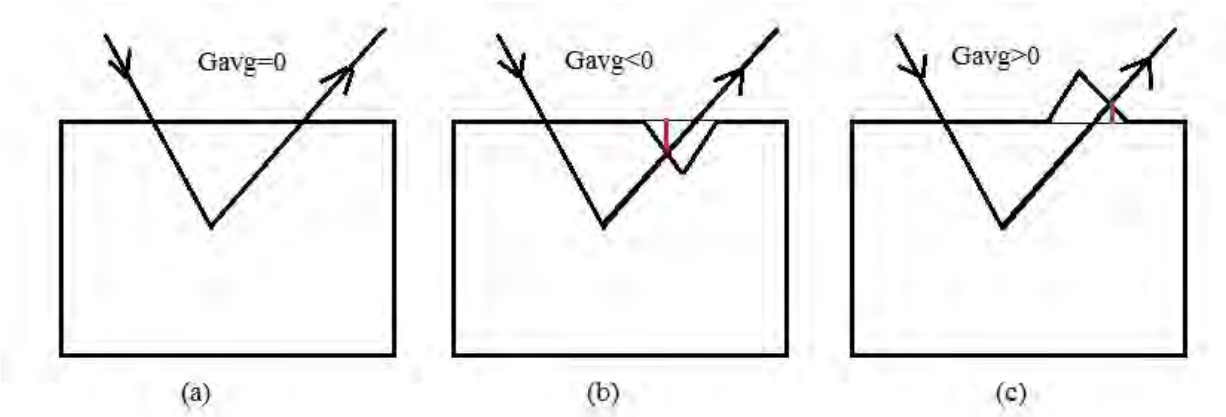


Figure 2.3: (a) Smooth surface with average $G(z, A, x)$ to be 0. (b) Rough surface with average $G(z, A, x)$ to be less than 0. (c) Rough surface with average $G(z, A, x)$ to be bigger than 0.

2.5 Numerical modeling of surface roughness effect on IPFY

In this section, we will first verify $G(z, A, x)$ calculated from a sine wave rough surface by its actual detection schematic, and then follow the expression we developed for surface roughness effect to numerically calculate the roughness size, energy and geometry dependence of the effect based on a sine wave rough surface. Those are the main results of my numerical modeling.

2.5.1 Sine wave rough surface

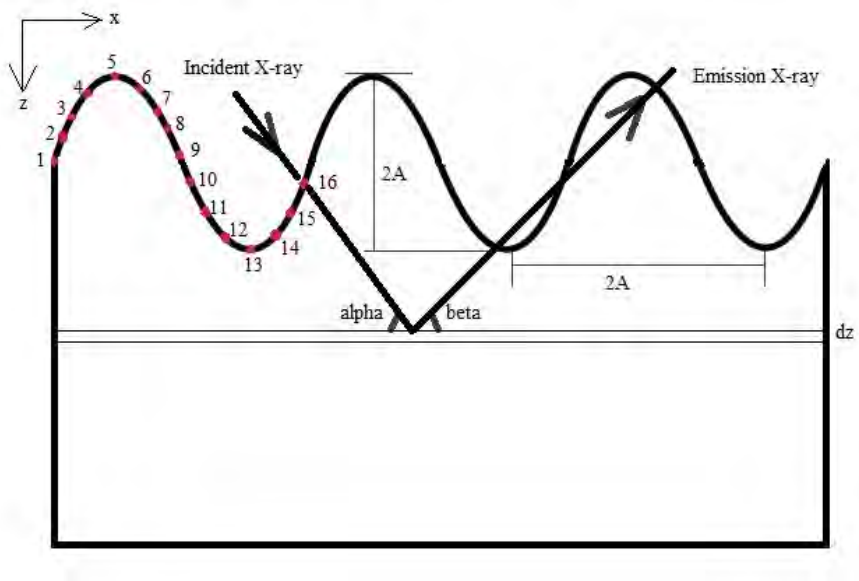


Figure 2.4: Schematic of x-rays interact with a sine wave rough surface which has peak to peak amplitude $2A$ and period $2A$. 16 sampling points over a cycle $2A$ along lateral direction x are displayed.

In figure 2.3, we build up a sine wave rough surface with peak to peak amplitude $2A$ and period $2A$, the length l and thickness d of the sample is far bigger than roughness scale A. Since sine wave rough surface is a periodic structure, the effective lateral integration range is just one cycle $2A$. As to choose the integration depth into the sample and number of sampling points over one cycle, we have to consider both computation time and sensible physical limits in order to achieve reasonable accuracy. Eventually, in our numerical calculations, we neglected the contribution that is less than 0.1% of the normalized differential intensity and this gives us the limit of number of integration steps. In terms of determination of the number of sampling points, we calculated the convergence of IPFY in high physical limits for sampling points up to 128. We found that with sampling points to be 64, we are able to reduce the percentage error in IPFY to be less than 0.1% in our interested physical ranges. All the verifications of the limits in our calculations can be found in the Appendix A, B.

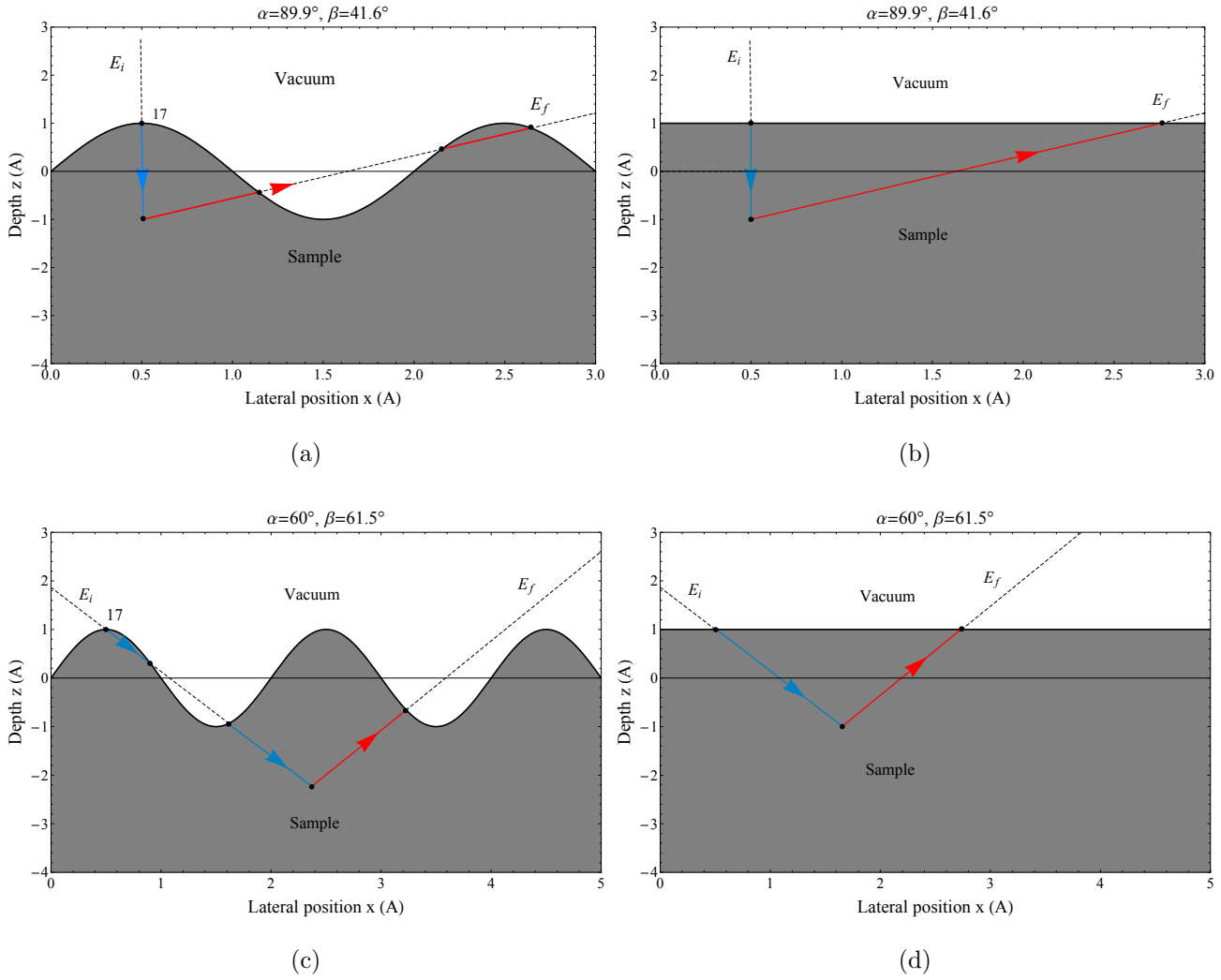


Figure 2.5: (a) Schematic of x-ray traversed at effective depth $2A$ on a sine wave rough surface at normal incidence geometry, where solid blue curve is effective incident x-ray length and solid red curve is effective emission x-ray length. (b) Schematic of x-ray traversed at effective depth $2A$ on a smooth surface at normal incidence geometry. (c) Schematic of x-ray traversed at effective depth $2A$ on a sine wave rough surface at regular incidence geometry. (d) Schematic of x-ray traversed at effective depth $2A$ on a smooth surface at regular incidence geometry.

2.5.2 $G(z, A, x)$ from a sine wave rough surface

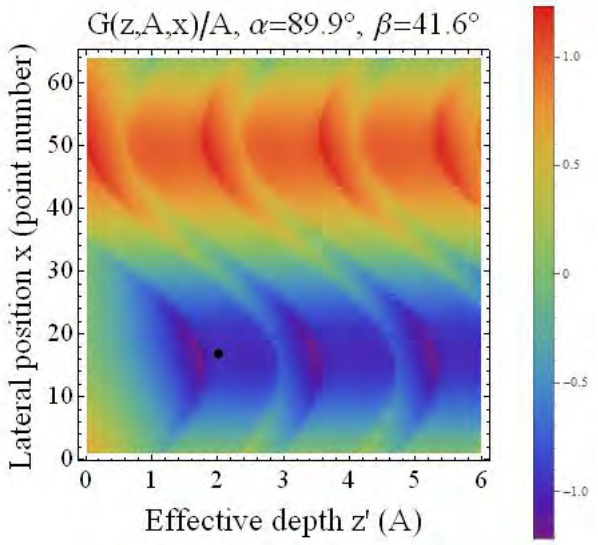
To understand our later calculations for $G(z, A, x)$, the explanation of the calculation process is necessary. In figure 2.5, we illustrated how x-ray traverse differently in a sine wave rough surface and a smooth surface at effective depth $2A$ for two selected geometries at sampling point 17 (crest).[1] The selected geometries correspond to two experimental detection geometries in IPFY measurements. For normal incidence geometry, effective emission x-ray length (solid red curve) in rough surface is shorter than in smooth surface, which therefore gives us negative $G(z, A, x)$. In regular incidence geometry[2], depth z is no longer the same as effective incident x-ray depth as part of the length along incident x-ray direction is in the vacuum. In order to calculate $G(z, A, x)$ at effective depth $2A$, we have to go deeper into the sample than smooth surface case as shown in 2.5c, and the sign of $G(z, A, x)$ turned out to be negative.

In figure 2.5, we illustrated how we obtain $G(z, A, x)$ for one specific integration step sampled from point 17. To calculate IPFY, we have to calculate $G(z, A, x)$ for all 64 sampling points at desired depth. In figure 2.6a and 2.6c, we showed the density plot of calculated $G(z, A, x)$ for all 64 sampling points up to effective depth $6A$ for the detection geometries illustrated in figure 2.5. The two black dots in figure 2.6a and 2.6c correspond to the schematic drawing in figure 2.5, and the signs of the corresponding $G(z, A, x)$ are consistent with our prediction.

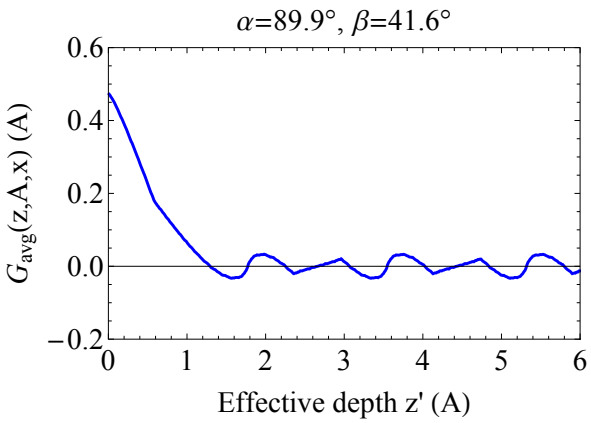
In normal incidence geometry, for the rough layer part($z' < 2A$) in 2.6a, $G(z, A, x)$ is quite different at different sampling point. We can see that $G(z, A, x)$ from this part is a complicated outcome of the rough surface and it cannot reveal much information about the rough surface profile. From equation (2.9), we can see the intensity of IPFY is in a exponential relationship with $G(z, A, x)$. Therefore, in our integration for IPFY, the dominant contribution is from the rough layer part. We will term $G(z, A, x)$ from rough layer part as type I $G(z, A, x)$, and type I $G(z, A, x)$ mainly decides the distortions in IPFY. When we probe further into the bulk part of the sample, $G(z, A, x)$ starts to form periodic pattern and such periodic structure is proved to be the same for all sampling points at same geometry in Appendix C. For periodic $G(z, A, x)$ from bulk part, those periodic patterns are transformations of the corresponding sine wave rough surface profile which reflect the genuine properties of our rough surface. Therefore, an analytical treatment for surface roughness effect is possible if we only have this type of $G(z, A, x)$. Since the average $G(z, A, x)$ from this periodic pattern is zero, IPFY contribution from this part will not distort IPFY. We will term $G(z, A, x)$ from the bulk part as type II $G(z, A, x)$.

[1] Depth z is the geometrical depth from its incident point where effective depth is the depth that x-ray has traversed inside the sample.

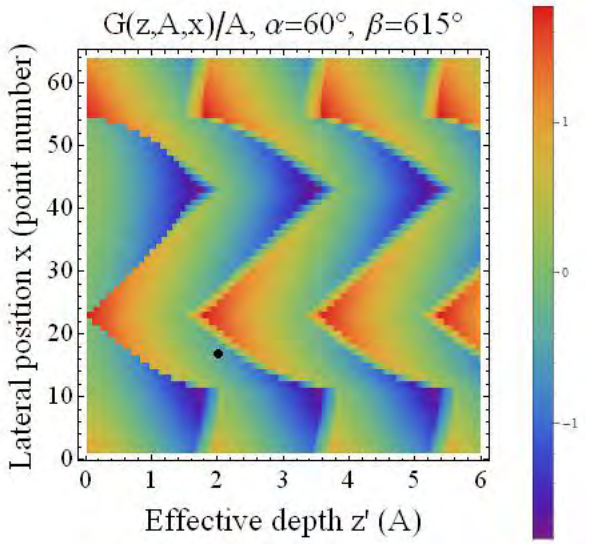
[2] The regular incidence geometry is $\alpha = 60\,^\circ$ and $\beta = 61.5\,^\circ$.



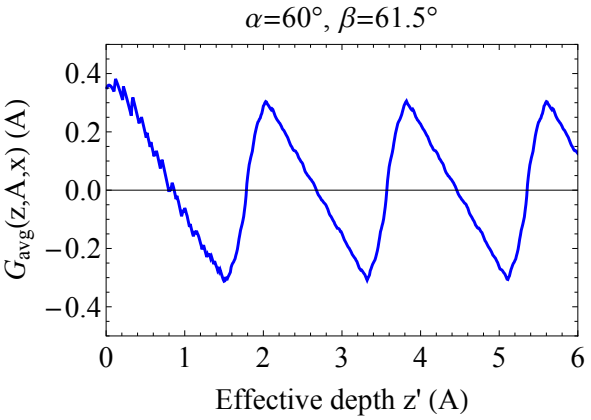
(a)



(b)



(c)



(d)

Figure 2.6: (a) Density plot of $G(z, A, x)/A$ with α, β to be 89.9° and 41.6°, respectively. (b) Average of $G(z, A, x)/A$ over lateral direction with geometry same as (a).(c) Density plot of $G(z, A, x)/A$ with $\alpha = 60°$ and $\beta = 61.5°$. (b) Average of $G(z, A, x)/A$ over lateral direction with geometry same as (c). The lateral position is in unit of the sampling number along the surface and effective depth is in unit of A.

From 2.6b, we can see the overall sign for rough layer part $G(z, A, x)$ in normal incidence geometry is positive and it indicates the increase in IPFY intensity with respect to smooth surface.
For regular incidence geometry, similar to normal incidence, $G(z, A, x)$ from rough layer is distinct at each x position but periodic in bulk part. The overall $G(z, A, x)$ is positive at depth less than $1A$ but negative at layer between $1A$ to $2A$, this will result in a competition between the positive $G(z, A, x)$ and negative $G(z, A, x)$ contributions in IPFY calculations. In this case, IPFY intensity from this geometry may be either bigger or smaller than the smooth surface.
Our following sections will use the calculated $G(z, A, x)$ values from those two geometries to calculate the effect on surface roughness effect on roughness size, geometry and energy. The prediction of the change in IPFY intensity based on the average $G(z, A, x)$ for those two geometries will be tested.

2.5.3 Roughness size dependence of surface roughness effect on IPFY from numerical modeling

The physical parameters involved in IPFY spectroscopy are incident photon energy energy E_i, emission energy E_f, alternatively, incident attenuation coefficient $\mu(E_i)$, emission attenuation coefficient $\mu(E_f)$, and geometry angle α, β. For the study of surface roughness effect on IPFY, another parameter surface roughness A will be introduced into former parameter space. In our simulations, we will convert our $\mu(E_i)$ and A into unit of $\mu(E_f)$ and $1/\mu(E_f)$, respectively, since $\mu(E_f)$ is a fixed quantity for a given sample. Such dimensionless conversion is not subject to any specific materials and the conclusions drawn can be general.

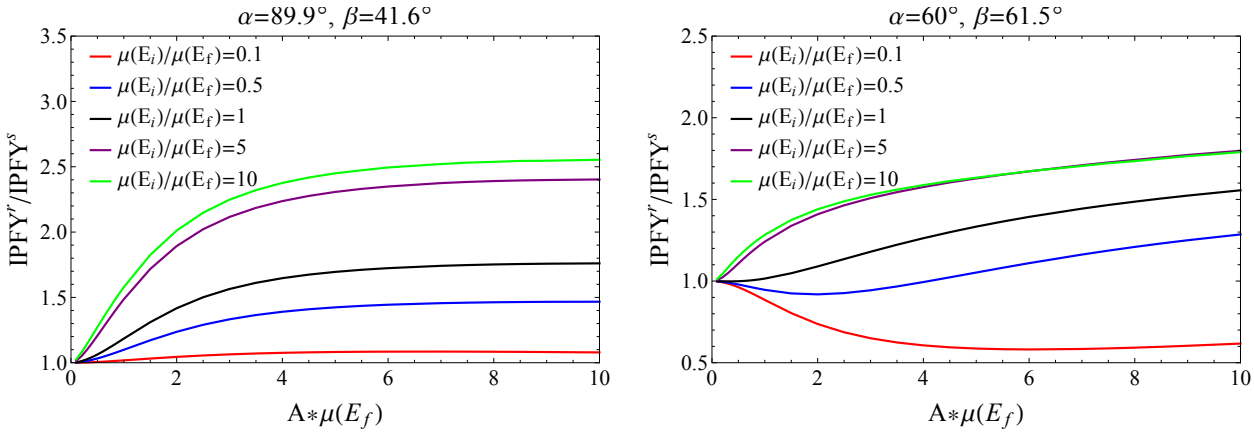


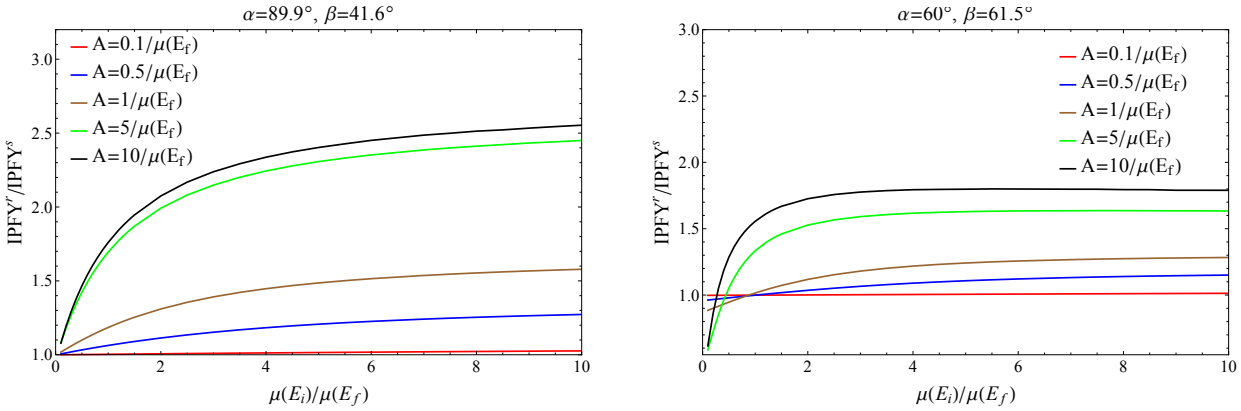
Figure 2.7: (a) The roughness size dependence of sine wave surface roughness effect on IPFY at $\mu(E_i)$ as $0.1\mu(E_f)$, $0.5\mu(E_f)$, $1\mu(E_f)$, $5\mu(E_f)$, $10/\mu(E_f)$ with geometry α, β to be $89.9\,^\circ$ and $41.6\,^\circ$, respectively. (b) The roughness size dependence of sine wave surface roughness effect on IPFY at $\mu(E_i)$ as $0.1\mu(E_f)$, $0.5\mu(E_f)$, $1\mu(E_f)$, $5\mu(E_f)$, $10\mu(E_f)$ with geometry α, β to be $60\,^\circ$ and $61.5\,^\circ$, respectively.

Typically, for XAS in soft x-ray region, $\mu(E_i)$ is in the range of $0.1\mu(E_f)$ to $10\mu(E_f)$. $\mu(E_i)$ from pre-edge and post-edge region is usually around $0.1\mu(E_f)$ to $1\mu(E_f)$ whereas the peak region has $\mu(E_i)$ around 5 to 10 times $\mu(E_f)$. Based on these considerations, we plotted IPFY^r/IPFY^s ratio versus dimensionless surface roughness size $A*\mu(E_f)$ for two different geometries in figure 2.7. The choice of those two geometries was based the detection geometries in experimental setup.
In figure 2.7a, we have a normal incidence geoemtry. In all selected energies, IPFY inten-

sities are growing quickly when we firstly increase roughness size. After roughness level reaches about $4/\mu(E_f)$, IPFY intensities cease to grow and tend to level themselves with corresponding scaling factors. At fixed surface roughness size, the scaling factors is increasing with the increase of $\mu(E_i)$.
When we changed the geometry to regular incidence, the results are quite different. The IPFY intensity is decreasing at low $\mu(E_i)$ but increasing at high $\mu(E_i)$ when increase roughness. In the intermediate stage, for instance, $\mu(E_i)$ is half of $\mu(E_f)$, IPFY intensity is initially decreasing up to $A = 2/\mu(E_f)$ and then increasing monotanically with roughness size. This indicates a crossover between IPFY measured from a rough surface and a smooth surface.
Combine both situations, we can see that distortions on IPFY is most sensitive around the roughness size comparable to emission x-ray penetration length $1/\mu(E_f)$.

2.5.4 Energy dependence of surface roughness effect on IPFY

The energy dependence study of surface roughness effect on IPFY is the most significant since it can be directly used to intepret measured IPFY spectra. As shown in figure 2.8, when we have normal incidence geometry, IPFY intensities grow monotonically with respect to the increase of $\mu(E_i)$ for all roughness sizes. In terms of real IPFY spectra, since $\mu(E_i)$ is small around pre-edge and post-edge region and large around peak region, such result indicates small distortions around pre-edge and post-edge regions but big distortions around peak regions. For roughness size as small as $0.1/\mu(E_f)$, IPFY intensities nearly stay the same as smooth IPFY in regardless of energies.
As we look at regular incidence geometry, the effect is quite different around $\mu(E_i)$ less than $1\mu(E_f)$ region but similar when $\mu(E_i)$ is bigger than $2\mu(E_f)$. IPFY obtained from rough surfaces at all selected roughness sizes have crossovers with smooth IPFY at small $\mu(E_i)$. It indicates that crossovers may be observed in the pre-edge and post-edge regions but not peak regions when compared to smooth surface IPFY and rough surface IPFY. For same surface roughness size, the distortions from regular incidence is generally smaller than normal incidence. In regular incidence geometry, we have plateaus around $\mu(E_i)$ bigger than $4\mu(E_f)$ which corresponds to our normal peak regions, it implies that IPFY spectra will only be scaled around peak regions and no distortions will occur.
In general, when surface roughness size is small enough, we will see no distortions on IPFY spectra as expected. As to accurately determine the maximum of this distortion free roughness size, the investigations on geometry dependence is necessary since the geometry dependence of surface roughness effect is big as stated above. In addition, one more conclusion we can draw from this section is that for certain geometry, the effect of surface



(a) (b)

Figure 2.8: (a) The energy dependence of sine wave surface roughness effect on IPFY at roughness size as $0.1/\mu\left(E_f\right)$, $0.5/\mu\left(E_f\right)$, $1/\mu\left(E_f\right)$, $5/\mu\left(E_f\right)$, $10/\mu\left(E_f\right)$ with geometry α, β to be $89.9\,^\circ$ and $41.6\,^\circ$, respectively. (b) The energy dependence of sine wave surface roughness effect on IPFY at roughness size as $0.1/\mu\left(E_f\right)$, $0.5/\mu\left(E_f\right)$, $1/\mu\left(E_f\right)$, $5/\mu\left(E_f\right)$, $10/\mu\left(E_f\right)$ with geometry α, β to be $60\,^\circ$ and $61.5\,^\circ$, respectively.

roughness can be reduced.

2.5.5 Geometry dependence of surface roughness effect on IPFY

From our discussions in section 2.5.4, for fixed roughness size, the biggest distortion would occur at biggest $\mu\left(E_i\right)$. To find the optimal detection geometry and maximum allowable roughness size, in figure 2.9, we plotted the percentage error of rough surface IPFY versus α and β at chosen roughness sizes for maximum $\mu\left(E_i\right) = 10\mu\left(E_f\right)$.
If we let 5% be our critical distortion error, from figure 2.9a, there were no distortions for surface roughness size A to be $0.1/\mu\left(E_f\right)$. When we increased the roughness size up to $0.3/\mu\left(E_f\right)$, distortion free regions were largely reduced and mainly located around α and β both less than $40\,^\circ$ area and $\alpha \approxeq 60\,^\circ$ and $\beta < 40\,^\circ$ area. If we further increase surface roughness size to be $1/\mu\left(E_f\right)$, there was almost no distortion free area except a very narrow region where α and β are both no less than $80\,^\circ$. Combine all three plots, we concluded that the biggest distortion happen in area where $\alpha > 70\,^\circ$ and $\beta < 50\,^\circ$, therefore our regular normal incidence geometry should be avoided.

In addition, we calculated ratio $\mathrm{IPFY}^r/\mathrm{IPFY}^s$ over surface roughness range up to $10/\mu\left(E_f\right)$

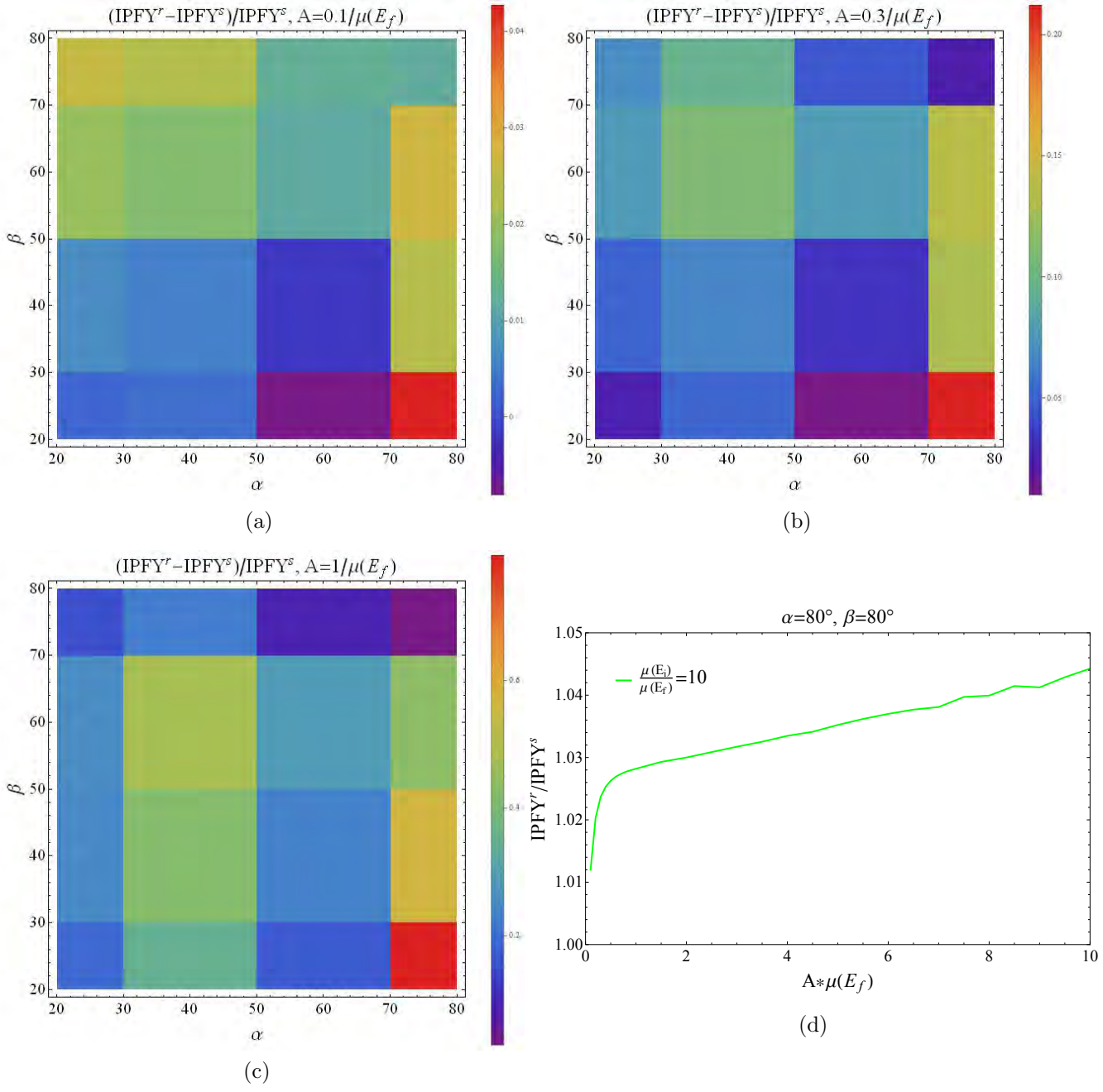


Figure 2.9: (a) (b) (c) Geometry dependence mesh of the absolute percentage difference $(\mathrm{IPFY}^r - \mathrm{IPFY}^s)/\mathrm{IPFY}^s$ with α and β varies from 20° to 80° with 20° step size with surface roughness size to be $0.1/\mu(E_f)$, $0.3/\mu(E_f)$, $1/\mu(E_f)$, respectively. The $\mu(E_i)$ is fixed to be $10\mu(E_f)$. (d) Surface roughness dependence of $\mathrm{IPFY}^r/\mathrm{IPFY}^s$ over roughness size range from $0.1/\mu(E_f)$ to $10/\mu(E_f)$ with $\mu(E_i)/\mu(E_f)$ fixed as 10 with α and β to 80°.

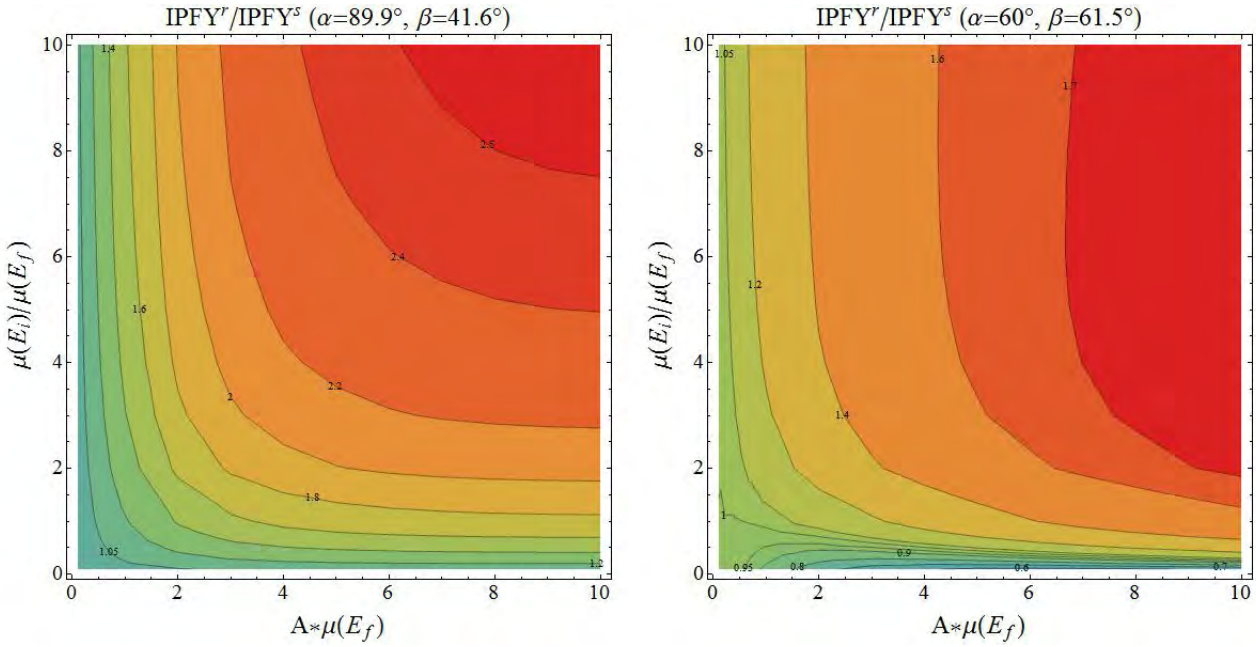
α \ β	20 °	40 °	60 °	80 °
20 °	$0.439/\mu(E_f)$	$0.294/\mu(E_f)$	$0.203/\mu(E_f)$	$0.198/\mu(E_f)$
40 °	$0.296/\mu(E_f)$	$0.261/\mu(E_f)$	$0.181/\mu(E_f)$	$0.170/\mu(E_f)$
60 °	$0.484/\mu(E_f)$	$0.364/\mu(E_f)$	$0.224/\mu(E_f)$	$0.325/\mu(E_f)$
80 °	$0.109/\mu(E_f)$	$0.157/\mu(E_f)$	$0.143/\mu(E_f)$	$>10/\mu(E_f)$

Table 2.1: The maximum surface roughness sizes calculated from different geometries in term of units $1/\mu(E_f)$, that guaranteed the distortions of IPFY over range $\mu(E_i)/\mu(E_f)$ between 0.1 to 10 from a sine wave rough surface is no more than 5%.

at $\alpha = \beta = 80\,^\circ$ as shown in figure 2.9d, it turned out that within the physical range we are interested in, we will always have distortion free measurement. Therefore, nearly normal incidence and emission geometry will guarantee distortion free measurement of IPFY in regardless of roughness size.
In order to find the maximum allowable roughness size for all detection geometries, in table 2.1, we tabulated maximum roughness size for each geometry by setting the percentage error to be 5% at $\mu(E_i) = 10\mu(E_f)$. The angle mesh we calculated did cover a reasonable angle range, and it revealed that the maximum distortion free roughness size is $0.109/\mu(E_f)$ in regardless of detection geometry. However, at optimal detection geometry other than nearly normal incidence and emission, the critical surface roughness size can be optimized to $0.484/\mu(E_f)$.

At the end of the numerical work, we would like to discuss about the combined effect of roughness size and energy in two particular geometries in a wider range. As stated before, we defined 5% as our critical distortion tolerance. From figure 2.10, we can see that regular incidence geometry has bigger distortion free area than normal incidence geometry and therefore proved itself as a better detection geometry. In normal incidence geometry, for surface roughness size smaller than $2/\mu(E_f)$ and $\mu(E_i) > 3\mu(E_f)$ area, we can see the gradient of calculated $\mathrm{IPFY}^r/\mathrm{IPFY}^s$ tend to be 0 at any chosen roughness size. This implies that in a large region around peak, IPFY is only scaled by some constant but not distorted. For regular incidence geometry, when $\mu(E_i) > 3\mu(E_f)$, we would always have distortion free IPFY regardless of surface roughness size.
Another important aspect from figure 2.10b is that we have regions that IPFY from rough surface can be either bigger or smaller than smooth surface IPFY. This clearly indicates a crossover between IPFY from rough surface and IPFY from smooth surface at certain energy. However, this phenomenon is only observable when we have surface roughness size

bigger than $1/\mu(E_f)$.



(a) (b)

Figure 2.10: (a) Contour plot of IPFY^r/IPFY^s from a sine wave rough surface as a function of $\mu(E_i)/\mu(E_f)$ and $A*\mu(E_f)$ with geometry α, and β to be 89.9° and 41.6°, respectively. (b) Contour plot of IPFY^r/IPFY^s from a sine wave rough surface as a function of $\mu(E_i)/\mu(E_f)$ and $A*\mu(E_f)$ with geometry α, and β to be 60° and 61.5°, respectively.

Chapter 3

Experimental Demonstration of Surface Roughness Effect on IPFY

3.1 Details of measurement

The measurements described in this chapter were performed at the Canadian Light Source's High Resolution Spherical Grating Monochromator (SGM) 11ID-1 beamline. In SGM, a picoammeter is used to measure total electron yield (TEY) by drain current mode. Total fluorescence yield (TFY) is measured on a Micro-Channel Plate (MCP) detector, and partial fluorescence yield (PFY), inverse partial fluorescence yield (IPFY) are measured by one PGT and four Amptek silicon drift detectors (SDD). The pressure maintained in the main chamber is around 10^{-9} Torr.

3.2 IPFY spectroscopy

3.2.1 $NdGaO_3$

The $NdGaO_3$ single crystal was obtained from MTI Corporation. It is specified that the dimension of the sample is 10 mm $\times$ 10 mm $\times$ 0.5 mm with surface roughness size less than 5 Å, and its $\langle 100 \rangle$ direction is normal to sample surface. The $NdGaO_3$ single crystal is then cut into 8 almost equal size pieces by a diamond saw and polished to several

different roughness sizes by lapping films and sand papers. The surface roughness sizes are characterized by AFM. All the sample preparation details can be found in Appendix D.

3.2.2 Penetration length of $NdGaO_3$

As stated in our numerical modeling, IPFY is most sensitive to surface roughness size around the penetration length of emission x-rays. To check how our polished roughness sizes compare to the penetration length of $NdGaO_3$, we plotted the penetration length over 800 eV to 1100 eV in figure 3.1. The penetration length at chosen energy E_i is simply the inversion of absorption coefficient at that energy, for instance, $1/\mu(E_i)$. The absorption coefficient we used to derive penetration length in figure 3.1 is from reference [1].

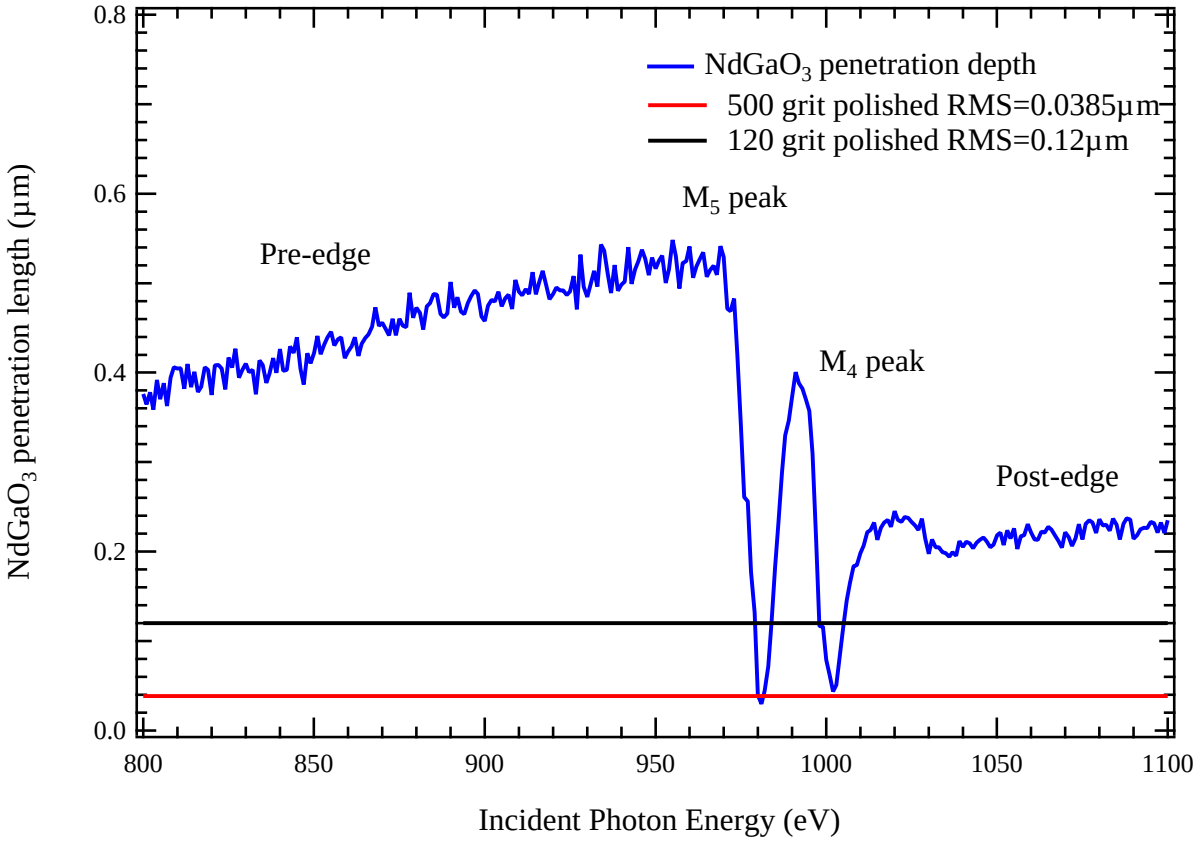


Figure 3.1: X-ray penetration depth of $NdGaO_3$ over energy range 800 eV to 1100 eV. The pre-edge, Nd M_5, Nd M_4, post-edge regions are shown on the figure.

All the samples are charaterized by AFM and details are shown in Appendix D. As characterized by AFM, 500 grit polished sample (red solid line) has roughness size 0.0385 μm which is $0.134/\mu(E_f)$ where we collect PFY from oxygen K emission ($E_f = 524.9eV$). The corresponding absorption coefficient $\mu(E_f)$ of $NdGaO_3$ at this energy is $3.48659\mu m^{-1}$ with density 7.57 g/cm^3 [35, 36]. As compared to $NdGaO_3$ penetration length, we saw it barely touched Nd M_5 peak so the impact range would be very narrow. Similarly, 120 grit polished sample (solid black line) has roughness size 0.12 μm which is $0.418/\mu(E_f)$. It did cover a appreciable region across both Neodymium $M_{5,4}$ peak, so we would expect the distortion on IPFY happen in a wider region if there is any.

3.2.3 X-ray fluorescence and PFY

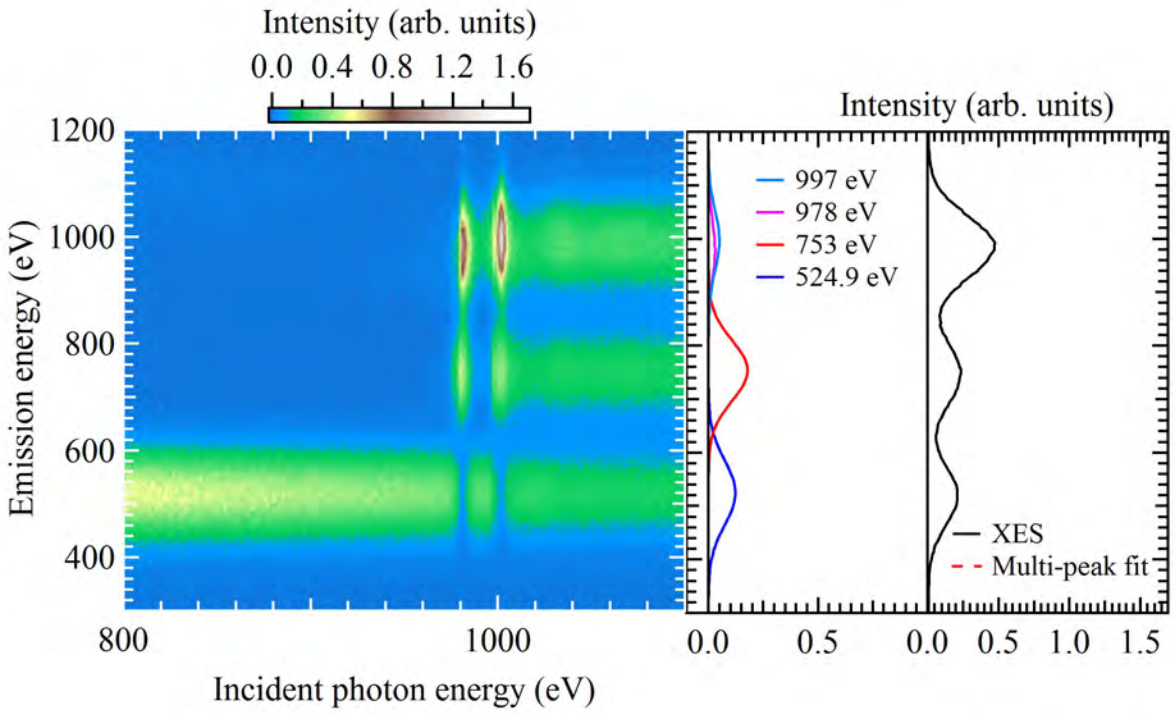


Figure 3.2: $NdGaO_3$ x-ray fluorescence (left panel) and its characteristic emission profile (right panel) over energy range from 800 eV to 1100 eV.

We measured both wide energy range from 800 eV to 1100 eV with stepsize 1 eV and narrow energy range from 960 eV to 1020 eV with energy step 0.1 eV. In figure 3.2, we

showed the x-ray fluorescence (XRF) of smooth surface $NdGaO_3$ from normal incidence geometry on the left panel and its emission line profile on the right panel. We used multi-peak fitting to fit 4 gaussians at characteristic x-ray emission energies for Nd and O between 800 eV to 1100 eV. The sum of those four gaussians agrees with x-ray emission spectroscopy (XES) extracted at $E_i = 1150eV$ where all characterisitic x-rays contribute to emission. All the x-ray emission transition line details are tabled in table 3.1.

Emission line	Energy (eV)	Transition
O K_{α_1}	524.9	$L_3 \rightarrow K$
Nd M_ζ	753	$N_3 \rightarrow M_5$
Nd M_α	978	$N_{6,7} \rightarrow M_5$
Nd M_β	997	$N_6 \rightarrow M_4$

Table 3.1: Characterisitic x-ray emission lines for $NdGaO_3$ over energy range 500 eV to 1100 eV [11].

3.2.4 IPFY spectroscopy on rough surface $NdGaO_3$ samples

In this section, we will show the experimental results of IPFY from 500 grit polished, 120 grit polished and smooth surface $NdGaO_3$ samples at three different detection geometries. The correponding simulations from sine wave modeling are discussed as well.

For normal incidence geoemtry of 500 grit polished sample, the IPFY spectrum was unexpectedly greatly offset from the smooth surface results, this was later found to due to the instability of experimental conditions, e.g., the movement of beamspot on grid, rather than surface roughness effect alone (see Appendix E). In order to see whether there was any distortions happened on its IPFY spectrum, we scaled its IPFY spectra to match the pre-edge of smooth surface by a factor of 1.1. From figure 3.3a, we can see that there is no distortion and which is consistent with our simulation from sine wave model as shown in figure 3.3b. When we change the detection geometry to grazing incidence, the IPFY of 500 grit polished $NdGaO_3$ is also scaled by a factor of 1.1 due experimental conditions as shown in figure 3.3c. The invariance of the scaling factor under two different geometries implies that this scaling factor really comes from experimental instability. We still saw no distortion on 500 grit polished sample, which is reasonable because when the roughness size is small, surface roughness effect is small and not sensitive to geometry change. At the tip of Nd M_5 peak, rough surface IPFY intensity is slightly greater than smooth surface IPFY for both detection geometries and such result is consistent with our calculations.

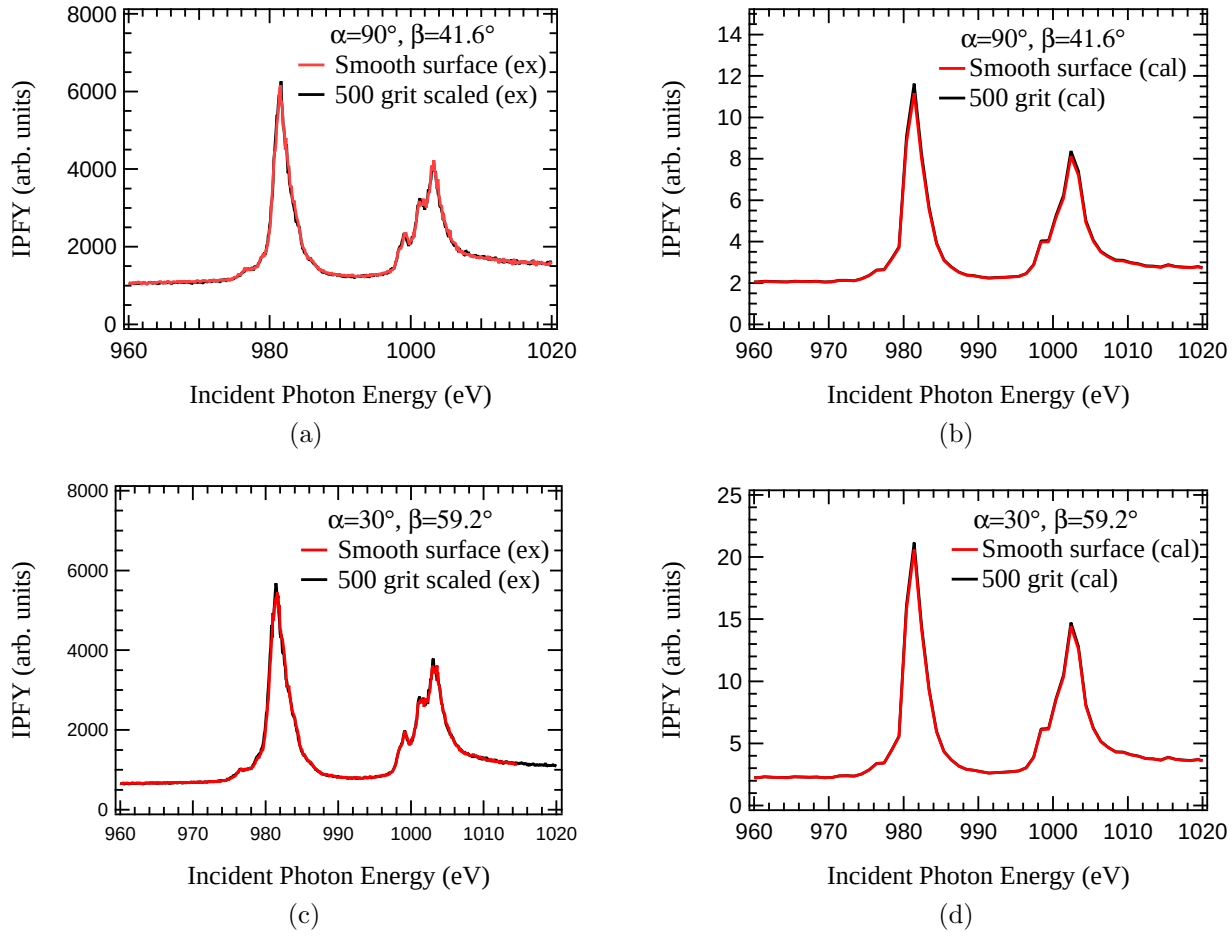


Figure 3.3: (a) Raw IPFY spectrum from 500 grit polished $NdGaO_3$ is scaled by a factor 1.1 at geometry α, β to be 90 ° and 41.6 °, respectively. (b) Rough surface and smooth surface IPFY calculated from sine wave model by using RMS of 500 grit polished sample at normal incidence detection geometry.(c) Raw IPFY spectrum from 500 grit polished $NdGaO_3$ is scaled by a factor 1.1 at geometry $\alpha = 30\,°$, $\beta = 59.2\,°$. (b) Rough surface and smooth surface IPFY calculated from sine wave model by using RMS of 500 grit polished sample at grazing incidence detection geometry. The absorption coefficent data used in sine wave calculation are from reference [1].

For normal incidence geometry of 120 grit polished sample, we saw distortions across almost the whole spectrum except for the pre-edge region in figure 3.4a. We can see that the distortion from rough surface reduced the intensity of IPFY with respect to smooth surface results and the distortions are the strongest around peak regions. In our calculations shown in figure 3.4b, the predicted IPFY from rough surface is greater than smooth surface IPFY which is different from what was found experimentally. However, the magnitude of distortion we calculated from sine wave model is consistent with the experimental result as shown in figure 2.5c. One plausible reason for this is that in our simulation for surface roughness effect on IPFY, we only used a single parameter roughness size to characterize rough surface profile. Therefore, it loses other features from a rough surface, such as rough particle shape, lateral correlation lengths. Fortunately, our main object is to see how much distortion surface roughness effect would cause on IPFY rather than the absolute intensity of IPFY.

To explore the geometry dependence of surface roughness effect, we also measured IPFY of 120 grit polished $NdGaO_3$ at regular incidence geometry. At this geometry, from figure 3.5a the distortions on IPFY are reduced when compared with normal incidence case as shown in figure 3.4a. The decrease in the distortion is most obvious around post-edge region where the distortion vanishes in this detection geometry. These changes were subsequently observed in our calculations shown in figure 3.5b, but the predicted absolute intensity of rough surface IPFY disagrees with experimental results. Nevertheless, our sine wave model calculation well captured the magnitude of distortion from surface roughness effect at this detection geometry as shown in figure 3.5c. From the comparison with normal incidence geometry, we clearly saw that regular incidence geometry is a better detection geometry than normal incidence geometry as to reduce surface roughness effect.

In conclusion, our sine wave model managed to quantitatively predict the magnitude of distortion caused by surface roughness effect. However, the features of a real rough surface cannot be fully described by a single roughness size parameterization which evident in the failure of our sine wave model in predicting the trend of the change in IPFY intensity for 120 grid polished sample. Nevertheless, the success in applying sine wave model to anticipate the degrees of distortion in IPFY enabled us to determine the maximum allowable surface roughness size and optimal detection geometry.

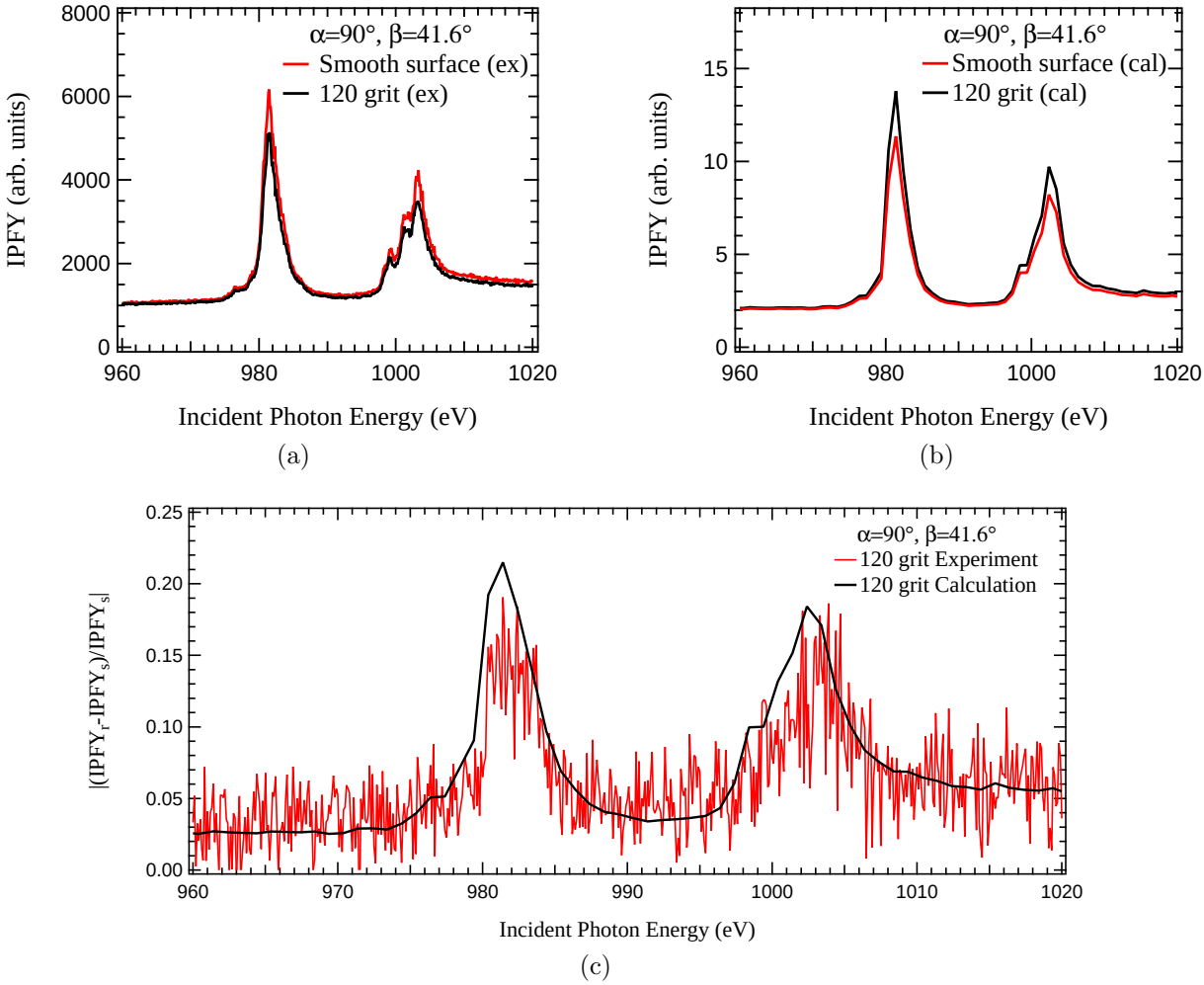


Figure 3.4: (a) IPFY spectra from a 120 grit polished $NdGaO_3$ and smooth surface $NdGaO_3$ at geometry α, β to be 90 ° and 41.6 °, respectively. (b) Rough surface and smooth surface IPFY calculated from sine wave model by using RMS of 120 grit polished sample at normal incidence detection geometry. (c) The percentage differece between smooth surface IPFY and rough surface IPFY from experiments and calculations. The absorption coefficent data used in sine wave calculation are from reference [1].

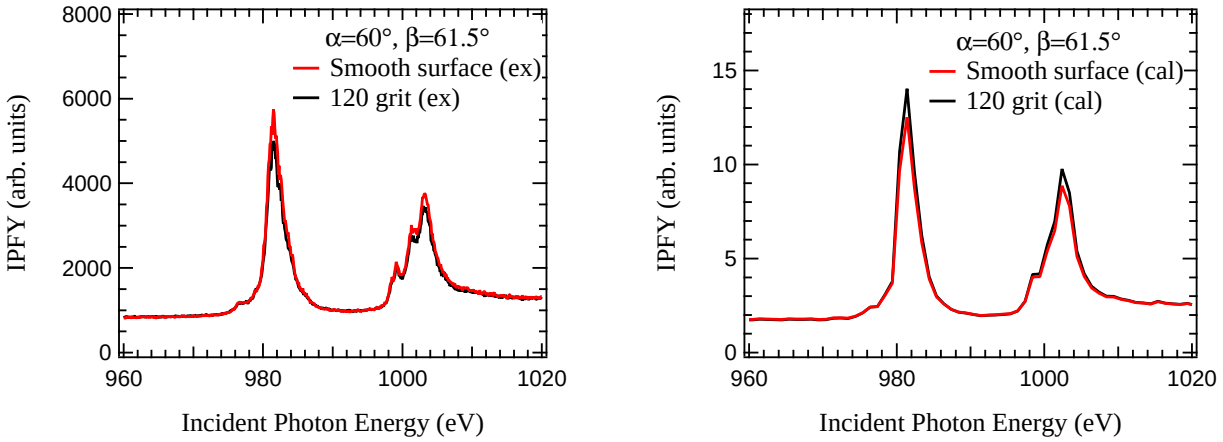


Figure 3.5: (a) IPFY spectra from a 120 grit polished $NdGaO_3$ and smooth surface $NdGaO_3$ at geometry α, β to be 60 ° and 61.5 °, respectively. (b) Rough surface and smooth surface IPFY calculated from sine wave model by using RMS of 120 grit polished sample at regular incidence detection geometry. (c) The percentage differece between smooth surface IPFY and rough surface IPFY from experiments and calculations. The absorption coefficent data used in sine wave calculation are from reference [1].

Chapter 4

Granularity effect on IPFY

4.1 Granularity effect

When homogeneous single crystals are not available for the study of IPFY, powder specimens become our only choice. For this reason, the test on the applicability of IPFY on porous samples becomes very important. According to Suortti, the measurement of x-ray fluorescence intensity from compressed powder specimens would suffer from both surface roughness effect and porosity effect, and such combined effect is termed as granularity effect. [33] The study of granularity effect is more complicated than surface roughness effect, and even to setup a reasonable model for numerical simulations are very difficult. In this chapter, we will only qualitatively discuss about granularity effect on IPFY.
In general, we could categorize granularity effect into three sub scenarios:

1 For a bulk rough surface sample, we would have surface roughness effect but no porosity effect.

2 For ideally polished compressed powder specimens, there will be no surface roughness effect and we only have porosity effect.

3 For general powder specimens, we would have combined effects from surface roughness and porosity.

4.2 Randomly distributed rough surface

For case 1, we will discuss a special situation where we have a randomly distributed surface. Usually for a real rough surface, we would intuitively think that surface roughness is randomly distributed and the roughness height distribution can be described by a normal distribution function. This thinking was found to be true from our characterization of $NdGaO_3$ rough surfaces in Appendix D.2. However, this randomly distribution of roughness height cannot fully pass on to $G(z, A, x)$ due to the cutoff from rough layer. In a manner similar to $G(z, A, x)$ calculated from a sine wave rough surface, for the rough layer we must have type I $G(z, A, x)$ that is a complex outcome of rough surface. In the bulk, we would have type II $G(z, A, x)$ that is linearly transformed from rough surface profile which reflects the distribution of roughness height. However, the dominant contribution is from the rough layer part rather than the bulk part whose $G(z, A, x)$ contains the information about the rough surface profile. In conclusion, for a randomly distributed rough surface, an analytical expression for surface roughness effect on IPFY by invoking the random distribution of rough surface height cannot be realized.

4.3 Porosity effect

In case 2, we have an ideally polished randomly packed powder specimen, the structure incident x-rays probe is similar at any depth z. In this situation, we only a type II $G(z, L, x)$ due to the porosity from random packing where L stands for the average chord length inside the specimen. Since random packing can only be described properly in a statistical way, it is reasonable to assume its random nature can pass on to our type II $G(z, L, x)$. Instead of calculating position dependent $G(z, L, x)$ numerically, we now can treat $G(z, L, x)$ statistically as average G_{avg} which is described by a normal distribution function. Following this assumption, we can write (2.12) for an ideally polished randomly packed powder specimen as:

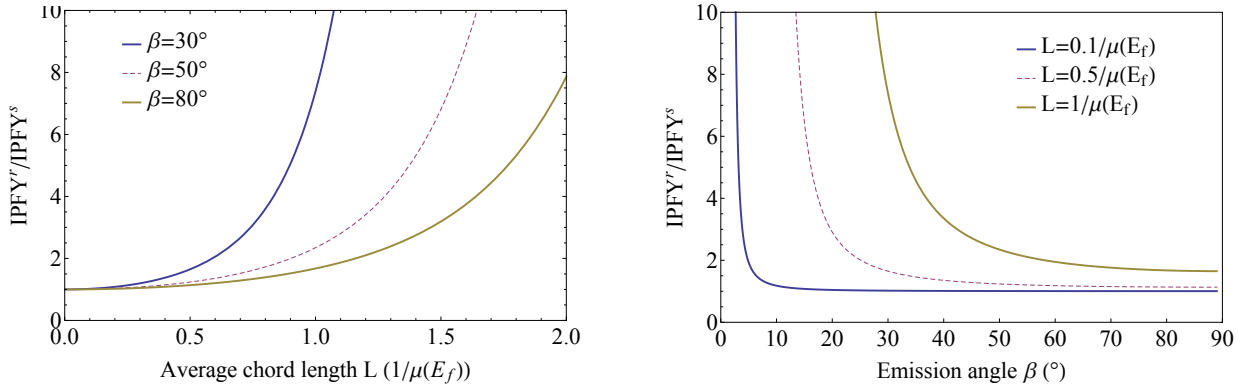
$$\frac{\mathrm{IPFY}_r}{\mathrm{IPFY}_s} = e^{\frac{\mu(E_f)}{\sin\beta} G_{avg}(L)} \tag{4.1}$$

Formula (4.1) implies that $\mathrm{IPFY}_r/\mathrm{IPFY}_s$ is independent of incident energies E_i and incident angle α, so IPFY spectrum will only be scaled by a constant factor whereas the lineshape preserves. For IPFY spectroscopy, we always measure at fixed emission energy

so that $\mu(E_f)$ would be constant for all subsequent measurements.[1] The scaling factor will only depend on emission angle β and average chord length L.
To incorporate the random nature of packing into our modeling, we will rewrite formula (4.1) as:

$$\frac{\text{IPFY}_r}{\text{IPFY}_s} = \int_{-\infty}^{+\infty} \frac{1}{\sqrt{2\pi}L} e^{-\frac{x^2}{2L^2}} e^{\frac{\mu(E_f)}{\sin\beta}x} dx \tag{4.2}$$

$$= e^{\frac{\mu(E_f)^2 L^2}{2\sin^2\beta}} \tag{4.3}$$



(a) (b)

Figure 4.1: (a) Avergae chord length dependence of porosity effect at emission angle 30 °, 50 °, 80 °, respectively. (b) Emission angle β dependence of porosity effect with average chord length to be $0.1/\mu(E_f)$, $0.5/\mu(E_f)$, $1/\mu(E_f)$, respectively.

In order to evaluate how big the porosity effect is, we followed formula (4.3), and plotted the average chord length dependence and emission angle dependence of the effect in figure 4.1a and figure 4.1b, respectively. From figure 4.1a, for any given emission angle β, we can see that the scaling factor is increasing when the average chord length increases. The growth rate of $\text{IPFY}^r/\text{IPFY}^s$ is bigger when emission angle is smaller. As to the emission

[1] The composition of the material is the same across all the measurements.

angle dependence, for any given average chord length, the scaling factor is decreasing while we increase emission angle β. The rate of changing in scaling factor tends to decrease towards bigger emission angle and eventually settle as zero at normal emission angle. At normal emission angle, the amount of scaling grows with respect to average chord length. In this sense, a bigger emission angle would be a better detection geometry for smooth porous sample.

4.4 General granularity effect

In reality, our common polishing procedures generally fail to produce a perfectly polished surface. Therefore, there will be more or less surface roughness effect on IPFY spectroscopy. From our calculations shown in figure 4.1b and figure 2.7, for the same surface roughness size and average chord length, the effect from porosity is much bigger than effect from rough surface. For a given detection geometry, porosity effect from random packing will give us big a scaling factor that is independent of incident energy E_i. On top of that, surface roughness effect which depends on incident energy will distort IPFY spectra by a relatively small amount based on the actual structure of the open pores.
In this sense, distortions on IPFY performed on porous specimen only come from surface roughness effect, so that the minimization of surface roughness effect will eventually minimize distortions from granularity effect. In our previous study of surface roughness effect on IPFY, we learned that surface roughness effect would vanish when we polish rough surface to our critical roughness level or set our detection geometry to be nearly normal incidence and normal emission. If our model for randomly packed porous specimen worked well and it is possible to have distortion free IPFY measure on powder specimen, however, since IPFY spectra are still scaled by some constants therefore cannot be used to quantitatively obtain absorption coefficients. This would eventually leads to the failure of composition analysis on powder specimen.
In subsequent section, we will illustrate some results of IPFY performed on $NdGaO_3$ powder specimen and we will only qualitatively comment on the experimental results in regards of our discussions.

4.5 IPFY spectroscopy on $NdGaO_3$ powder specimen

In figure 4.2a and 4.2c, we plotted the comparison of smooth surface $NdGaO_3$ IPFY and porous $NdGaO_3$ IPFY at normal incidence and regular incidence respectively. We can see clearly from both geometries that IPFY intensity from powder specimen is much bigger than smooth surface. This result is consistent with what we argued before, the major contribution of granularity effect is from porosity effect and the IPFY intensity from porosity effect is predicted to be always greater than smooth surface IPFY. As to see how much distortion caused by granularity effect, we scaled the powder specimen IPFY to match up with smooth surface pre-edge IPFY intensity as shown in figure 4.2b and 4.2d, respectively. If this scaling factor can be approximately treated as the effect from porosity alone, and we can see the scaling factor from $\beta = 41.6\,^\circ$ is $1/0.67 = 1.49$ which is bigger than the scaling factor from $\beta = 61.5\,^\circ$ (1.39). Such a result also agreed with our prediction for emission angle dependence of porosity effect on IPFY.
In both geometries, we can see appreciable distortions caused by surface roughness effect. The overall effect decreases the IPFY intensity with respect to smooth surface in regular incidence geometry, whereas in normal incidence geometry two IPFY spectra crossover each other at several different energies. In this sense, regular incidence geometry is a better detection geometry than normal incidence geometry. Previously, we saw distortions caused by surface roughness effect alone is bigger in normal incidence geometry than regular incidence and thus proved regular geometry a better detection geometry. In conclusion, we can possibly make distortion free IPFY measurements on porous specimen by better polishing and choosing optimal detection geometry. We can benefit from our numerical work in modeling surface roughness effect to find critical scale of polishing and optimal detection geometry for IPFY measurement on porous specimen.

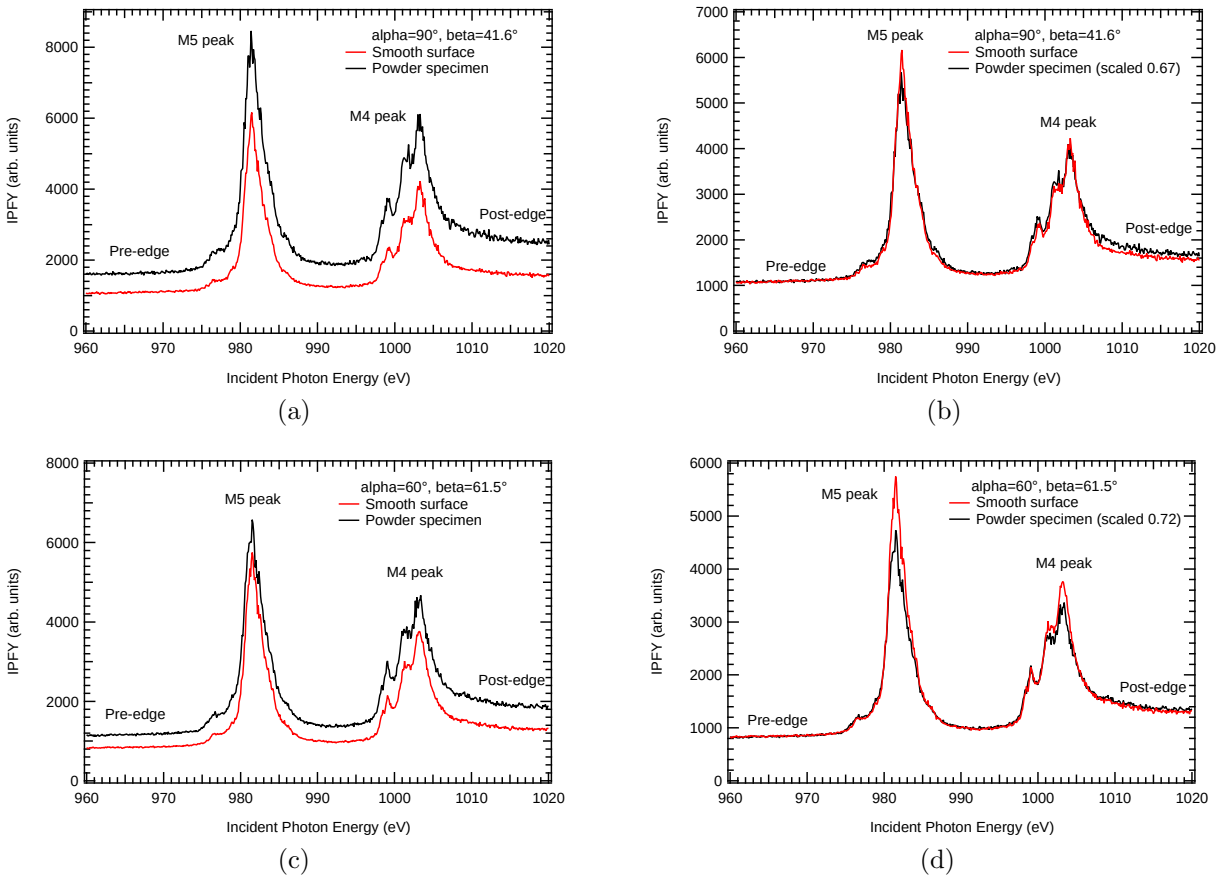


Figure 4.2: (a) IPFY spectra from $NdGaO_3$ powder specimen and smooth surface $NdGaO_3$ at geometry α, β to be 90° and 41.6°, respectively. (b) Raw IPFY spectrum $NdGaO_3$ powder specimen is scaled by 0.67 at geometry α, β to be 90° and 41.6°, respectively. (c) IPFY spectra from $NdGaO_3$ powder specimen and smooth surface $NdGaO_3$ at geometry α, β to be 60° and 61.5°, respectively. (d) Raw IPFY spectrum $NdGaO_3$ powder specimen is scaled by 0.72 at geometry α, β to be 60° and 61.5°, respectively.

Chapter 5

Conclusions

5.1 Summary of results

5.1.1 Theoretical work

The IPFY expression for rough surface originates from smooth surface IPFY where the difference is the emission x-ray depth (EXD) is no longer the same as incident x-ray depth (IXD). By introducing a new parameter $G(z, A, x)$ which is the difference between EXD and IXD, we are able to formulize the IPFY expression for rough surface as following:

$$\mathrm{IPFY}_r = \frac{A(E_i)}{\int_{x1}^{x2}\int_0^{\infty} \frac{1}{\sin\alpha} e^{-\left(\frac{\mu(E_i)}{\sin\alpha}z + \frac{\mu(E_f)}{\sin\beta}(G(z,A,x)+z)\right)} dzdx} \tag{5.1}$$

where we will define quantity $A(E_i)$ to be:

$$A(E_i) = \frac{\nu_{Grid}(E_i)}{\frac{\Omega}{4\pi}\eta(E_f)\,\omega_X(E_i, E_f)\,\mu_X(E_i)} \tag{5.2}$$

Therefore to study surface roughness effect on IPFY, we divide IPFY from rough surface to IPFY from smooth surface, we end up with ratio as:

$$\frac{\mathrm{IPFY}_r}{\mathrm{IPFY}_s} = \frac{\int_0^{\infty} e^{-\left(\frac{\mu(E_i)}{\sin\alpha} + \frac{\mu(E_f)}{\sin\beta}\right)z} dz}{\int_{x1}^{x2}\int_0^{\infty} e^{-\left(\frac{\mu(E_i)}{\sin\alpha}z + \frac{\mu(E_f)}{\sin\beta}(G(z,A,x)+z)\right)} dzdx} \tag{5.3}$$

In our numerical calculations for surface roughness effect on IPFY, we firstly build up a sine wave rough surface with peak to peak amplitude and period defined as $2A$, and then evaluate the expression in (5.3) numerically to investigate the roughness size, energy and geometry dependence of surface roughness effect.

From our modeling we found that the distortion on rough surface IPFY generally increases with respect to surface roughness size and saturates when we reach certain roughness level. Depending on the detection geometry, the absolute IPFY intensity from rough surface can be either bigger or smaller than smooth surface. The IPFY intensity of most sensitive surface roughness size comparable to the emission x-ray penetration length is $1/\mu(E_f)$.

For a given surface roughness size, the distortion on IPFY is monotonically increasing versus incident x-ray absorption coefficient $\mu(E_i)$. This implies the peak region where bigger $\mu(E_i)$ will experience much bigger distortion than pre-edge and post-edge where $\mu(E_i)$ is much smaller. The growth rate of distortion is bigger when we have bigger surface roughness size. By comparing distortions from two different detection geometry, we found that regular incidence geometry has less distortion than normal incidence geometry which implies the existence of optimal detection geometry.

In the end, to find the universal distortion free surface roughness size and optimal detection geometry, we explored the geometry dependence of surface roughness effect. We found $0.109/\mu(E_f)$ to be the maximum allowable surface roughness size for all detection geometries for a 5% error tolerance as our tolerance. When we go to an optimal geometry, the critical roughness size can increase up to $0.484/\mu(E_f)$. The evaluation of geometry dependence suggests $\alpha, \beta < 40^\circ$ and $\alpha \approx 60^\circ$ and $\beta < 40^\circ$ areas to be our optimal detection geometries, whereas $\alpha > 70^\circ$ and $\beta < 50^\circ$ area is the geometry we should try to avoid. In particular, we found when $\alpha, \beta > 80^\circ$, we would always have distortion free IPFY measurements.

In our study of IPFY on powder specimen, we found an analytical solution to IPFY on porous specimen in a sub scenario of granularity effect. In the special case where we have smoothly polished randomly packed powder specimen, by assuming our $G(z, L, x)$ can inherit the nature of randomness from packing, we are able to analytically write IPFY from porosity effect alone as:

$$\frac{\text{IPFY}_r}{\text{IPFY}_s} = e^{\frac{\mu(E_f)^2 L^2}{2\sin^2\beta}} \tag{5.4}$$

From (5.4), we can see that IPFY from porosity effects is only scaled by a constant which

does not depend on incident x-ray energy E_i and angle α. Thus means the lineshape of IPFY is preserved over the whole spectrum. Since for IPFY measurement, our emission energy is always fixed so that $\mu(E_f)$ is a fixed quantity. The only dependence of the scaling factor is on average chord length L and emission angle β. Due to the fact that all quantities in expression (5.4) are positive, IPFY intensity from porous specimen will always be bigger than smooth bulk sample and the scaling factor is monotonically increasing with respect to L but decreasing with respect to β.

5.1.2 Experimental demonstrations

For the study of surface roughness effect on IPFY, we prepared a 500 grit polished $NdGaO_3$ with surface roughness size 0.0385 μm as characterized by AFM and a 120 grit polished $NdGaO_3$ with surface roughness size 0.12 μm. For the purpose of understanding our theoretical work, those two surface roughness sizes are converted into units of $1/\mu(E_f)$ as $0.134/\mu(E_f)$ and $0.418/\mu(E_f)$, respectively. The results showed that there is no distortion on 500 grit polished sample in both normal incidence and grazing incidence geometry. Such result agreed very well with our sine wave modeling for this 500 grit polished roughness size. For 120 grit polished sample, we clearly saw distortions in both geometries, and the distortion is much smaller in post-edge region than $Nd\ M_{5,4}$ peak regions. In addition, the distortion is reduced in regular incidence geometry. In both geometries, our numerical calculations well captured the degrees of distortion. However it failed to predict the actual trend of the change in IPFY intensity for 120 grit polished sample. The most sensible reason for this discrepancy is that the single roughness size parameterization cannot fully reflect the structure of a real rough surface. Other factors such as lateral correlation, degrees of bumpiness should be incorported in order to accurately model a real rough surface. Despite the disagreement of the absolute intensity, our sine wave model successfully anticipated the degrees of distortion that occured in every rough sample for both geometries. This argument proves our sine wave model can be reliable in the estimate of maximum allowable roughness size and optimal detection geometry.

For the study of IPFY on porous specimen, we measured IPFY on $NdGaO_3$ powder specimen for two geometries. We did see a big increase in IPFY intensity on powder specimen with respect to smooth bulk sample, which is consistent with our modeling for porosity effect. Moreover, the estimated scaling factor by scaling IPFY from powder specimen to the pre-edge of smooth bulk sample is decreasing while we increase emission angle, our analytical results agree with the experimental results. The distortion is small around pre-edge and post-edge while dominating around $Nd\ M_{5,4}$ peak regions, the consistency of

this observation with our numerical results of surface roughness effect implies that the distortion on porous specimen comes from large open pores on the rough layer. Therefore, when we polish surface roughness size to the allowable surface roughness size or choose nearly normal incidence and emission geometry, it is possible to have distortion free IPFY measure on porous specimen.

5.1.3 Future work

The failure of applying our sine wave model to predict the absolute intensity of 120 polished sample gives us a very good direction to extend my current work to. There are two simple scenarios to explore:

1 Our sine wave model chose the peak to peak amplitude to be the same as the period of sine wave, but the shape of actual rough particles can be different. Therefore, we can still use sine wave model but use different periods to study the shape dependence of rough particles on surface roughness effect.

2 In our model, the number of concave parts and convex parts is the same. However, for a real rough surface, the weight of concave parts and convex parts can be uneven for same roughness size. The exploration of two extremes where we only have concave parts and convex parts and the intermediate combination of both could be very useful.

Experimentally, we only measured IPFY on surface roughness size up to $0.418/\mu\left(E_f\right)$ and the measurement on roughness size equal or bigger than $1/\mu\left(E_f\right)$ would be important in further prove our model. In addition, we can prepare samples by polishing smooth surface samples differently and then test the topography dependence at same roughness level.

For the test on the applicability of IPFY to porous specimen, it is important to test two solutions from our previous discussions for distortion free measurements. One is to prepare a well compressed powder specimen and then polish the surface roughness size down to critical size as predicted in our sine wave model. Then we can measure IPFY on this smoothly polished powder specimen for a series of geometries, the comparison with a smooth bulk sample can be used to test whether there is any distorion and whether the geometry dependence model for porosity works. Another is to prepare a regular powder specimen and leave the surface unpolished, try to measure IPFY from this sample at nearly normal incidence and emission and check whether we will have distortion or not.

References

[1] A. J. Achkar, T. Z. Regier, E. J. Monkman, K. M. Shen, and D. G. Hawthorn, "Determination of total x-ray absorption coefficient using non-resonant x-ray emission," *Scientific Reports*, vol. 1, no. 182, 2011.

[2] D. Giuseppe, "Interaction x-rays-matter." http://www.science.unitn.it/~fisica1/raggi_x/pdf_ppt/intradmat.pdf, July 2013.

[3] L. Gerward, "Basic x-ray interactions with matter," *Imaging Processes and Coherence in Physics Lecture Notes in Physics*, vol. 112, pp. 132–138, 1980.

[4] M. Newville, "Fundamentals of x-ray absorption fine structure." http://cars9.uchicago.edu/xafs_school/APS_2005/Newville_Intro.pdf, July 2013.

[5] E. A. Stern, S. M. Heald, and E. E. Koch, *Basic Principles and Applications of EXAFS*, ch. 10, pp. 995–1014. North-Holland: Addison-Wesley, 1983.

[6] D. C. Koningsberger and R. Prins, "X-ray absorption: Principles, applications, techniques of exafs, sexafs, and xanes," *Chemical Analysis*, vol. 92, 1988.

[7] J. Stöhr and H. Seigmann, *Magnetism: From Fundamentals to Nanoscale Dynamics*. Berlin-Heidelberg: Springer-Verlag, 2006.

[8] A. Thompson, D. Attwood, E. Gullikson, M. Howells, K.-J. Kim, J. Kirz, J. Kortright, I. Lindau, Y. Liu, P. Pianetta, A. Robinson, J. Scofield, J. Underwood, G. Williams, and H. Winick, "X-ray data booklet," Lawrence Berkeley National Laboratory, CA, 2009.

[9] J. Als-Nielson and D. McMorrow, *Elements of Modern X-Ray Physics*. Reading, MA: John Wiley & Sons Ltd., 2001.

[10] F. de Groot and A. Kotani, *Core Level Spectroscopy of Solids*. Boca Raton, FL: CRC Press, 2008.

[11] J. Bearden, "X-ray wavelengths," *Reviews of Modern Physics*, vol. 39, no. 1, pp. 78–124, 1967.

[12] R. Deslattes, E. K. Jr, P. Indelicato, L. de Billy, E. Lindroth, and J. Anton, "X-ray transition energies:new approach to a comprehensive evaluation," *Reviews of Modern Physics*, 2003.

[13] J. Stöhr, *NEXAFS Spectroscopy, volume 25 of Springer Series in Surface Sciences*. Berlin: Springer, 1996.

[14] M. Grioni, J. F. van Acker, M. T. Czyžyk, and J. C. Fuggle, "Unoccupied electronic structure and core-hole effects in the x-ray-absorption spectra of cu_2o," *Physical Review B*, vol. 45, no. 7, pp. 3309–3318, 1992.

[15] D. G. Hawthorn, K. M. Shen, J. Geck, D. C. Peets, H. Wadati, J. Okamoto, S.-W. Huang, D. J. Huang, H. J. Lin, J. D. Denlinger, R. Liang, D. A. Bonn, W. N. Hardy, and G. A. Sawatzky, "Resonant elastic soft x-ray scattering in oxygen-ordered $YBa_2Cu_3O_{6+\delta}$," *Physical Review B*, vol. 84, no. 7, p. 075125, 2011.

[16] D. E. Sayers, E. A. Stern, and F. W. Lytle, "New technique for investigating noncrystalline structure:fourier analysis of the extend x-ray absorption fine structure.," *Phys. Rev. Lett*, vol. 27, no. 18, pp. 1204–1207, 1971.

[17] P. Lee, P. Citrin, P. Eisenberger, and B. Kincaid, "Extended x-ray absorption fine structure-its strengths and limitations as a structural tool," *Reviews of Modern Physics*, 1981.

[18] J. Rehr and R. Albers, "Theoretical approaches to x-ray absorption fine structure," *Reviews of Modern Physics*, 2000.

[19] B. D. Cullity, *Elements of X-ray Diffraction*. Reading, MA: Addison-Wesley, 1956.

[20] J. Jaklevic, J. A. Kirby, M. P. Klein, A. S. Robertson, G. S. Brown, and P. Eisenberger, "Sensitivity enhancement for dilute species and thin films," *Solid State Commun.*, vol. 23, no. 9, pp. 679–682, 1977.

[21] G. Fraser, "The characterisation of soft x-ray photocathodes in the wavelength band 1-300:i. lead glass, lithium fluoride and magnesium fluoride.," *Nuclear Instruments and Methods in Physics Research*, vol. 206, no. 1-2, pp. 251–263, 1983.

[22] R. Fink, R. Jopson, H. Mark, and C. Swift, "Atomic fluorescence yields," *Review of Modern Physics*, 1966.

[23] W. Bambynek, B. Crasemann, R. Fink, and H. Freund, "X-ray fluorescence yields, auger, and coster-kronig transition probabilities," *Review of Modern Physics*, 1972.

[24] J. Hubbell, P. Trehan, N. Singh, B. Chand, D. Mehta, M. Garg, R. Garg, S. Singh, and S. Puri, "A review, bibliography, and tabulation of k, l and higher atomic shell x-ray fluorescence yields," *J. Phys. Chem. Ref. Data*, vol. 23, no. 2, pp. 339–364, 1994.

[25] L. Tröger, D. Arvanitis, K. Baberschke, H. Michaelis, U. Grimm, and E. Zschech, "Full correction of the self-absorption in soft-fluorescence extended x-ray-absorption fine structure," *Phys. Rev. B*, vol. 46, no. 6, pp. 3283–3289, 1992.

[26] S. Eisebitt, T. Böske, J.-E. Rubensson, and W. Eberhardt, "Determination of absorption coefficients for concentrated samples by fluorescence detection," *Phys. Rev. B*, vol. 47, no. 21, pp. 14103–14109, 1993.

[27] A. J. Achkar, T. Z. Regier, H. Wadati, Y.-J. Kim, H. Zhang, and D. G. Hawthorn, "Bulk sensitive x-ray absorption spectroscopy free of self-absorption effects," *Phys. Rev. B*, vol. 83, no. 8, p. 081106, 2011.

[28] A. J. Achkar, "Inverse partial fluorescence yield spectroscopy," Master's thesis, University of Waterloo, 2011.

[29] P. M. de Wolff, "Measurement of particle absorption by x-ray fluorescence," *Acta Cryst.*, vol. 9, pp. 682–683, 1956.

[30] W. K. Kuhn and G. Andermann, "Effects of surface roughness on surface analysis via soft and ultrasoft x-ray fluorescence spectroscopy.," *Applied Surface Science*, vol. 185, no. 1-2, pp. 84–91, 2001.

[31] H. Ebel and C. Poehn, "Quantitative x-ray fluorescence analysis of specimens with rough surfaces:monte carlo approach," *X-Ray Spectrometry*, vol. 18, no. 3, pp. 101–104, 1989.

[32] H. Hermann and M. Ermrich, "Microabsorption of x-ray intensity in randomly packed powder specimens," *Acta Crystallography Section A*, vol. 43, no. 3, pp. 401–405, 1987.

[33] P. Suortti, "Effects of porosity and surface roughness on the x-ray intensity reflected from a powder specimen.," *Journal of Applied Crystallography*, vol. 5, no. 5, pp. 325–331, 1972.

[34] S. K. Sinha and S. Garoff, "X-ray and neutron scattering from rough surfaces," *Phys. Rev. B*, vol. 38, no. 4, pp. 2297–2312, 1988.

[35] C. Chantler, "Detailed tabulation of atomic form factors, photoelectric absorption and scattering cross section, and mass attenuation coefficients in the vicinity of absorption edges in the soft x-ray(z=30-36, z=60-89, e=0.1 kev-10 kev), addressing convergence issues of earlier work," *J. Phys. Chem. Ref. Data*, vol. 29, no. 4, pp. 597–1048, 2000.

[36] J. H. Hubbell and S. M. Seltzer, "Table of x-ray mass attenuation coefficients and mass energy-absorption coefficients." http://www.nist.gov/pml/data/xraycoef/, July 2013.

APPENDICES

Appendix A

Limit of numerical integration depth

In our numerical simulation, we assumed that our bulk sample is thick enough so that x-ray would never transmit through our sample. Theoretically, we have to integrate the depth z to infinity to collect all the contributions. However, in our numerical simulation, we have to consider the computation time, so in our future analysis, we will neglect the contribution that is smaller than 0.1% of the normalized differential intensity. Therefore, by making the exponential part of formula (2.10) equal to 0.1%, we can obtain the upper limit of our integration depth for smooth surface denoted as ${z^s}_{upper}$ below:

$$ {z^s}_{upper} = \frac{6.91}{\left(\frac{\mu(E_i)}{\sin\alpha} + \frac{\mu(E_f)}{\sin\beta} \right)} \tag{A.1} $$

Similarly, the upper integration depth limit for a rough surface denoted as ${z^r}_{upper}$ is decided by equation below:

$$ \frac{\mu\left(E_i\right)}{\sin\alpha} {z^r}_{upper} + \frac{\mu\left(E_f\right)}{\sin\beta} \left({z^r}_{upper} + G^{min}\left(z, A, x\right) \right) = 6.91 \tag{A.2} $$

where $G^{min}\left(z, A, x\right)$ corresponds to the minimum value of $G\left(z, A, x\right)$ among all calculated values.
Rearrange equation (A.2), the ${z^r}_{upper}$ turn out to be:

$$ {z^r}_{upper} = \frac{6.91 - \frac{\mu(E_f)}{\sin\beta} G^{min}\left(z, A, x\right)}{\frac{\mu(E_i)}{\sin\alpha} + \frac{\mu(E_f)}{\sin\beta}} \tag{A.3} $$

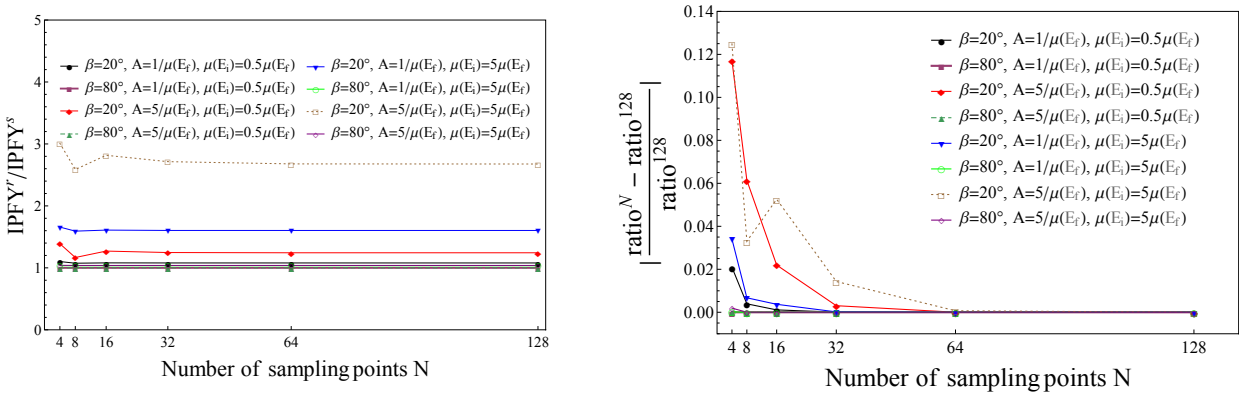
Normally, we would have negative values of $G^{min}\left(z, A, x\right)$, but there are scenarios where

$G^{min}(z, A, x)$ could be positive value and even positive enough to make ${z^r}_{upper}$ negative. In such rare cases, we will set $G^{min}(z, A, x)$ as 0 so ${z^r}_{upper}$ has same expression as ${z^s}_{upper}$.

This integration limit ${z^r}_{upper}$ is of great significance since it defines the cutoff of the $G(z, A, x)$ that we can use to calculate IPFY. Take $G(z, A, x)$ from sine wave rough surface for example, if our ${z^r}_{upper}$ is around $2A$ which corresponds to rough layer part where we have only type I $G(z, A, x)$, the distortion on IPFY would be most prominent. In the opposite, if ${z^r}_{upper}$ is very big or we have very small surface roughness size, for example $> 100A$, where we mainly have type II $G(z, A, x)$, so the distorted contribution from rough layer relative to non-distorted part from bulk will be largely reduced, and the overall distortion on IPFY would be negligible. Invoke this idea to a real IPFY spectra, we will see large distortions at peak regions where we have big $\mu(E_i)$ and corresponding small ${z^r}_{upper}$. Similarly, in pre-edge and post-edge regions, where $\mu(E_i)$ is largely reduced, where the corresponding ${z^r}_{upper}$ will be bigger, so the distortion will be smaller. The geometry dependence of surface roughness effect on IPFY can be understood in means of ${z^r}_{upper}$ as well.

Appendix B

Optimal sampling points



(a) (b)

Figure B.1: (a) IPFY^r/IPFY^s as a function of sampling points N with incident angle 85 °, and emission angle 20 ° and 80 °, surface roughness size $1/\mu\,(E_f)$ and $5/\mu\,(E_f)$ and linear attenuation coefficient at incident energy E_i as $0.5/\mu\,(E_f)$ and $5/\mu\,(E_f)$. (b) The percentage error of ratio IPFY^r/IPFY^s from different sampling points number N with respect to samlping points number 128 at parameters described in (a).

To find the optimal number of sampling points, we calculated ratio IPFY^r/IPFY^s versus number of sampling points by chosen high and low limits of parameter $\mu(E_i)$, β, A at fixed α and $\mu(E_f)$. In order to see quantitatively how the ratio $IPFY^r/IPFY^s$ converge as we increase the number of sampling points, we plotted the percentage difference between IPFY^r/IPFY^s ratio from sampling number N and IPFY^r/IPFY^s ratio from the maximum sampling number 128 in figure B.1b. We see that 32 sampling points has a maximum percentage error less than 2% in all interested physical ranges, but to be more precise, we finally chose 64 sampling points in all our later calculations. In this case, we are able to reduce the biggest percentage error to be less than 0.1%.

Appendix C

Proof of the periodicity of $G(z, A, x)$ from bulk

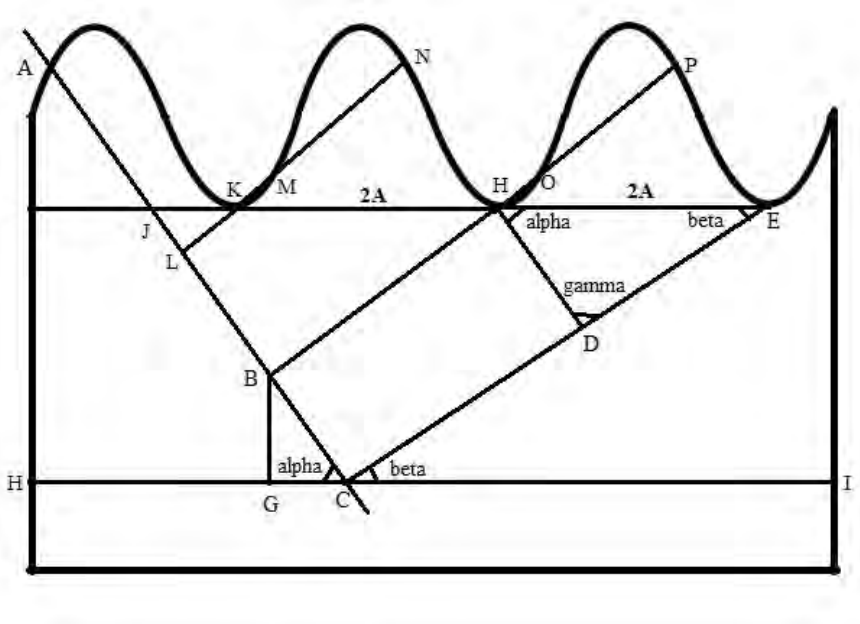


Figure C.1: Schematic of calculating $G(z, A, x)$ contributed from the bulk part from a sine wave rough surface with peak to peak amplitude denoted as $2A$ and period $2A$.

As we probe further into the bulk part over a sine wave rough surface from same starting point A as depicted in figure C.1, since we have same emission angle β and equivalent

position[1] K, H and E, the emission x-ray effective penetration lengths from the rough layer[2] L_{MN}, L_{OP} are the same. Our $G(z, A, x)$ at integration depth L and B are expressed as:

$$G^L(z, A, x) = (L_{LK} + L_{MN}) \sin\beta - (L_{LJ} + L_{AJ}) \sin\alpha \tag{C.1}$$
$$G^B(z, A, x) = (L_{BH} + L_{OP}) \sin\beta - (L_{BJ} + L_{AJ}) \sin\alpha \tag{C.2}$$

Apparently, from figure C.1, the emission and incident penetration depths contributed from the bulk[3] are the same at both position L and position B. Those can be expressed as:

$$L_{LJ} \sin\alpha = L_{LK} \sin\beta \tag{C.3}$$
$$L_{BJ} \sin\alpha = L_{BH} \sin\beta \tag{C.4}$$
$$L_{MN} = L_{OP} \tag{C.5}$$

Combining equation (C.1), (C.2), (C.3), (C.4), (C.5), we can easily obtain:

$$G^L(z, A, x) = L_{MN} \sin\beta - L_{AJ} \sin\alpha = G^B(z, A, x) \tag{C.6}$$

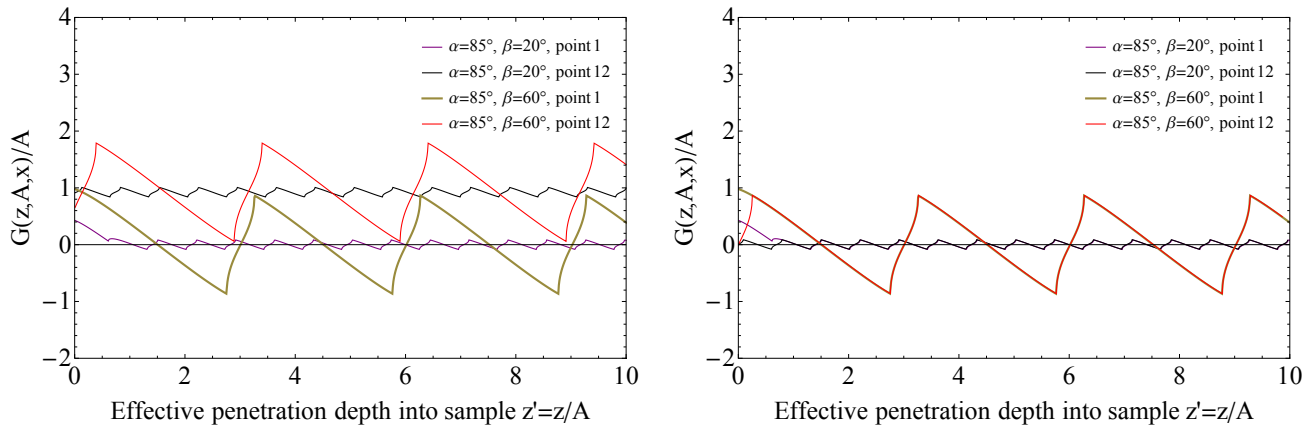
The result derived above not only apply to antinode, for example, K, H, but also to any points on the sine wave rough surface. Such result explains why the $G(z, A, x)$ is periodic when probed into the bulk part.
In addition, the period in $G(z, A, x)$ can be determined analytically. In figure C.1, the period in terms of effective penetration depth is L_{BG}. Since L_{BC} is parallel with L_{HD} and so does L_{BH} AND L_{CD}, BCDH forms a parallelogram. We will have following relationships:

$$L_{BG} = L_{BC} \sin\alpha \tag{C.7}$$
$$L_{BC} = L_{HD} \tag{C.8}$$
$$\frac{L_{HD}}{\sin\beta} = \frac{2A}{\sin\gamma} \tag{C.9}$$
$$\gamma = \pi - \alpha - \beta \tag{C.10}$$

Combining equation (C.7), (C.8), (C.9), (C.10), we will have the period L_{BG} as:

$$L_{BG} = \frac{\sin\alpha \sin\beta}{\sin(\pi - \alpha - \beta)} 2A \tag{C.11}$$

[1]Positions K, H, E have exactly same height and lateral distance between them are integer times of the period $2A$.
[2]The topmost layer which has thickness $2A$.
[3]The part just below the rough layer, alternatively, below height of position K or H.



(a) (b)

Figure C.2: (a) $G\left(z,A,x\right)/A$ calculated from a sine wave rough surface with fixed incident angle α equal to $85\,^{\circ}$ at different exiting angles β equal to $20\,^{\circ}$, $60\,^{\circ}$, when our first intercept point with the rough surface is point 1 and point 12 as depicted in figure 2.2, respectively. (b) By manually moving $G\left(z,A,x\right)/A$ from same geometry but different starting point together, we found the periodic parts coincide with each other very well.

As we can see from (C.11), for fixed geometry α and β, in regardless of where x-ray is incident into the sine wave rough surface, we will always have same periodic structure for same detection geometry. Such result is consistent with what we have calculated in figure C.2.

To see how really $G\left(z,A,x\right)$ change from sine wave rough surface when we sample the rough surface at different starting point but with same geometry, we plotted them in figure C.2. In this situation, rough layer part $G\left(z,A,x\right)$ with same geometries but different starting points are quite different from each other, however, the periodic parts of $G\left(z,A,x\right)$ from the bulk with same geometries coincide with each other in despite of offset and lateral displacement as shown in figure C.2b. This result is consistent with our proof before.

Appendix D

$NdGaO_3$ rough sample preparations and characterizations

D.1 $NdGaO_3$ sample preparations

The 10 mm × 10 mm × 0.5 mm $NdGaO_3$ single crystal is firstly bonded to a cross glass plate by melting crystal bond on top of the surface and cooling down afterwards. After that, the single crystal is cutted into 8 approximate 2.5 mm × 10 mm × 0.5 mm equal size pieces by using a mechanical saw with fine diamond saw bit sawing smoothly for few hours.
As shown in figure D.1, three pieces of $NdGaO_3$ single crystals were polished by 500 grit, 240 grit and 120 grit sand paper with abrasive particle size as 30.2 μm, 58.5 μm and 125 μm, respectively. One piece of $NdGaO_3$ single crystals was polished by a 9 μm lapping film, and another piece was crashed by a pestle inside of a mortar into powder specimen. All the rough surface polishing are polished in random directions evenly for about 0.7 hour to 2 hours. The powder specimen was grinded uniformly for a reasonable period, and its uniformity was checked by a microscope. The piece named texture side is referred to the unpolished side of the original single crystal, which showed texture characteristics under Atomic Force Microscopy (AFM).

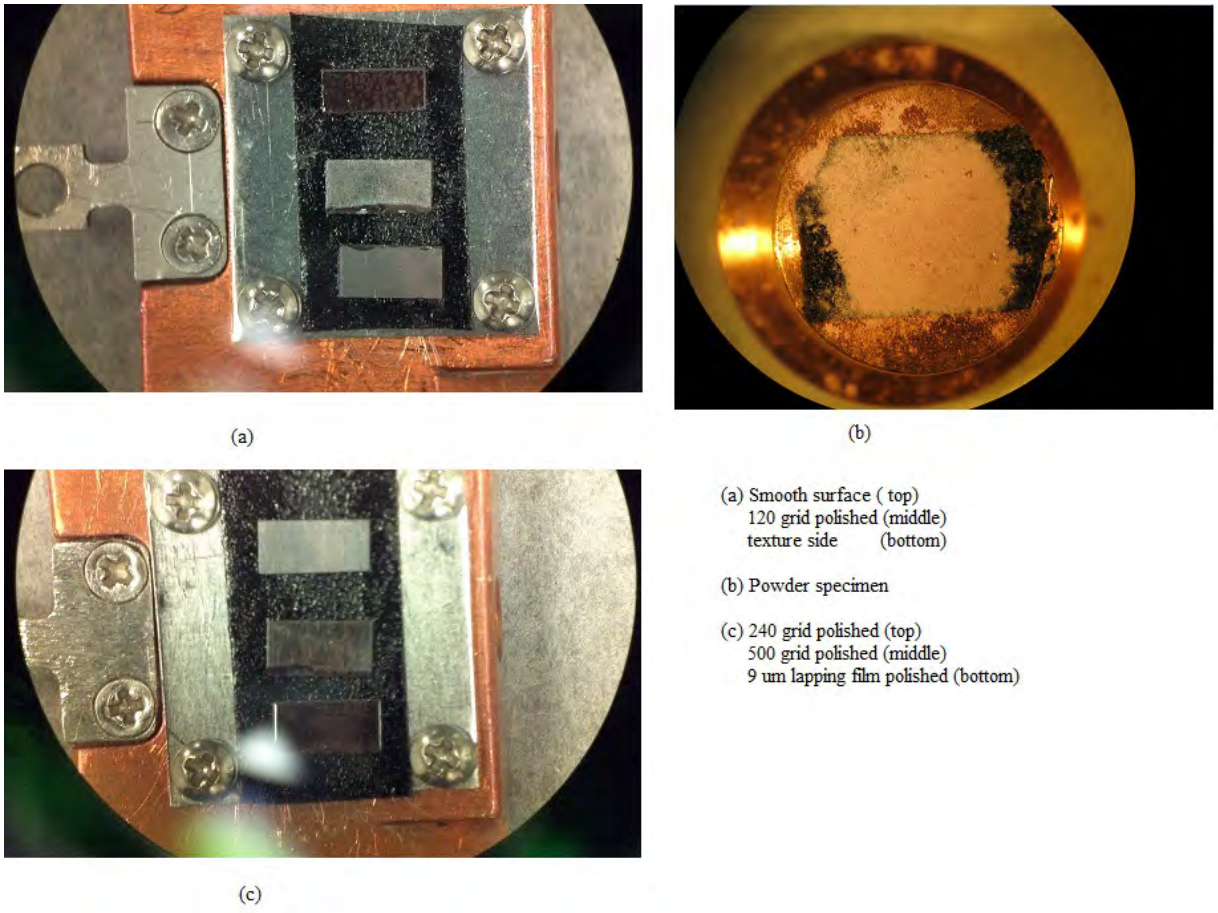


Figure D.1: Rough surface $NdGa_3$ samples produced by using various grits and lapping films to polish smooth surface $NdGaO_3$ samples, and $NdGaO_3$ powder specimen made by using pestle to crash $NdGaO_3$ single crystals in a mortar.

D.2 Characterizations of surface roughness by AFM

AFM is a surface scanning probe microscopy with very high resolution on the order of nanometer, and therefore it satisfied our need fairly well.[1] In figure D.2, we plotted the AFM scanning of a 500 grit polished rough surface and the unpolished texture like side in both 3D view and 1D roughness height view. From figure D.2a and figure D.2c, we can see that the roughness scale of texture side is much greater than 500 grit polished surface.

[1]However, the scanning range it can reach for a single scan is on the order of few hundreds μm^2, which may not be able to accurately capture the average roughness size of our $NdGaO_3$ samples.

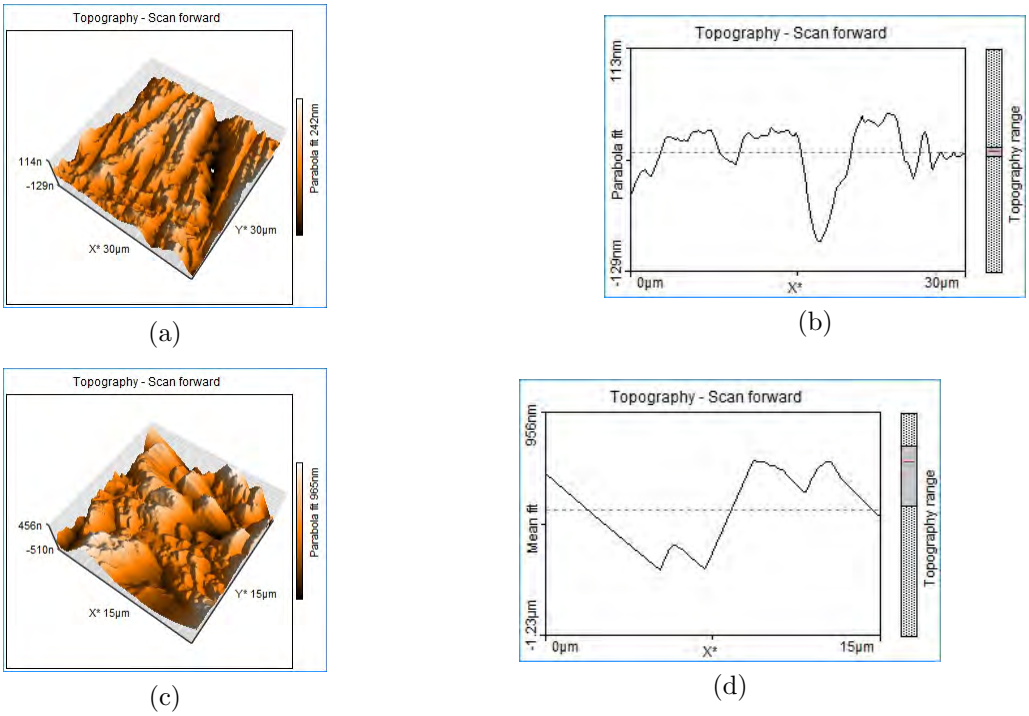
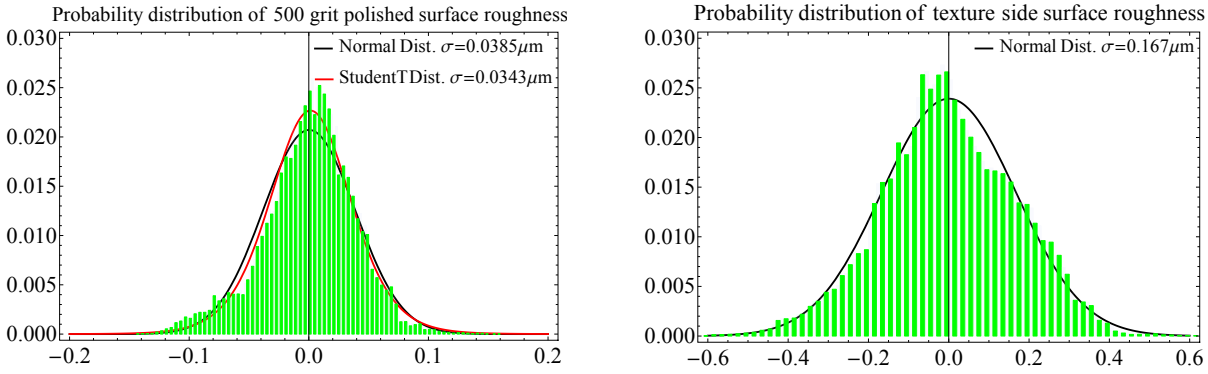


Figure D.2: (a) 3D view of 500 grit polished $NdGaO_3$ rough surface within the area 30 μm × 30 μm. (b) A single scan of 500 grit polished surface roughness profile took along X axis as shown figure D.2a. (c) 3D view of unpolished $NdGaO_3$ texture side rough surface within the area 15 μm × 15 μm. (d) A single scan of unpolished texture side surface roughness profile took along X axis as shown figure D.2c.

From figure D.2b and D.2d, we can tell that roughness scale of 500 grit polished surface is around 0.1 μm while texture like side has surface roughness size around 1 μm. From figure D.2d, we can clearly see the texture like characteristic from its flatness on every single division and no considerate fluctuations over each division.
To gain some aspects of roughness height distribution of real rough surfaces, in figure D.3, we plotted the surface roughness height probability distributions of 500 grit polished rough surface and texture like side as depicted in figure D.3a and D.3b, respectively. In figure D.3a, we fitted the probability distribution by both student T distribution and normal distribution. In general, student T distribution seemed to fit the roughness height distribution profile better than normal distribution, however, normal distribution fitted surface roughness size σ agreed better with calculated surface roughness RMS value than student T distribution. As to texture like rough side surface roughness distribution in figure



(a) (b)

Figure D.3: (a) The probability distribution histogram of 500 grit polished surface roughness, the bottom axis is in unit of μm and its surface roughness RMS is calculated to be 0.0385 μm. (b) The probability distribution histogram of texture side rough surface with RMS calculated to be 0.167 μm, and normal distribution fitting agreed with roughness size well.

D.3b, a Gaussian distribution function fitted the distribution reasonably well meanwhile it showed consistency calculated surface roughness RMS value 0.167 μm.

Appendix E

Refinement to $S_{j,k}$ analysis of IPFY

The discussion in this chapter originates from equation (2.11) in the scenario where we have a smooth surface homogeneous bulk sample but the experimental conditions fluctuate in appreciable amount. The goal is to explore how the fluctuations in experimental conditions affect our normal $S_{j,k}(E_i)$ analysis of IPFY in deriving linear attenuation coefficients.

E.1 $S_{j,k}$ analysis

Experimentally, for homogeneous bulk materials with smooth surfaces, the IPFY expression is written as:

$$IPFY = \frac{\nu_{Grid}(E_i)}{\eta(E_f)\frac{\Omega}{4\pi}\omega_Y(E_i,E_f)\mu_Y(E_i)}\left(\mu(E_i)+\mu(E_f)\frac{\sin\alpha}{\sin\beta}\right) \quad \text{(E.1)}$$

$$= A(E_i)\left(\mu(E_i)+\mu(E_f)\frac{\sin\alpha}{\sin\beta}\right) \quad \text{(E.2)}$$

For simplicity, we will denote $A(E_i)$ as the total factor outside the brackets as shown in equation (E.1). If we perform two measurements of IPFY with geometry j and k,we can write their IPFY expressions of them as following:

$$IPFY_j = A_j(E_i)\left(\mu(E_i)+\mu(E_f)\frac{\sin\alpha_j}{\sin\beta_j}\right) \quad \text{(E.3)}$$

$$IPFY_k = A_k(E_i)\left(\mu(E_i)+\mu(E_f)\frac{\sin\alpha_k}{\sin\beta_k}\right) \quad \text{(E.4)}$$

Experimentally, if we measure IPFY for two different geometries j and k use same detector at fixed emission energy E_f, we would have same detection efficiency $\eta(E_f)$. The solid angle Ω is also a fixed quantity for both geometries except for some extreme angles where detector position is in parallel with sample plate or the detector position was changed in subsequent measurement. Since our subject is the same for both geometries, $\omega_Y(E_i, E_f), \mu_Y(E_i)$ stays the same. For two separate measurements, $\nu_{Grid}(E_i)$ would potentially change if the beam spot on the grid is deviated from its original position in another measurement. Mostly, the change in grid quantum efficiency is small and can be neglected.
Therefore, it is reasonable to make the assumption that $A_j(E_i) = A_k(E_i) = A(E_i)$, and based on that we will find that:

$$A(E_i) = \frac{1}{\mu(E_f)} \frac{IPFY_j - IPFY_k}{\frac{\sin\alpha_j}{\sin\beta_j} - \frac{\sin\alpha_k}{\sin\beta_k}} \tag{E.5}$$

$$= \frac{1}{\mu(E_f)} S_{j,k}(E_i) \tag{E.6}$$

where we define our $S_{j,k}(E_i)$ to be:

$$S_{j,k}(E_i) = \frac{IPFY_j - IPFY_k}{\frac{\sin\alpha_j}{\sin\beta_j} - \frac{\sin\alpha_k}{\sin\beta_k}} \tag{E.7}$$

By inserting equation (E.6) back into equation (E.2) and rearranging it, and we will obtain:

$$\mu(E_i) = \left(\frac{IPFY}{S_{j,k}(E_i)} - \frac{\sin\alpha}{\sin\beta}\right) \mu(E_f) \tag{E.8}$$

Equation (E.8) implies that the angle dependence $S_{j,k}(E_i)$ analysis of IPFY will provide us with a direct measure of total linear attenuation coefficients.

E.2 The effect of Unequal $A_{j,k}(E_i)$ on $S_{j,k}(E_i)$ analysis

As we have mentioned before, our success in applying $S_{j,k}(E_i)$ analysis of IPFY to extract total linear attenuation coefficients is relying on one important condition that $A_j(E_i) = A_k(E_i)$ for two different geometries j and k. However, there are scenarios where $A_j(E_i)$ is not coincident with $A_k(E_i)$ exactly. For example, as we discussed in section 1.1, when the incident beam spot on the grid moved in subsequent measurement, we might as well have a

significant change in $\nu_{Grid}(E_i)$. This difference will eventually reflect itself in $A(E_i)$. The motivation here is to know how much effect we would have on our $S_{j,k}(E_i)$ analysis when $A(E_i)$ varied with respect to different geometries. Here we will expand our old $S_{j,k}(E_i)$ analysis to a more general case where $A(E_i)$ is allowed to vary for different geometries.

E.2.1 The collapse of IPFY spectra

From our former $S_{j,k}(E_i)$ analysis of IPFY on NiO and NdGaO3, we noticed that after divided by $S_{j,k}(E_i)$ and subtracted the corresponding ratio $\frac{\sin\alpha}{\sin\beta}$, the IPFY spectra from different geometries will eventually collapse into one single curve.[1] Such experimental results from NiO and NdGaO3 followed exactly as what equation (1.8) predicted since they all measure the same quantity $\mu(E_i)$. However, as we will prove it later, this result will hold even in the case $A_j(E_i) \neq A_k(E_i)$.
Simply followed from equation (E.7), we will have:

$$\frac{IPFY_j}{S_{j,k}(E_i)} = \frac{IPFY_j}{IPFY_j - IPFY_k}\left(\frac{\sin\alpha_j}{\sin\beta_j} - \frac{\sin\alpha_k}{\sin\beta_k}\right) \tag{E.9}$$

$$\frac{IPFY_k}{S_{j,k}(E_i)} = \frac{IPFY_k}{IPFY_j - IPFY_k}\left(\frac{\sin\alpha_j}{\sin\beta_j} - \frac{\sin\alpha_k}{\sin\beta_k}\right) \tag{E.10}$$

The subtraction of equation (E.9) and (E.10) is:

$$\frac{IPFY_j}{S_{j,k}(E_i)} - \frac{IPFY_k}{S_{j,k}(E_i)} = \frac{\sin\alpha_j}{\sin\beta_j} - \frac{\sin\alpha_k}{\sin\beta_k} \tag{E.11}$$

Rearrange equation (E.11), we will get:

$$\frac{IPFY_j}{S_{j,k}(E_i)} - \frac{\sin\alpha_j}{\sin\beta_j} = \frac{IPFY_k}{S_{j,k}(E_i)} - \frac{\sin\alpha_k}{\sin\beta_k} \tag{E.12}$$

If we multiply both sides of equation (E.12) by $\mu(E_f)$, we will have the right hand side of equation (E.8) which turns out to be $\mu(E_i)$ in the case $A_j(E_i) = A_k(E_i)$.This indicates that $\left(\frac{IPFY}{S_{j,k}(E_i)} - \frac{\sin\alpha}{\sin\beta}\right)\mu(E_f)$ from any pair of IPFY spectra will always collapse into one single curve even though this expression might not correspond to $\mu(E_i)$ in the situation $A_j(E_i) \neq A_k(E_i)$.

E.2.2 Deviation of $S_{j,k}(E_i)$ analysis under $A_j(E_i) \neq A_k(E_i)$

From equation (E.3),(E.4) and (E.7), we can rewrite $S_{j,k}(E_i)$ in a more general sense:

$$S_{j,k}(E_i) = \frac{IPFY_j - IPFY_k}{\frac{\sin\alpha_j}{\sin\beta_j} - \frac{\sin\alpha_k}{\sin\beta_k}} \tag{E.13}$$

$$= \frac{A_j(E_i)\left(\mu(E_i) + \mu(E_f)\frac{\sin\alpha_j}{\sin\beta_j}\right) - A_k(E_i)\left(\mu(E_i) + \mu(E_f)\frac{\sin\alpha_k}{\sin\beta_k}\right)}{\frac{\sin\alpha_j}{\sin\beta_j} - \frac{\sin\alpha_k}{\sin\beta_k}} \tag{E.14}$$

$$= \frac{(A_j(E_i) - A_k(E_i))\mu(E_i) + \left(A_j(E_i)\frac{\sin\alpha_j}{\sin\beta_j} - A_k(E_i)\frac{\sin\alpha_k}{\sin\beta_k}\right)\mu(E_f)}{\frac{\sin\alpha_j}{\sin\beta_j} - \frac{\sin\alpha_k}{\sin\beta_k}} \tag{E.15}$$

If we assume that $\frac{A_j(E_i)}{A_k(E_i)} = M_{jk}$ which is independent of energies, we can write $S_{j,k}(E_i)$ in terms of M_{jk} as:

$$S_{j,k}(E_i) = \frac{(M_{jk}-1)A_k(E_i)\mu(E_i) + \left(M_{jk}A_k(E_i)\frac{\sin\alpha_j}{\sin\beta_j} - A_k(E_i)\frac{\sin\alpha_k}{\sin\beta_k}\right)\mu(E_f)}{\frac{\sin\alpha_j}{\sin\beta_j} - \frac{\sin\alpha_k}{\sin\beta_k}} \tag{E.16}$$

$$= A_k(E_i)\frac{(M_{jk}-1)\left(\mu(E_i) + \mu(E_f)\frac{\sin\alpha_j}{\sin\beta_j}\right) + \left(\frac{\sin\alpha_j}{\sin\beta_j} - \frac{\sin\alpha_k}{\sin\beta_k}\right)\mu(E_f)}{\frac{\sin\alpha_j}{\sin\beta_j} - \frac{\sin\alpha_k}{\sin\beta_k}} \tag{E.17}$$

$$= A_k(E_i)\left(\mu(E_f) + \frac{M_{jk}-1}{\frac{\sin\alpha_j}{\sin\beta_j} - \frac{\sin\alpha_k}{\sin\beta_k}}\left(\mu(E_i) + \mu(E_f)\frac{\sin\alpha_j}{\sin\beta_j}\right)\right) \tag{E.18}$$

$$\frac{IPFY_k}{S_{j,k}(E_i)} = \frac{A_k(E_i)\left(\mu(E_i) + \mu(E_f)\frac{\sin\alpha_k}{\sin\beta_k}\right)}{A_k(E_i)\left(\mu(E_f) + \frac{M_{jk}-1}{\frac{\sin\alpha_j}{\sin\beta_j} - \frac{\sin\alpha_k}{\sin\beta_k}}\left(\mu(E_i) + \mu(E_f)\frac{\sin\alpha_j}{\sin\beta_j}\right)\right)} \tag{E.19}$$

$$= \frac{\frac{\mu(E_i)}{\mu(E_f)} + \frac{\sin\alpha_k}{\sin\beta_k}}{1 + \frac{M_{jk}-1}{\frac{\sin\alpha_j}{\sin\beta_j} - \frac{\sin\alpha_k}{\sin\beta_k}}\left(\frac{\mu(E_i)}{\mu(E_f)} + \frac{\sin\alpha_j}{\sin\beta_j}\right)} \tag{E.20}$$

Therefore, we can easily write:

$$\frac{IPFY_k}{S_{j,k}(E_i)} - \frac{\sin\alpha_k}{\sin\beta_k} = \frac{\frac{\mu(E_i)}{\mu(E_f)} + \frac{\sin\alpha_k}{\sin\beta_k}}{1 + \frac{M_{jk}-1}{\frac{\sin\alpha_j}{\sin\beta_j} - \frac{\sin\alpha_k}{\sin\beta_k}}\left(\frac{\mu(E_i)}{\mu(E_f)} + \frac{\sin\alpha_j}{\sin\beta_j}\right)} - \frac{\sin\alpha_k}{\sin\beta_k} \tag{E.21}$$

When $M_{jk} = 1$, where $A_j(E_i) = A_k(E_i)$, equation (E.21) is reduced into (E.22) and by rearrange (E.22), we will get equation (E.8) which gives us linear attenuation coefficients.

$$\frac{IPFY_k}{S_{j,k}(E_i)} - \frac{\sin\alpha_k}{\sin\beta_k} = \frac{\mu(E_i)}{\mu(E_f)} \tag{E.22}$$

By invoke formula (E.21) and plot $\left(\frac{IPFY_k}{S_{j,k}(E_i)} - \frac{\sin\alpha_k}{\sin\beta_k}\right)\mu(E_f)$ versus energy for different M_{jk} values, we will gain some aspects of so called $A_{j,k}(E_i)$ effect on traditional $S_{j,k}(E_i)$ analysis. In figure E.1, we used $\mu(E_i)$ of NdGaO3 from literature and choose the two geometries to be $\alpha_j = 20\,^\circ, \beta_j = 53\,^\circ; \alpha_k = 90\,^\circ, \beta_k = 41.6\,^\circ$. $M_{jk} = 1$ case corresponds to where we have unchanged $A(E_i)$ for two different geometries, where we shall see the total linear attenuation coefficient $\mu(E_i)$ instead. When M_{jk} is 10 percent away from expected value 1, the upper limit will bring the spectrum upwards and the magnitude around the peak regions increased dramatically while the lower limit did exactly the opposite way.

E.2.3 Ratio of $\frac{A_j(E_i)}{A_k(E_i)}$

From our previous analysis, we concluded that the difference between $A_j(E_i)$ and $A_k(E_i)$ will have significant impacts on our $S_{j,k}(E_i)$ analysis. To know how exactly $A(E_i)$ change from one geometry to another geometry is of crucial importance. Theoretically, the most straight forward way is what can be simply derived from equation (E.3) and (E.4):

$$A_j(E_i) = \frac{IPFY_j}{\mu(E_i) + \mu(E_f)\frac{\sin\alpha_j}{\sin\beta_j}} \tag{E.23}$$

$$A_k(E_i) = \frac{IPFY_k}{\mu(E_i) + \mu(E_f)\frac{\sin\alpha_k}{\sin\beta_k}} \tag{E.24}$$

$$\frac{A_j(E_i)}{A_k(E_i)} = \frac{IPFY_j}{IPFY_k}\frac{\mu(E_i) + \mu(E_f)\frac{\sin\alpha_k}{\sin\beta_k}}{\mu(E_i) + \mu(E_f)\frac{\sin\alpha_j}{\sin\beta_j}} \tag{E.25}$$

The shortcoming of using equation (E.25) to obtain the ratio of $\frac{A_j(E_i)}{A_k(E_i)}$ is that we have to have accurate total linear attenuation coefficients $\mu(E)$ first. However, once we have the ratio and the ratio turned out to be constant within acceptable range with respect to incident photon energy, we can apply it to one of the IPFY spectra to reestablish the prerequisite $A_j(E_i)' = A_k(E_i)'$, and therefore validate our normal $S_{j,k}(E_i)$ approach.

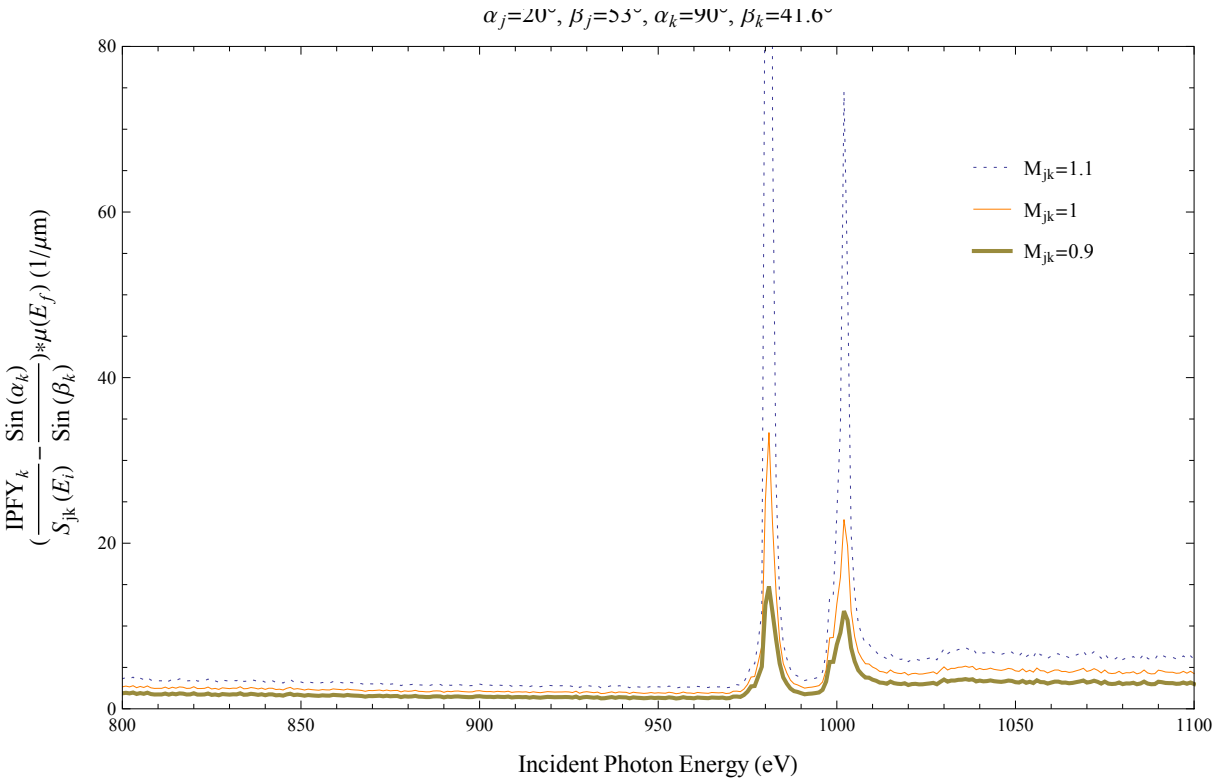


Figure E.1: The effect of varied $A_{j,k}(E_i)$ for two different geometries on $S_{j,k}(E_i)$ analysis from $NdGaO_3$ data.

Another way of looking at the ratio of $\frac{A_j(E_i)}{A_k(E_i)}$ is to think about its original form:

$$A(E_i) = \frac{\nu_{Grid}(E_i)}{\eta(E_f)\frac{\Omega}{4\pi}\omega_Y(E_i, E_f)\mu_Y(E_i)} \tag{E.26}$$

In SGM beamline, we have two newly installed Amptek detectors within the scattering plane of incident X-ray beam and one PGT detector in an azimuthal angle. The angle dependence $S_{j,k}(E_i)$ analysis can be done either by using IPFY spectra from two different detectors but within one measurement or by using IPFY spectra from two independent measurements with different geometries but share the same detector. In both cases, $\omega_Y(E_i, E_f), \mu_Y(E_i)$ would always be the same for two different geometries since we measured at same incident photon energy, detected at fixed emission energy and fixed atom or core state Y. However, this is rarely the case, but if there is big change in the energy calibration of beamline between those two measurements, we would have non-negligible difference for $\omega_Y(E_i, E_f), \mu_Y(E_i)$ from two different geometries. Based on the discussion above, we can also write the ratio of $\frac{A_j(E_i)}{A_k(E_i)}$ as:

$$\frac{A_j(E_i)}{A_k(E_i)} = \frac{\nu^j{}_{Grid}(E_i)\,\eta_k(E_f)\,\Omega_k}{\nu^k{}_{Grid}(E_i)\,\eta_j(E_f)\,\Omega_j} \tag{E.27}$$

In the case where we have IPFY spectra detected by two different detectors within one scan, we will have $\nu^j{}_{Grid}(E_i) = \nu^k{}_{Grid}(E_i)$ since the actual incident beam intensity after filtered by the grid and ring current of the synchrotron are exactly the same for both detectors in this case. At fixed detection energy, we will have $\frac{\eta_j(E_f)}{\eta_k(E_f)} = Constant$, and the ratio of $\frac{\Omega_j}{\Omega_k}$ also stayed unchange for fixed detector geometries. In this sense, we can further reduce formula (E.27) in this case as:

$$\frac{A_j(E_i)}{A_k(E_i)} = \frac{\eta_k(E_f)\,\Omega_k}{\eta_j(E_f)\,\Omega_j} \tag{E.28}$$

$$= Constant \tag{E.29}$$

The result derived above has significant implications as the ratio of $\frac{A_j(E_i)}{A_k(E_i)}$ is indeed independent of incident photon energy $\mu(E_i)$, which will validate our $S_{j,k}(E_i)$ analysis after apply the scaling factor M_{jk} we defined before to one of the IPFY spectra. We will reformulize the $S_{j,k}(E_i)$ analysis in a functional form for the case $\frac{A_j(E_i)}{A_k(E_i)} = M_{jk}$ in subsequent sections.

In another case where we have IPFY spectra measured twice by the same detector at different geometries, equation (E.27) is therefore reduced into equation (E.30) due to the fact that we used the same detector and the solid angle for both geometries should be the

same if the detector position remained unchanged during two measurements.

$$\frac{A_j\left(E_i\right)}{A_k\left(E_i\right)} = \frac{{\nu^j}_{Grid}\left(E_i\right)}{{\nu^k}_{Grid}\left(E_i\right)} \tag{E.30}$$

However, ${\nu^j}_{Grid}\left(E_i\right)$ may not always be the same as ${\nu^k}_{Grid}\left(E_i\right)$. When we do a second measure of IPFY for different geometry, the incident beam spot on the grid can potentially move which will cause the difference in $\nu_{Grid}\left(E_i\right)$. Furthermore, it is hard to tell whether such difference will be energy dependent and if it is, the M_{jk} scaling factor correction will no longer apply.

E.2.4 Reformulism of $S_{j,k}\left(E_i\right)$ analysis in the case $\frac{A_j(E_i)}{A_k(E_i)} = M_{jk}$

As we argued in the former section, if we have the situation where $\frac{A_j(E_i)}{A_k(E_i)} = M_{jk}$ for two different geometries which is independent of incident photon energy $\mu\left(E_i\right)$, we can simply multiply the scaling factor M_{jk} to $IPFY_k$ and reestablish the only requirement $A_j\left(E_i\right)' = A_k\left(E_i\right)'$ for normal $S_{j,k}\left(E_i\right)$ analysis. To be more specific, we will denote our new $S_{j,k}\left(E_i\right)'$ as:

$$S_{j,k}\left(E_i\right)' = \frac{IPFY_j - M_{jk} * IPFY_k}{\frac{\sin\alpha_j}{\sin\beta_j} - \frac{\sin\alpha_k}{\sin\beta_k}} \tag{E.31}$$

where $M_{jk} = \frac{A_j(E_i)}{A_k(E_i)}$ for different geometry j and k.
Note that since we defined $M_{jk} = \frac{A_j(E_i)}{A_k(E_i)}$, our M_{kj} will then become $1/M_{jk}$, and the $S_{j,k}\left(E_i\right)'$ is not exactly identical to $S_{k,j}\left(E_i\right)'$. Instead, $S_{k,j}\left(E_i\right)'$ is defined as:

$$S_{k,j}\left(E_i\right)' = \frac{IPFY_k - M_{kj} * IPFY_j}{\frac{\sin\alpha_k}{\sin\beta_k} - \frac{\sin\alpha_j}{\sin\beta_j}} \tag{E.32}$$

$$= \frac{1}{M_{jk}} S_{k,j}\left(E_i\right)' \tag{E.33}$$

Therefore, the corresponding $\mu\left(E_i\right)$ can be corrected accordingly as:

$$\mu_{corr}\left(E_i\right) = \left(\frac{IPFY_j}{S_{j,k}\left(E_i\right)'} - \frac{\sin\alpha_j}{\sin\beta_j}\right)\mu\left(E_f\right) \tag{E.34}$$

$$= \left(\frac{IPFY_j}{M_{jk}S_{k,j}\left(E_i\right)'} - \frac{\sin\alpha_j}{\sin\beta_j}\right)\mu\left(E_f\right) \tag{E.35}$$

$$\mu_{corr}(E_i) = \left(\frac{M_{jk} * IPFY_k}{S_{j,k}(E_i)'} - \frac{\sin\alpha_k}{\sin\beta_k}\right)\mu(E_f) \quad (E.36)$$

$$= \left(\frac{IPFY_k}{S_{k,j}(E_i)'} - \frac{\sin\alpha_k}{\sin\beta_k}\right)\mu(E_f) \quad (E.37)$$

In the discussion of the ratio $\frac{A_j(E_i)}{A_k(E_i)}$ in section 1.2.3, we have drawn the conclusion that for IPFY spetra from same measurement by different detectors at different geometries, we would always have $\frac{A_j(E_i)}{A_k(E_i)} = Constant$ (see equation (E.29)) that is independent of incident photon energies. Once this requirement is satisfied, our new $S_{j,k}(E_i)'$ analysis will be guarantteed to work to correct the $\mu(E_i)$ spectrum. This conclusion will be proved in the experimental demonstration later.

E.2.5 Error propagation

We have already discussed about how normal $S_{j,k}(E_i)$ analysis results will differ from their expectations in the case $A_j(E_i) \neq A_j(E_i)$. To be more explicit about how errors propagate during our original analysis, we will work out the percentage error expressions for both $S_{j,k}(E_i)$ and $\mu(E_i)$ in the case $\frac{A_j(E_i)}{A_k(E_i)} = M_{jk}$.
First, we will define another quantity δ_{jk} as:

$$\delta_{jk} = M_{jk} - 1 \quad (E.38)$$

The percentage error expression for $S_{j,k}(E_i)$ in the case $\frac{A_j(E_i)}{A_k(E_i)} = M_{jk}$ is:

$$\frac{\delta S_{j,k}(E_i)}{S_{j,k}(E_i)} = \frac{S_{j,k}(E_i) - S_{j,k}(E_i)'}{S_{j,k}(E_i)'} \quad (E.39)$$

By inserting equation (E.7), (E.31) and (E.38) into (E.39), we will have:

$$\frac{\delta S_{j,k}(E_i)}{S_{j,k}(E_i)} = \frac{\frac{IPFY_j - IPFY_k}{\frac{\sin\alpha_j}{\sin\beta_j} - \frac{\sin\alpha_k}{\sin\beta_k}} - \frac{IPFY_j - (1+\delta_{jk}) * IPFY_k}{\frac{\sin\alpha_j}{\sin\beta_j} - \frac{\sin\alpha_k}{\sin\beta_k}}}{\frac{IPFY_j - (1+\delta_{jk}) * IPFY_k}{\frac{\sin\alpha_j}{\sin\beta_j} - \frac{\sin\alpha_k}{\sin\beta_k}}} \quad (E.40)$$

$$= \frac{\delta_{jk} * IPFY_k}{IPFY_j - (1+\delta_{jk}) * IPFY_k} \quad (E.41)$$

Equation (E.41) can be reduced by inserting equation (E.3) and (E.4) into it, so it becomes:

$$\frac{\delta S_{j,k}(E_i)}{S_{j,k}(E_i)} = \frac{\delta_{jk} * A_k(E_i)\left(\mu(E_i) + \mu(E_f)\frac{\sin\alpha_k}{\sin\beta_k}\right)}{(1+\delta_{jk}) * A_k(E_i)\,\mu(E_f)\left(\frac{\sin\alpha_j}{\sin\beta_j} - \frac{\sin\alpha_k}{\sin\beta_k}\right)} \tag{E.42}$$

$$= \frac{\delta_{jk}}{1+\delta_{jk}} \frac{\frac{\mu(E_i)}{\mu(E_f)} + \frac{\sin\alpha_k}{\sin\beta_k}}{\frac{\sin\alpha_j}{\sin\beta_j} - \frac{\sin\alpha_k}{\sin\beta_k}} \tag{E.43}$$

In order to make the final expression neat, we will introduce another notation g as the ratio of $\frac{\sin\alpha}{\sin\beta}$. In this way, for different geometry j and k, g is notated as:

$$g_j = \frac{\sin\alpha_j}{\sin\beta_j} \tag{E.44}$$

$$g_k = \frac{\sin\alpha_k}{\sin\beta_k} \tag{E.45}$$

Therefore, equation (E.43) can be further reduced as:

$$\frac{\delta S_{j,k}(E_i)}{S_{j,k}(E_i)} = \frac{\delta_{jk}}{1+\delta_{jk}} \frac{\frac{\mu(E_i)}{\mu(E_f)} + g_k}{g_j - g_k} \tag{E.46}$$

$$= \frac{\delta_{jk}}{1+\delta_{jk}} \frac{\frac{\mu(E_i)}{g_k\mu(E_f)} + 1}{\frac{g_j}{g_k} - 1} \tag{E.47}$$

To get a quantitative picture of $\delta S_{j,k}(E_i)/S_{j,k}(E_i)$, we plotted it as a function of $\mu(E_i)/\mu(E_f)$ and g_j/g_k in figure E.2. The ranges we chose for g_j/g_k and $\mu(E_i)/\mu(E_f)$ were based on real physical geometries in SGM beamline and real material attenuation coefficients. In SGM beamline, the sensible two geometry limits are $\alpha = 60\,°, \beta = 15.7\,°$ and $\alpha = 20\,°, \beta = 53.0\,°$, which gives us g_j/g_k range as (0.13, 7.5). For $NdGaO_3$, the linear attenuation coefficients within energy range of interests are within $(1.9\mu m^{-1}, 33.4\mu m^{-1})$ and $\mu(E_f = 524.9eV) \approx 3.48549\mu m^{-1}$, and therefore the range for $\mu(E_i)/\mu(E_f)$ is about (0.1, 10).
One of the common features among those four plots is that when g_j/g_k is close to 1, the error in $S_{j,k}(E_i)$ becomes very large as colored in blue and yellow, regardless of the incident or emission photon energies. Such result suggests a good way to reduce the error in our $S_{j,k}(E_i)$ analysis, that is to choose geometries where the ratio g_j/g_k is far away from 1. Compare figure E.2a and figure figure E.2b, figure E.2c and figure E.2d, the change of the sign in δ_{jk} generally reversed the distribution of $\delta\mu(E_i)/\mu(E_i)$ in terms of sign. To see

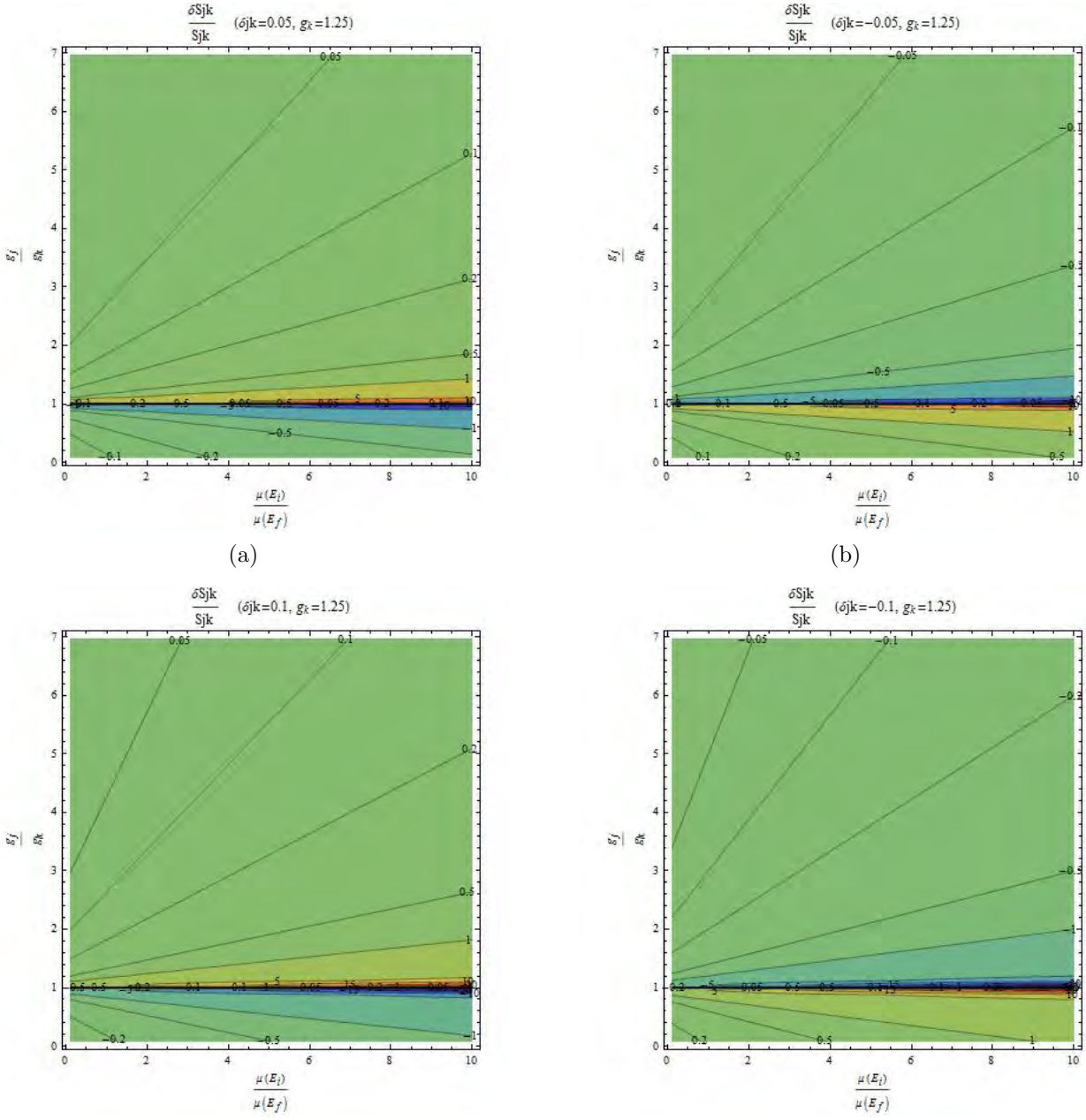


Figure E.2: The contour plots of $\delta S_{j,k}(E_i)/S_{j,k}(E_i)$ as a function of $\mu(E_i)/\mu(E_f)$ and g_j/g_k with δ_{jk} to be 0.05, -0.05, 0.1, -0.1, respectively, at fixed g_k=1.25.

how the magnitude of δ_{jk} affect $\delta S_{j,k}(E_i)/S_{j,k}(E_i)$, we can focus on the area where we have error less than 5 percent. 5 percent deviation of $A(E_i)$ offered us much wider range with percentage error less than 5% in terms of both geometries and linear attenuation coefficients, compared with 10 percent difference in $A(E_i)$ for two geometries. The areas (blue in figure E.2a and figure E.2c, yellow in E.2b and E.2d) where we have $\delta S_{j,k}(E_i)/S_{j,k}(E_i)$ less than -1, which means we would have negative $S_{j,k}(E_i)$, and furthermore result in negative $\mu(E_i)$ would not be taken into discussions, since negative $S_{j,k}(E_i)$ would obviously fail our regular $S_{j,k}(E_i)$ analysis.
Similarly, the percentage error expression for $\mu(E_i)$ in case $\frac{A_j(E_i)}{A_k(E_i)} = M_{jk}$ is:

$$\frac{\delta\mu(E_i)}{\mu(E_i)} = \frac{\mu_{uncorr}(E_i) - \mu_{corr}(E_i)}{\mu_{corr}(E_i)} \tag{E.48}$$

where $\mu_{uncorr}(E_i)$ is referred to the result obtained from normal $S_{j,k}(E_i)$ analysis as expressed in formula (E.8). Combined equation (E.21), (E.38) with (E.44), we obtain:

$$\frac{\delta\mu(E_i)}{\mu(E_i)} = \frac{\left(\frac{IPFY_k}{S_{j,k}(E_i)} - \frac{\sin\alpha_k}{\sin\beta_k}\right)\mu(E_f) - \mu(E_i)}{\mu(E_i)} \tag{E.49}$$

$$= \frac{\left(\frac{\frac{\mu(E_i)}{\mu(E_f)} + \frac{\sin\alpha_k}{\sin\beta_k}}{1 + \frac{\delta_{jk}}{\frac{\sin\alpha_j}{\sin\beta_j} - \frac{\sin\alpha_k}{\sin\beta_k}}\left(\frac{\mu(E_i)}{\mu(E_f)} + \frac{\sin\alpha_j}{\sin\beta_j}\right)} - \frac{\sin\alpha_k}{\sin\beta_k}\right)\mu(E_f) - \mu(E_i)}{\mu(E_i)} \tag{E.50}$$

where $\mu_{corr}(E_i)$ is replaced with $\mu(E_i)$. Eventually equation (E.46) can be simplied as:

$$\frac{\delta\mu(E_i)}{\mu(E_i)} = \frac{-\delta_{jk}\left(1 + g_k\frac{\mu(E_f)}{\mu(E_i)}\right)\left(\frac{\mu(E_i)}{\mu(E_f)} + g_j\right)}{(g_j - g_k) + \delta_{jk}\left(\frac{\mu(E_i)}{\mu(E_f)} + g_j\right)} \tag{E.51}$$

$$= -\frac{1 + g_k\frac{\mu(E_f)}{\mu(E_i)}}{1 + \frac{\frac{g_j}{g_k} - 1}{\delta_{jk}\left(\frac{\mu(E_i)}{g_k\mu(E_f)} + \frac{g_j}{g_k}\right)}} \tag{E.52}$$

In figure E.3a, we plotted $\delta\mu(E_i)/\mu(E_i)$ as a function of $\mu(E_i)/\mu(E_f)$ and g_j/g_k at fixed $g_k = 1.25$ but allow δ_{jk} to vary. The first thing we noticed from those four plots was that they all have sigularities which start around g_j/g_k equal to 1, and then those sigularities position themselves along a approximate straight line with respect to $\mu(E_i)/\mu(E_f)$. All those divergence correspond to the cases where the denominator $(g_j - g_k) + \delta_{jk}(\mu(E_i)/\mu(E_f) + g_j)$

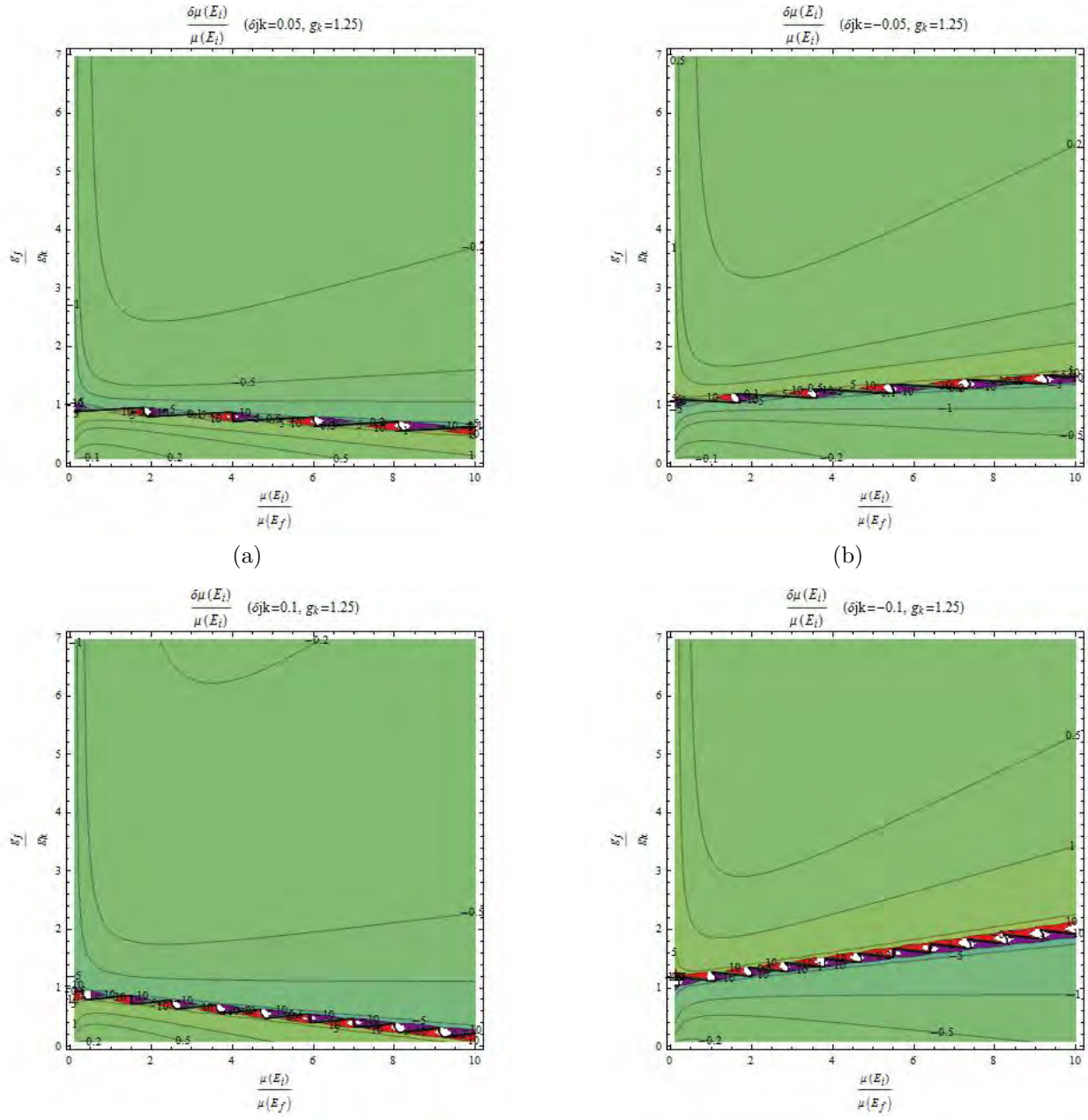


Figure E.3: (a) The contour plot of $\delta\mu\left(E_i\right)/\mu\left(E_i\right)$ as a function of $\mu\left(E_i\right)/\mu\left(E_f\right)$ and g_j/g_k with δ_{jk} to be 0.05, -0.05, 0.1, -0.1, respectively, at fixed g_k=1.25.

is approximately zero, which would end up giving us very large errors in $\mu(E_i)$.
For fixed δ_{jk}, for instance, in figure E.3a where δ_{jk} equal to 0.05, the simple conclusion we can draw is that bigger g_j/g_k would give us much wider range of $\mu(E_i)/\mu(E_f)$ with same percentage error in $\delta\mu(E_i)/\mu(E_i)$ than small g_j/g_k. We know for two geometries where we have g values far apart, depend on which one we choose to be the first geometry, g_j/g_k value could be large or small. The above argument indicated that choose the bigger g value as our first geometry which has bigger g_j/g_k would help to reduce errors in $\mu(E_i)$.
For fixed magnitude of δ_{jk} with different signs, we can compare figure E.3a and figure E.3b or figure E.3c and figure E.3d. The change of the sign in δ_{jk} reversed the sign in $\delta\mu(E_i)/\mu(E_i)$ but with similar distribution of percentage error. If we look at the areas in figure E.3a and figure E.3b where we have percentage error less than 0.2, we found that bigger g_j/g_k with positive δ_{jk} and smaller g_j/g_k with negative δ_{jk} have wider range of $\mu(E_i)/\mu(E_f)$ to be accessed.
For different magnitude of δ_{jk} but with same sign, we can clearly see that bigger $|\delta_{jk}|$ would have bigger percentage error in $\mu(E_i)$ at fixed g_j/g_k and $\mu(E_i)/\mu(E_f)$. The number of sigularities also increased with repect to the increase of $|\delta_{jk}|$.
As to gain some aspects of how each variable affects $\mu(E_i)$, we plotted $\delta\mu(E_i)/\mu(E_i)$ vs δ_{jk}, g_j/g_k and $\mu(E_i)/\mu(E_f)$, respectively.
From figure E.4, we can see that for bigger g_j/g_k ratios, the sigularities appeared at negative δ_{jk} side while smaller g_j/g_k ratios have the opposite trend. Consider the parts before we reach any sigularities, for higher g_j/g_k ratios, the rate of the change in $\delta\mu(E_i)/\mu(E_i)$ tend to slow down towards the direction of the increasing δ_{jk} whereas the smaller g_j/g_k ratios have increasing rate of change in $\delta\mu(E_i)/\mu(E_i)$. Within a sensible range near δ_{jk} equal to 0, the percentage error in $\mu(E_i)$ will continue to grow with respect to increasing magnitude of δ_{jk}.
As to the dependence of $\delta\mu(E_i)/\mu(E_i)$ on g_j/g_k, we can easily see from figure E.5 that low and high g_j/g_k ratios have smaller percentage errors than those situations when g_j and g_k have close values. This indicates that bigger difference between g_j and g_k would greatly reduce the errors in $\mu(E_i)$, in regardless of the ratio of $\mu(E_i)/\mu(E_i)$. In figure E.6, except for the blue curve, all other percentage error curves varied nearly independent of $\mu(E_i)/\mu(E_f)$ with $\mu(E_i)/\mu(E_f)$ in the range from 0.5 to 5 for the chosen g_j/g_k ratios. This indicates that for certain tolerance of the errors in $\mu(E_i)$, $S_{j,k}(E_i)$ analysis is still applicable for a very wide range of energies. Besides, one obvious conclusion to draw is that the percentage eror in $\mu(E_i)$ is smaller when we have smaller magnitude of δ_{jk}.

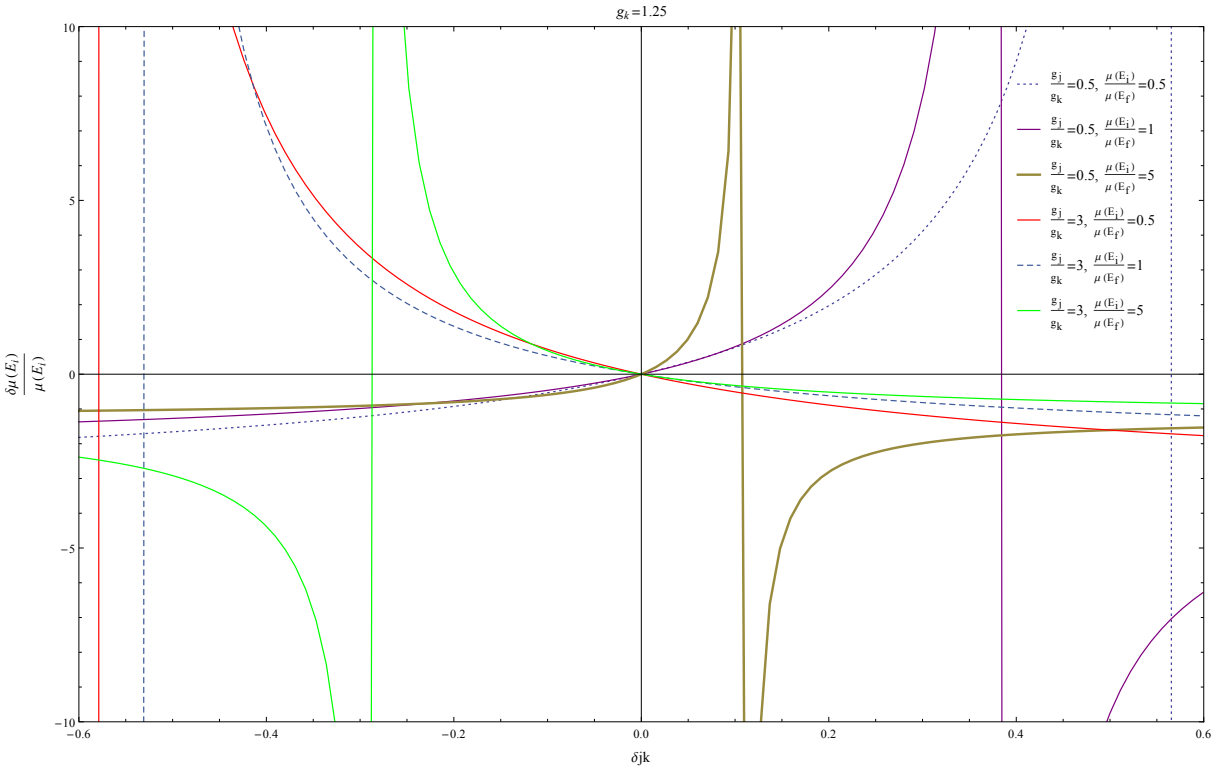


Figure E.4: $\delta\mu\left(E_i\right)/\mu\left(E_i\right)$ as a function of δ_{jk} where we have chosen g_j/g_k and $\mu\left(E_i\right)/\mu\left(E_f\right)$ values as shown in the legend.

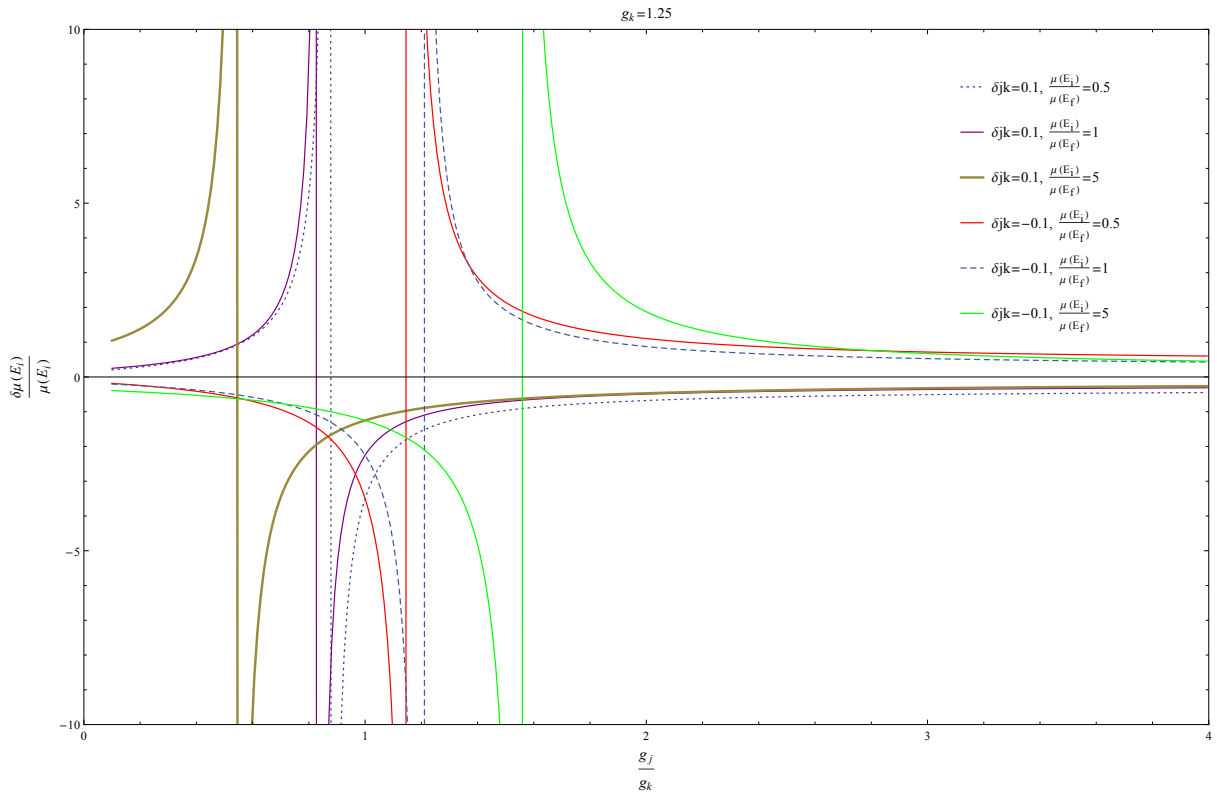


Figure E.5: $delta\mu\left(E_i\right)/\mu\left(E_i\right)$ as a function of g_j/g_k where we have low and high $\mu\left(E_i\right)/\mu\left(E_f\right)$ values and $\delta_{jk} = \pm 0.1$ as shown in the legend.

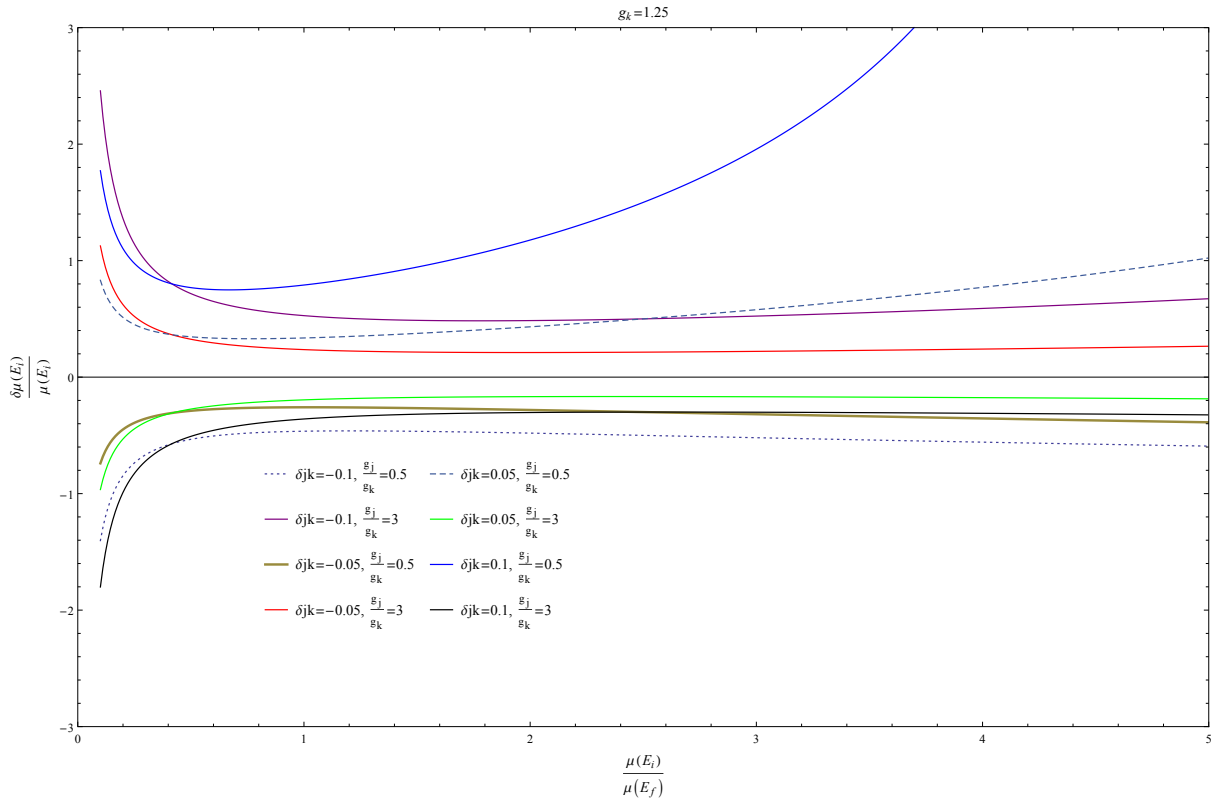


Figure E.6: $\delta\mu(E_i)/\mu(E_i)$ as a function of $\mu(E_i)/\mu(E_f)$ where we have low and high g_j/g_k values and $\delta_{jk} = \pm 0.1$ as shown in the legend.

E.3 Experimental demonstration of $A_{j,k}(E_i)$ effect on $S_{j,k}(E_i)$ analysis

In order to test what we have derived in previous section, we will illustrate IPFY measurements of NdGaO3 where we have unequal $A(E_i)$ for different geometries from both PGT detector and newly installed Amptek detectors. For this material, we did both long energy range scans from 800eV to 1100eV that covers pre-edge and post-edge structures and short energy rang scans from 960eV to 1020eV to identify more details around Nd M5 and M4 peak regions.

E.3.1 NdGaO3

The single crystal NdGaO3 was provided by MTI Corporation. They specify that the surface was polished to surface roughness level less than 5 Å and the crystal was oriented such that the $\langle 100 \rangle$ direction was normal to sample surface.

E.3.2 $S_{j,k}(E_i)$ analysis of IPFY spectra

Following from the standard $S_{j,k}(E_i)$ analysis for $NdGaO_3$, in figure E.7d, what we noticed first was that $\left(\frac{IPFY_k}{S_{j,k}(E_i)} - \frac{sin\alpha_k}{sin\beta_k}\right)\mu(E_f)$ did not end up providing us with the linear attenuation coefficients that expected to match up with atomic calculations from NIST as it was shown previously.[3] However, all $\left(\frac{IPFY_k}{S_{j,k}(E_i)} - \frac{sin\alpha_k}{sin\beta_k}\right)\mu(E_f)$ spectra did collapse into one single curve and this demonstrated agreement with what we predicted in equation (E.12).

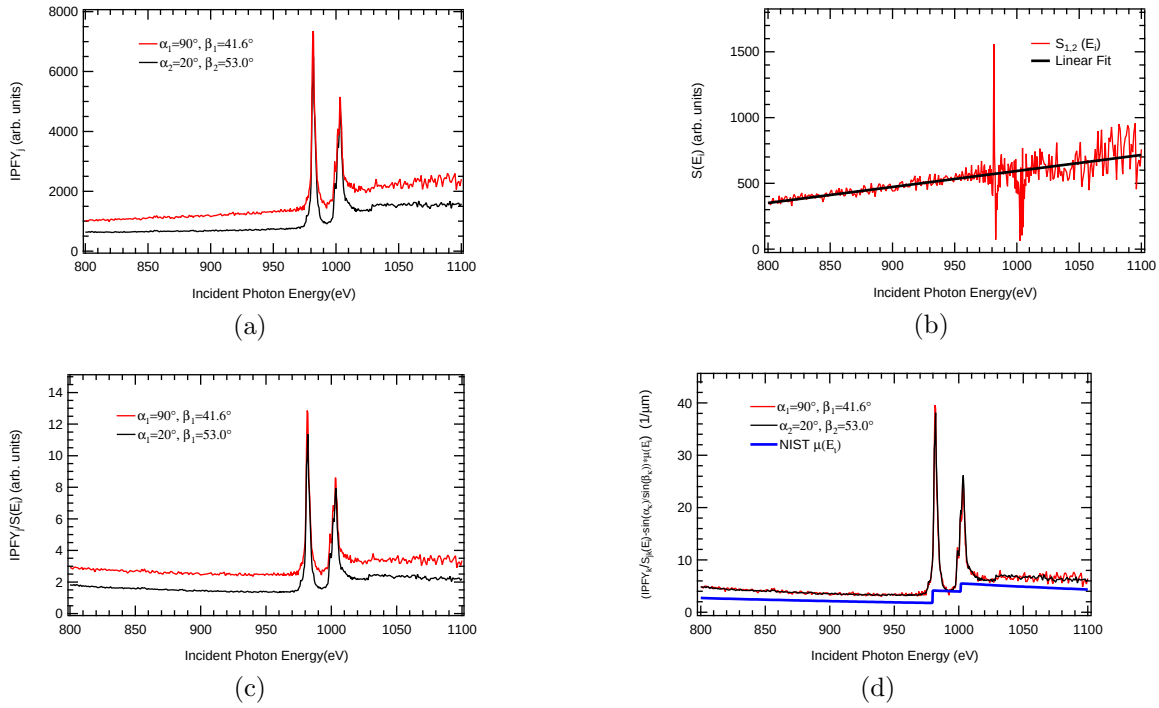


Figure E.7: (a) The IPFY of $NdGaO_3$ across the Nd $M_{5,4}$ edges over a wide energy range with geometries indicated on the figure. (b) The slope $S_{j,k}(E_i)$ is derived according to equation (E.7) with a linear fit to $S_{j,k}(E_i)$ is shown. (c) The IPFY spectra are divided by the linear fit to $S_{j,k}(E_i)$. (d) The spectra from figure E.7c are then subtracted by corresponding $\frac{sin\alpha}{sin\beta}$ and scaling to $\mu(E_f = 524.9eV) \approx 3.48549\mu m^{-1}$ for $NdGaO_3$ with a density of $\rho = 7.57g/cm^3$.[2]

In figure E.1, we illustrated that the difference between $A_{j,k}(E_i)$ from two different geometries will cause discrepancy in our measure of linear attenuation coefficients. This discrepancy is observed subsequently in real measurements. In figure E.8b, we can clearly see that there is a big difference between $A_{j,k}(E_i)$ from one geometry to another. The discrepancy between measurements and atomic calculation from NIST in figure E.7d is indeed caused by such difference.

To get a quantitative picture of how big this difference is, we plotted the division of $A(E_i)$ from those two geometries versus energy in subfigure E.8c. In previous sections, we assumed the ratio of $\frac{A_j(E_i)}{A_k(E_i)}$ is independent of incident photon energy, here what we actually observed in figure E.8c is not the case. We fitted our ratio by a constant line which has value 0.86 and also by a linear fitting, linear fitting fitted the ratio better than constant line, nevertheless, not as good as enough. In order to test whether the fitting is sufficient

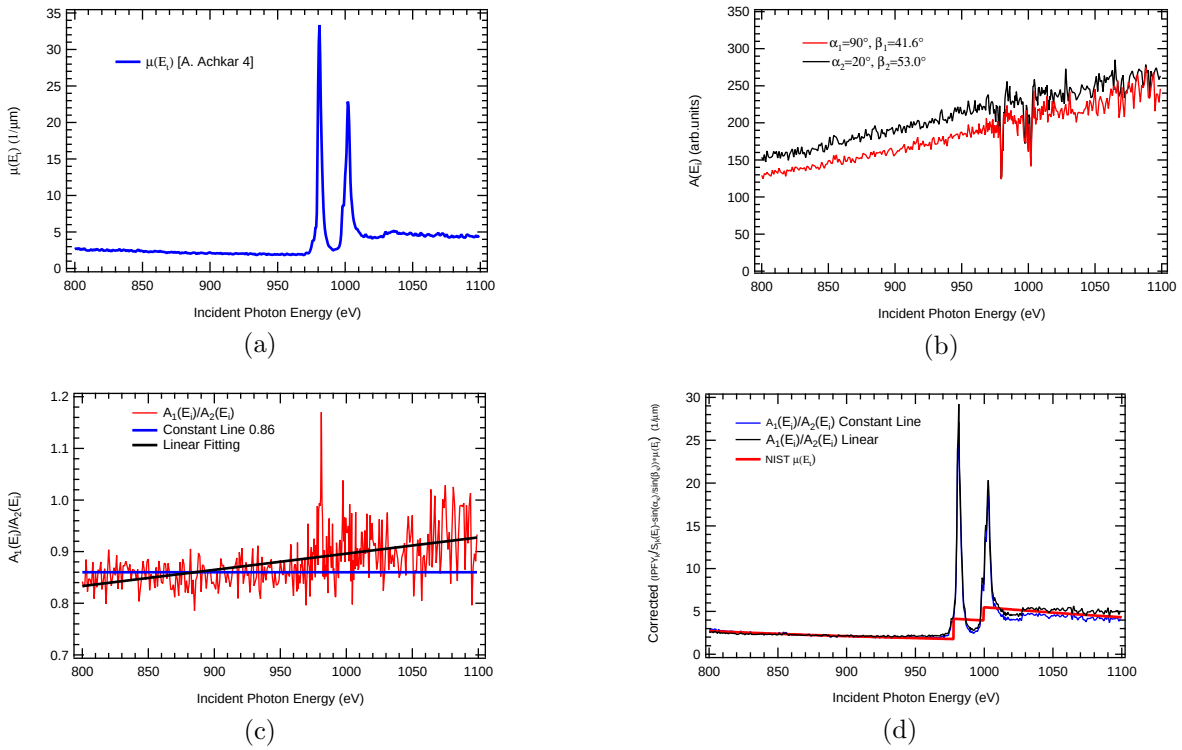


Figure E.8: (a) The $\mu(E_i)$ of $NdGaO_3$ over energy range 800eV to 1100eV.[4] (b) The $A(E_i)$ are derived from equation (E.23), (E.24) by inserting $\mu(E_i)$ from figure E.8a and IPFY spectra from figure E.7a for two different geometries. (c) The $\frac{A_1(E_i)}{A_2(E_i)}$ is obtained simply by the division of two curves from E.8b. We then fitted the ratio with constant line of value 0.86 and linear fitting with slope $3.1353 * 10^{-5}$ and intercept 0.58257, respectively. (d) The IPFY spetrum from geometry 2 ($\alpha = 20\,°, \beta = 53\,°$) is multiplied by the ratios $\frac{A_1(E_i)}{A_2(E_i)}$ from two fitting approaches. After that, we went through our normal $S_{j,k}(E_i)$ procedure by invoking this corrected IPFY spectrum, and we obtained their $\left(\frac{IPFY_k}{S_{j,k}(E_i)} - \frac{sin\alpha_k}{sin\beta_k}\right)\mu(E_f)$ spectra by scaling to $\mu(E_f = 524.9eV) \approx 3.48549\mu m^{-1}$ for $NdGaO_3$ with a density of $\rho = 7.57g/cm^3$.[2]

enough to correct the discrepancy as we discussed before, we multiplied one of the IPFY spectra by the $\frac{A_j(E_i)}{A_k(E_i)}$ ratio from both approaches, and redid the $S_{j,k}(E_i)$ analysis. In figure E.8d, the pre-edge parts of the spectra from both methods are consistent with atomic calculation from NIST, while the post-edge are either offsetted upper or lower than the calculations. There is no clear sign that linear fitting approach is better than constant line fitting approach whereas the linear fitting seemed to be better than constant fitting. The big difference in the post-edge part between the corrected spectrum and calculation

may due to the big fluctuations in the post-edge part of ratio $\frac{A_1(E_i)}{A_2(E_i)}$ in figure E.8c. The pre-edge part fluctuated much less than post-edge part and tended to a constant value, where approximation would expect to work better.